DISPERSED-PHASE TRANSFORMATION TOUGHENING IN ULTRAHIGH-STRENGTH STEELS

by

Gregory N. Haidemenopoulos

Dipl. Mechanical. Engineering, Aristotle University, Greece (1982)

S.M. Naval Architecture and Marine Engineering, M.I.T. (1985)

S.M. Metallurgy, M.I.T. (1985)

Submitted to the Department of Materials Science and Engineering
in partial fulfillment of the requirements for the degree of

DOCTOR OF PHILOSOPHY

at the

MASSACHUSETTS INSTITUTE OF TECHNOLOGY
May, 1988

Signature of Author _____
Department of Materials Science and Engineering
April 29, 1988

Certified by _____
Professor Morris Cohen
Thesis Supervisor

Certified by _____
Dr. Gregory B. Olson
Thesis Supervisor

Certified by _____
Dr. Mica Grujicic
Thesis Supervisor

Accepted by _____
Professor John B. Vander Sande, Chairman
Departmental Committee on Graduate Students

DISPERSED-PHASE TRANSFORMATION TOUGHENING IN ULTRAHIGH-STRENGTH STEELS

by

Gregory N. Haidemenopoulos

Submitted to the Department of Materials Science and Engineering
on April 29, 1988 in partial fulfillment of the requirements for the degree of
Doctor of Philosophy in Metallurgy

ABSTRACT

The interaction of deformation-induced martensitic transformation of dispersed austenite with fracture-controlling processes, such as microvoid-induced shear localization, results in a toughening mechanism termed dispersed-phase transformation toughening. The transformation behavior and the toughening effects are controlled by the stability of the austenitic dispersion, the most important microstructural parameters being the size and chemical composition of the austenite particles. The size affects the probability of finding a nucleation site in the particle, while the composition determines the chemical driving force for the martensitic transformation. The stability depends also on the stress state through interaction of the transformational volume change with stress triaxiality. For transformation toughening, the required stability of the austenitic dispersion is quite high, and can be achieved only by size refinement and compositional enrichment of the austenite particles.

The dispersed austenite can be in the form of either *retained austenite* or *precipitated austenite* . Retained austenite is that which conventionally remains untransformed after the steel is quenched from the austenitizing temperature. On the other hand, the precipitated austenite forms on high-temperature tempering or intercritical annealing. Transformation plasticity effects associated with retained austenite were studied in VAR 4340 steel, while precipitated austenite was examined in high Ni-Co secondary-hardening martensitic steels and in particular AF1410 steel.

The M_S^{σ} temperature provides a single-parameter characterization for the stability of dispersed austenite. It is the temperature at which the transformation occurs at the yield stress of the parent phase, and was measured as a function of stress state for retained austenite in 4340 steel. The results indicate that while the retained austenite is relatively stable for the pure-shear stress state, it is quite unstable for the crack-tip stress state and, therefore, retained austenite has little effect on toughness. Controlled experiments, designed to isolate the role of retained austenite in 4340 steel, using high-magnetic-field cryogenic treatments, demonstrate a flow-stabilizing effect in pure shear deformation. The delay in shear instability is attributed to the strain-induced transformation of retained austenite.

While the 0.2% macroscopic flow stress in 4340 steel is not found to be controlled by the transformation in the stress-assisted regime, as in the metastable fully-austenitic steels, microyielding experiments show that the

elastic limit is completely *transformation-controlled* for $T<M_S^{\sigma}$ and *slip-controlled* for $T>M_S^{\sigma}$. The constitutive behavior in the stress-assisted microyielding regime has been modelled by considering the effect of stress on the autocatalytic nucleation -site potency distribution. For retained austenite, the distribution is truncated due to the activation of sites during quenching. The procedure allows estimation of the carbon stabilization of the retained austenite during tempering. Such carbon enrichment decreases the chemical driving force and increases the frictional work of interfacial motion. Therefore, for transformation to continue, the above effects have to be compensated by supplying a mechanical driving force, which then determines the elastic limit (transformation stress) of the steel.

A functional form relating the M_S^{σ} temperature with the chemical composition and size of the austenite particles, the stress state, and the yield strength, has been developed using the dislocation-dissociation mechanism of martensitic nucleation. The microstructural requirements for dispersed-phase transformation toughening are then derived in terms of the austenite particle size and chemical enrichment in stabilizing solutes for a given strength and stress state. To achieve these microstructural requirements, three heat treatment methodologies have been studied in AF1410 steel, aiming at appropriate austenite stabilization : the standard single-tempering treatment, a two-step treatment for austenite nucleation at alloy-enriched cementite, and a two-step treatment for direct austenite nucleation during the short-time high-temperature first step of the treatment. The latter *direct-nucleation treatment* results in the formation of equilibrium austenite in an ultrafine (200Å) and Ni-enriched (30wt%) dispersion with high stability for crack-tip interactions. Both the Charpy (blunt notch) impact energy and the J_{IC} (sharp crack) fracture toughness are improved by 25% relative to the standard single treatments, with no loss of strength. This represents a significant advance in strength/toughness combinations, emphasizing the importance of dispersed-phase transformation toughening.

For transformation toughening to operate at ultrahigh-strengths (2000-2400 MPa), alloy design should be aimed both at enhanced austenite stabilization to compensate for the increased mechanical driving forces, and also at large transformation dilatation for maximum interaction with crack-tip triaxiality to enhance the fracture toughness. Computer-aided thermodynamic calculations of austenite stability combined with a formulation of the composition dependence of the lattice parameters provides a basis for the design of alloy matrix compositions for enhanced transformation toughening at extremely high strength levels.

Thesis Supervisor: **Dr. Morris Cohen.**
Title: Institute Professor, Emeritus.

Thesis Supervisor: **Dr. Gregory B. Olson.**
Title: Senior Research Associate.

Co-supervisor: **Dr. Mica Gruijic**
Title: Research Scientist

TABLE OF CONTENTS

LIST OF FIGURES

LIST OF TABLES

LIST OF SYMBOLS

d	*crystal interplanar spacing*
γ_s	*martensitic nucleus specific interfacial area*
n	*structural potency of nucleation sites defined in number of crystal planes in the defect.*
ΔG^{ch}	*chemical driving force for the martensitic transformation*
E^{str}	*elastic strain energy*
W_f	*frictional work of interfacial motion*
ΔG^{σ}	*mechanical driving force*
N_v	*density of nucleation sites*
γ_o	*transformational shear strain*
ε_o	*transformational normal strain*
V_p	*average austenite particle size*
f	*fraction of particles transformed*
M_s^{σ}	*temperature at which the transformation nucleates on yielding of the parent phase*
Md	*the temperature above which transformation cannot be induced by deformation*

M_S^{σ}(u.t)	*M_S^{σ} temperature for uniaxial tension*
M_S^{σ}(u.c)	*M_S^{σ} temperature for uniaxial compression*
M_S^{σ}(p.s)	*M_S^{σ} temperature for pure shear*
M_S^{σ}(c)	*M_S^{σ} temperature for the crack-tip stress state*
S-D	*strength-differential effect*
p	*autocatalytic factor*
$\Delta V/V$	*transformational volume change*

ACKNOWLEDGEMENTS

I am most gratefull to my thesis advisors, Prof. Morris Cohen and Dr. Greg B. Olson, for their guidance, advice and unfailing encouragement. Dr. Olson's imaginative power and insight combined with Prof. Cohen's experience and understanding of science provided the thrust that made this thesis posible.

I wish to express my appreciation to Dr. Mica Gruijic for his constant friendship and help. We worked together to solve several of the problems described in this thesis.

I am gratefull to many people that helped me one way or another to complete my doctoral thesis. The list includes:

Professors A.S. Argon, S.M. Allen of MIT and Prof. J.W. Hutchinson of Harvard University for stimulating discussions and for serving in the thesis defence committee.

Dr. Anthony J. Garratt Reed and Prof. John B. Vander Sande for their help with STEM Microanalysis.

Mim Rich, Yin-Lin Xie, Pat Kearney, Art Gregor, Mike Frongillo, and Gabriella Chapman for their valuable technical assistance.

Marge Meyer and Marie McTighe for their help with bureaucracy at MIT.

Frode Stavehaug, my officemate, for his friendship, the endless hours of conversation at the office, and for introducing me to Andy's chilie.

Mark Buonnano, a good friend, for making my stay at MIT more enjoyfull, and for bringing coffee and donuts at the library.

C.C. Young for his help with many of the experiments described in this work and for his friendship.

Woonsup Park, Mark Gore, Gary Carinci, Yukio kuroda, Huyak-Mo Lee, Dr. Dennis Haezebrouk, Dr. Fu-Rong Chen, Joe Aslanidis, and Minfa Lin for taking time out of their busy schedules to discuss about this research.

The entire Steel Research Group at MIT for providing a very stimulating environment for research.

Finally many thanks to my loving wife Yiota for her superhuman patience during these long five years at MIT. Without her love and support this thesis would not have been completed.

This thesis has been a part of a challenging research project entitled "Innovations in High-Strength Steel Technology". Financial support for this research was provided by a grant from the National Science Foundation.

This Thesis

is dedicated to:

my wife *Yiota*

and

my brother *Yannis*.

1. INTRODUCTION

A multi-institutional university-government-industry interdisciplinary research program was initiated at MIT in 1985 aiming at the advance and application of basic principles in physical metallurgy and related disciplines as a foundation for novel concepts in alloy design.

The long-term property objectives which serve as the "technological pull" or "driving force" for the research program are summarized in Fig.1.1. The figure shows data depicting the current achievable levels of K_{IC} fracture toughness for ultrahigh-strength martensitic steels as a function of hardness and tensile strength. Included are data bands for 9Ni-4Co steels, maraging steels, 4340 steel and its modifications (300M, Republic HP310), and M2 and M50 bearing steels. These toughness levels currently limit the usable hardness/strength properties of steels for structural applications (involving significant tensile loading) to Rc 50-55, or an ultimate tensile strength (UTS) range of 250-300 Ksi (1700-2100 MPa); the exact level depends on the required degree of reliability. The toughness ranges of premium steels at the Rc 50 and 55 hardness levels are indicated by the vertical bars in Fig.1.1. Toughness levels corresponding to a constant critical flaw size, a_c, at a design stress proportional to hardness are designated by the dashed lines passing through the centers of the vertical bars. These then identify the toughness improvements required for an increase in hardness at a constant critical flaw size. Steel users will acknowledge that an increase of 5 Rc points in usable hardness of these steels would represent a major advance in steel technology.

The toughness required for steels of Rc 55-60 hardness to replace steels currently of Rc 50-55 hardness is indicated by the vertical bars and dashed band shown further to the right in Fig.1.1. Meeting such strength - toughness objectives would not only expand the useful range of structural steels but would also overlap the required hardness levels (~Rc 60) of steels for advanced gears and bearings, and with a substantial toughness advantage over the M2 and M50-type steels of current importance. One can thus anticipate a wide range of engineering applications for the class of steels being considered here.

To avoid brittle fracture modes, the prior austenitic grain size should be kept to a minimum. This can be accomplished by an austenitic grain-refining dispersion for grain-boundary pinning. This dispersion must be sufficiently stable not only to remain out of solution during the austenitizing treatment but also to resist coarsening sufficiently so that a fine austenitic grain size can be maintained with a minimum volume fraction of the boundary-pinning phase.

An important consideration underlying the design of the grain-refining dispersion is that it should provide resistance to microvoid nucleation. The fracture toughness of high-cleanliness martensitic steels is typically limited by plastic shear instability which leads to a characteristic "zig-zag" pattern of crack propagation at a mode I crack tip. Microvoid nucleation is a very significant strain-softening influence contributing to shear instability.

In addition to reducing any softening influence during plastic deformation, another approach to controlled flow stability is the superposition of a strain hardening contribution. A promising way to alter the constitutive behavior of the matrix is through transformation plasticity associated with dispersed austenite. Fig.1.2 depicts the definition of Dispersed-Phase Transformation Toughening which is the toughening mechanism that is investigated in this work. The interaction of deformation-induced transformation

of dispersed austenite with fracture-controlling processes, such as microvoid-induced shear localization, can lead to substantial improvements in fracture toughness. Transformation toughening is attributed partly to a modification of the stress-strain curve shape, and partly to a modification of the stress state because of the transformation volume change. In designing an austenitic dispersion for dispersed-phase transformation toughening, two important factors must be taken into consideration: the stability and the amount of austenite. The stability is controlled by the size and the chemical composition of the austenite particles. The size influences the probability of finding a nucleation site in the particle, and the composition influences the chemical driving force for the martensitic transformation.

The transformation toughening considered here should be differentiated from the transformation toughening found in TRIP steels where the transforming phase is fully austenitic. In the ultrahigh-strength steels under consideration in this work, the transforming phase is dispersed metastable austenite either in the form of retained austenite or precipitated austenite. The conventional retained austenite is the austenite that remains untransformed after quenching from the solution temperature. On the other hand, the precipitated austenite forms upon high-temperature tempering or intercritical annealing. An important difference between these two forms of dispersed austenite is the stability against martensitic transformation. Substantial transformation toughening can be achieved only if the austenite has an optimum stability which is quite high. This condition can be achieved by size refinement and by compositional enrichment of the precipitated austenite, parameters which can be controlled with heat treatment. This controlled metastability is not feasible with retained austenite. However, study of the transformation plasticity associated with retained austenite provides insight into its effects on mechanical behavior and helps

clarify the still controversial role of retained austenite on fracture toughness. For this reason, a VAR 4340 steel was chosen to study the effects of retained austenite, while precipitated austenite was examined in high Ni-Co secondary hardening steels.

The outline of this thesis is as follows. A background discussion is presented in Chapter 2 dealing with transformation plasticity, transformation toughening, and austenite precipitation. In Chapter 3 the experimental procedures used throughout this work are presented. Chapter 4 focusses on the transformation plasticity of retained austenite. The stability of retained austenite is characterized quantitatively as a function of stress state. Plastic-flow stabilization effects in pure shear are correlated with austenite stability. Finally in Chapter 4, a discussion of the microyielding transformation behavior of retained austenite is presented. Chapter 5 deals with precipitated austenite with emphasis on austenite stabilization. Multistep heat treatments for austenite stabilization are discussed, and experimental results arising from transformation toughening effects are presented. Chapter 6 presents a discussion on alloy design for enhanced transformation toughening at high-strength levels including control of transformation volume change through compositional modifications. Finally Chapter 7 summarizes the major conclusions of this thesis.

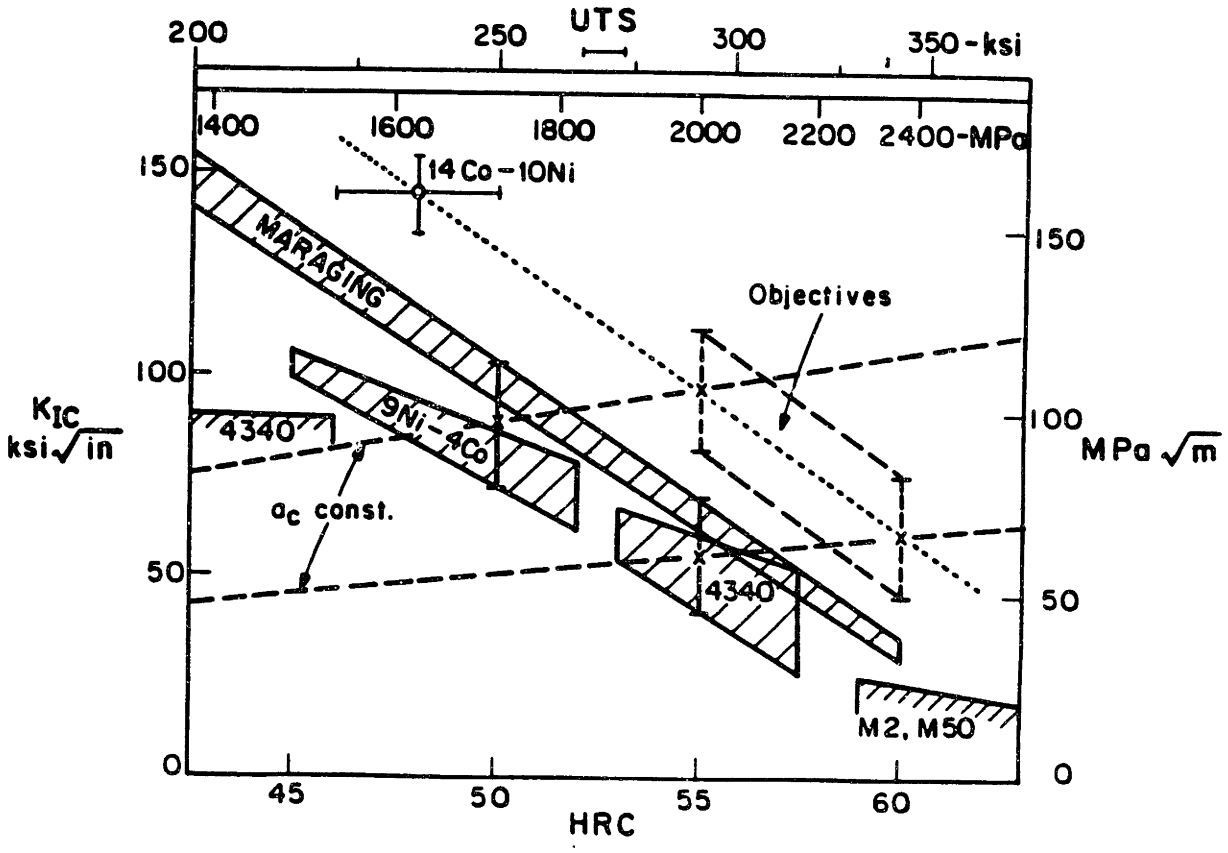

Fig.1.1 Strength / Toughness combinations in ultrahigh-strength martensitic steels.

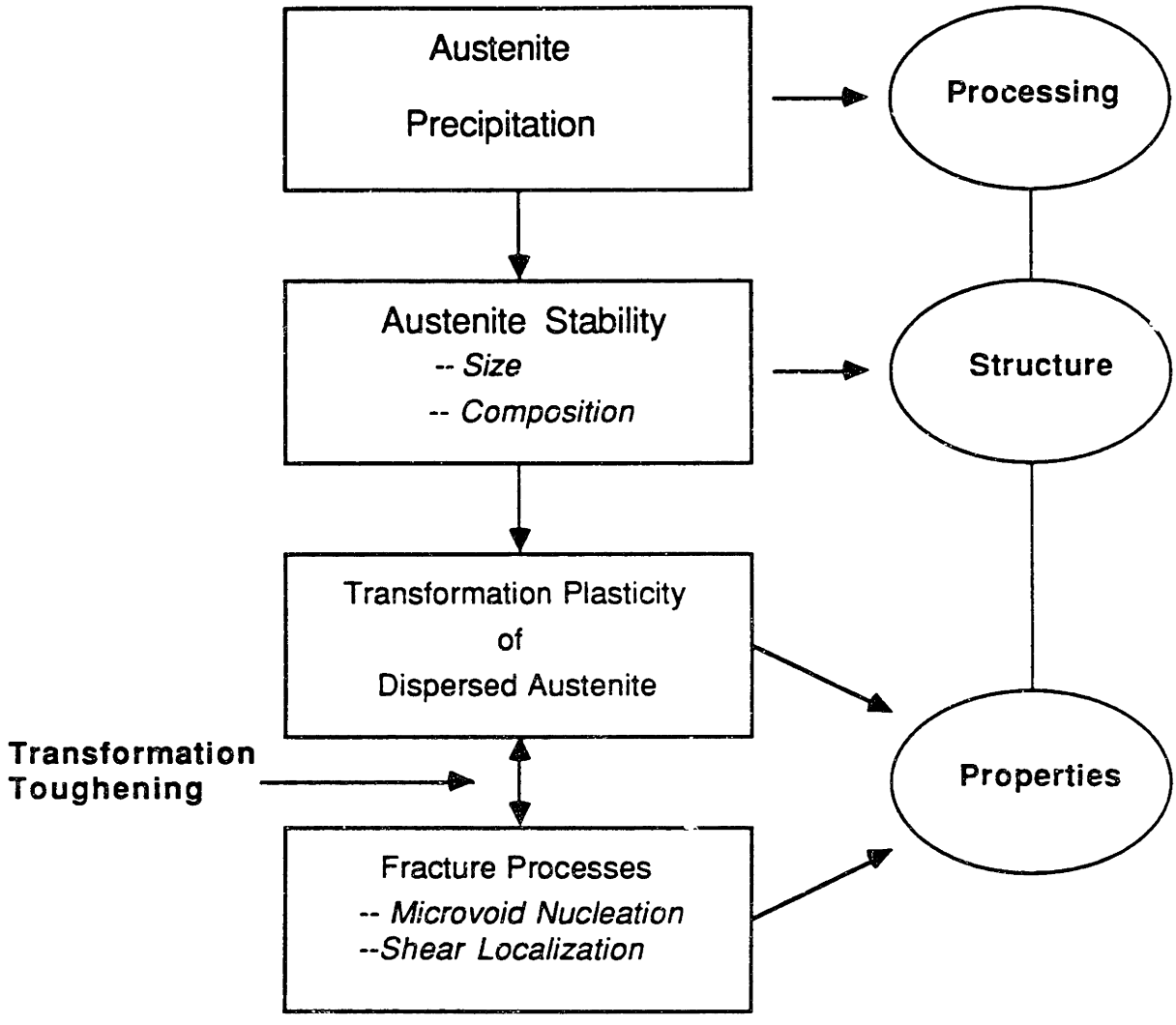

Fig.1.2 Definition of Dispersed-Phase Transformation Toughening as an interaction between transformation plasticity of dispersed austenite with fracture-controlling processes, in the context of structure / property relationships in materials science and engineering.

2. BACKGROUND

2.1 Dispersed-Phase Transformation Plasticity

Deformation can stimulate the kinetics of solid-state phase transformations through both the thermodynamic effect of the applied stress and the production of new catalyzing defects by plastic strain. For the case of martensitic transformations, these interactions are depicted in Fig.2.1 [1]. Spontaneous transformation triggered by pre-existing nucleation sites occurs on cooling to the M_S temperature (Point A). Stress-assisted nucleation on the same sites will occur at the stress denoted by the solid line indicated. At a temperature designated M_S^σ, this stress reaches the yield stress σ_y for slip in the parent phase (Point C). Above Ms^σ new potent nucleation sites, introduced by the plastic strain, trigger strain-induced nucleation (Line CE). The temperature Ms^σ thus defines an approximate boundary between the temperature regimes where separate modes of the transformation dominate; near the Ms^σ temperature both modes will operate. Due to transformation plasticity, the observed yield stress follows the stress for stress-assisted transformation below the Ms^σ (Line CA for athermal and line CA' for isothermal martensitic transformation). A reversal in the temperature dependence of the flow stress thus provides a convenient determination of the Ms^σ temperature.The Ms^σ temperature is then a quantitative characterization of the stability against stress-assisted transformation. Md is the maximum temperature above which martensitic transformation cannot be induced by deformation. Due to the interaction between stress triaxiality and transformation volume change, the Ms^σ and Md temperatures are stress-state dependent.

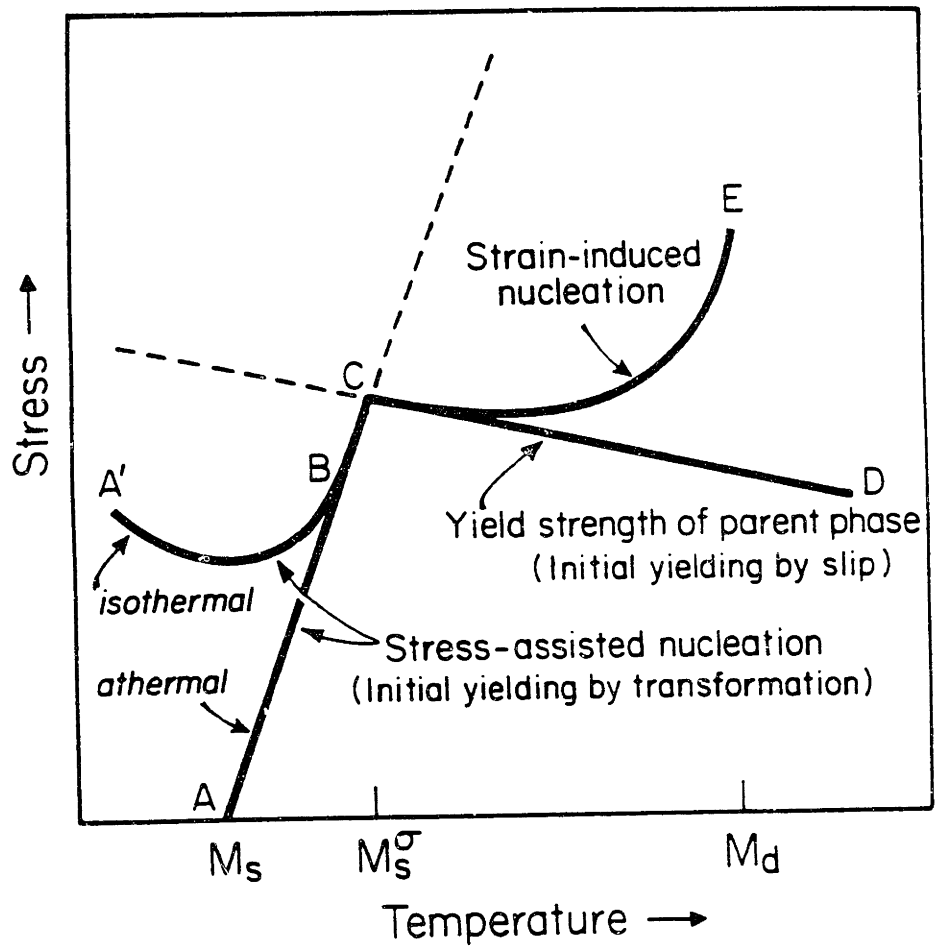

Fig.2.1 Schematic representation of stress-assisted and strain-induced regimes for mechanically-induced transformation. Below M_s^σ, initial yielding is controlled by transformation plasticity, and above M_s^σ by slip in the parent phase (from reference 1).

2.1.1 Stress-Assisted Transformation

For the case of stress-assisted nucleation, the applied elastic stress assists the transformation kinetics by modifying the effective potency distribution of the pre-existing nucleation sites. Based on a dislocation dissociation model of classical heterogeneous martensitic nucleation via elastic interactions with internal stress concentrations[2], the potency of a nucleation site can be expressed in terms of the thickness **n** (in numbers of crystal planes) of the nucleus that can be derived from the defect by barrierless dissociation. The critical n for nucleation at a given thermodynamic driving force per unit volume ΔG^{ch} is :

$$n = - \frac{2\,\gamma_s/d}{\Delta G^{ch} + E^{str} + W_f} \qquad (2.1)$$

where γ_s is the nucleus specific interfacial energy, **d** is the crystal interplanar spacing, E^{str} is the elastic strain energy per unit volume asscciated with distortions in the nucleus interface plane, and W_f is the frictional work of interfacial motion. Based on this model, Cohen and Olson[3] derived the cumulative structural defect-potency distribution $N_V(n)$, from the Cech and Turnbull small-particle experiments in Fe-30Ni [4].

$$N_V = N_V^0 \exp(-\alpha n) \qquad (2.2)$$

where N_V^0 is the total number of nucleation sites of all potencies and α is a constant.

The effect of the applied stress on the potency distribution can be found by adding a mechanical driving force term ΔG^{σ} to the chemical driving-force term ΔG^{ch} of eq(2.1), to obtain the total driving force:

$$\Delta G = \Delta G^{ch} + \Delta G^{\sigma} \qquad (2.3)$$

At a given stress level, the value of ΔG^{σ} changes with the orientation of the nucleus relative to the stress axis. The mechanical driving force due to a uniaxial elastic stress σ is then expressed as :

$$\Delta G^{\sigma} = \frac{\sigma}{2}\left\{\gamma_0 \sin(2\theta)\cos\alpha + \varepsilon_0(1+\cos(2\theta))\right\} \tag{2.4}$$

where γ_0 and ε_0 are the transformation shear and normal strains, θ is the angle between the applied stress axis and the normal to the habit plane, and α is the angle between the shear direction of the transformation and the maximum shear direction of the applied stress resolved on the habit plane.

In considering stress effects on the potency distribution, two limiting cases should be considered. A fully-biased distribution which is based on the assumption by Patel and Cohen[5] that the operative nucleation sites are of the optimum orientation for maximum interaction with the applied stress, such that $\Delta G^{\sigma}=\Delta G^{\sigma}_{max}$ for all sites. An opposite extreme is to consider a fully-random distribution, based on the assumption made by Olson, Tsuzaki, and Cohen[6] that the nucleation sites are randomly oriented. The actual behavior should be bounded between these two extremes. Olson, Tsuzaki, and Cohen found that in the stress-assisted regime the effect of the applied stress is approximately one third (1/3) of that predicted by the fully-biased distribution model. Therefore, the potency distribution of nucleation sites $N_V(\sigma)$, under an applied elastic stress σ, is given by the following expression :

$$N_v(\sigma) = N_v^0 \exp \frac{2\alpha\gamma_s / d}{\Delta G^{ch} + \Delta G^{\sigma}_{max} + W_f + E^{str}} \tag{2.5}$$

where for the fully-random distribution of nucleation sites, the term ΔG^{σ}_{max} should be replaced by $\Delta G^{\sigma}_{max}/3$.

The mechanical driving force is related to the applied stress through the expression:

$$\Delta G^{\sigma} = \sigma\left(\frac{\partial \Delta G}{\partial \sigma}\right)$$

The stress-assisted transformation of a well-spaced dispersion of metastable particles in a stable matrix is controlled by the pre-existing nucleation sites for which the potency distribution under an applied elastic stress σ is given by eq(2.5). For an average particle volume V_p, the fraction of particles to transform via sites of a potency with a cumulative number density N_V, is equal to the probability of finding at least one nucleation site in the particle, assuming that a single nucleation event transforms the particle to martensite. This probability is:

$$f = 1\text{-}\exp(-N_V.V_p) \tag{2.6}$$

From eq(2.1), the stress σ required to operate a nucleation site of a potency n_0 is linearly related to a parameter Φ of the form:

$$\Phi = \left[\sigma(-\partial\Delta G/\partial\sigma) - (\Delta G^{ch} + E^{str} + W_f)\right](d/2\gamma_s) = n_0^{-1} \tag{2.7}$$

For the potency distribution of eq(2.5), f and Φ are related by:

$$\Phi = \frac{\alpha}{\ln\left[-N_V^0.V_p/\ln(1-f)\right]} \tag{2.8}$$

Taking the plastic strain ε to be proportional to f, ($f=\varepsilon/\varepsilon_0$), with complete transformation giving a strain ε_0, the form of the Φ-f (σ–ε) curves predicted for various values of V_p normalized to $(N_V^0)^{-1}$ are shown in Fig.2.2. For small particles, a high strain-hardening rate arises from early exhaustion of the most potent sites, and further strain requires operation of less potent sites at higher stresses. The sigmoidal shape of the σ–ε curves

for stress-assisted transformation has been also observed for transformation plasticity in certain ceramic systems. Recent experiments by Chen and Reyes[7] have demonstrated sigmoidal σ–ε curves under combined pressure and uniaxial stress in MgO - partially stabilized zirconia ceramics.

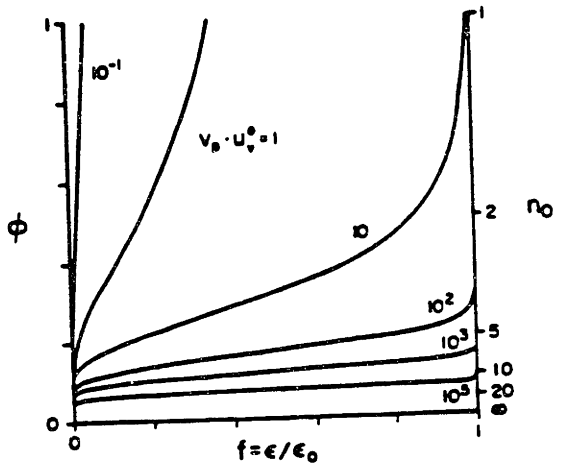

Fig.2.2 Stress-strain curves for stress-assisted transformation of a well-spaced dispersion of metastable particles in a stable matrix where the transformation is controlled by the pre-existing nucleation sites. Curves for various average particle sizes are shown. (from reference 6).

2.1.2. Strain-Induced Transformation

It was mentioned earlier that during strain-induced transformation new nucleation sites are created by plastic strain. The potency distribution of these sites can be found by making the assumption that these sites have an optimum orientation for maximum interaction with the applied stress (i.e. these sites are more potent than the pre-existing sites). In this case the mechanical driving force is $\Delta G^{\sigma}=\Delta G^{\sigma}max$ and therefore the potency distribution becomes:

$$N_v(\varepsilon) = N_v^0(\varepsilon)\ \exp\frac{2\ \alpha\gamma_s/d}{\Delta G^{ch}+\Delta G^{\sigma}_{max}+W_f+E^{str}} \qquad (2.9)$$

where all parameters have been defined earlier. However, note that N_V^O is now a function of plastic strain.

Recently, Kuroda[8] treated the strain-induced transformation of dispersed particles. He assumed that during strain-induced transformation, nucleation sites will be activated by the applied stress and created by the plastic strain, simultaneously. Taking these effects to be additive, the potency distribution of nucleation sites can be expressed as:

$$N_v = N_v^{00}\exp(-\alpha_o\, n_o) + N_v^0\exp(-\alpha_1\, n_1) \qquad (2.10)$$

where n_0 and n_1 are given by:

$$n_0 = -\frac{2\gamma_s/d}{\Delta G^{ch}+\Delta G^{\sigma}_{max/3}+W_f+E^{str}} \qquad (2.11)$$

$$n_1 = -\frac{2\gamma_s/d}{\Delta G^{ch}+\Delta G^{\sigma}_{max}+W_f+E^{str}} \qquad (2.12)$$

It can be seen that a fully-random distribution of nucleation sites is used for the stress-assisted part, while a fully-biased distribution is used for the strain-induced part. Then, invoking eq(2.6), the fraction of particles to transform can be expressed as:

$$f = 1 - \exp \{ - V_p [N_v^{00} \exp(-\alpha_0 n_0) + N_v^0 \exp(-\alpha_1 n_1)] \} \qquad (2.13)$$

The strain dependence of N_v^0 for strain-induced nucleation can be expressed as:

$$N_v^0 (\varepsilon) = N [1 - \exp (-K\varepsilon^n)] \qquad (2.14)$$

where N and K are constants. Kuroda used non-linear curve fitting to fit the above model with experimental data on the Cu-Fe system[9] and on a dual-phase steel[10].

While stress-assisted transformation ($T<M_S^\sigma$) represents a softening phenomenon relative to the flow behavior of the parent phase in the absence of transformation, above M_S^σ, where strain-induced nucleation dominates the transformation behavior, transformation and slip act as parallel deformation mechanisms. While a softening effect is still associated with the operation of the transformation as a deformation mechanism (*dynamic softening*), a hardening effect also arises from the transformation product as an obstacle to slip (*static hardening*). These two effects have been separated by pre-strain experiments, providing empirical constitutive relations for transformation plasticity [11]. A general characteristic of transformation plasticity is that dynamic softening is the dominant effect at low strains, while the static hardening dominates at high strains as the rate of transformation diminishes. The combined effect of these two contributions is to distort the usual

stress-strain curve to an upward-curving shape approximating an ideal "exponential hardening" behavior which imparts maximurn flow stability [12].

The flow-stabilizing influence of transformation plasticity has been demonstrated experimentally for retained austenite in dual-phase steels[13]. High-magnetic-field cryogenic treatments were used to vary the amount of retained austenite in an intercritically annealed 0.11C-0.55Si-1.4Mn steel. The tensile σ–ε curves are shown in Fig.2.3. Curve A represents the as-heat-treated material, curve B depicts the magnetic-field treated control material. Curves AT and BT represent specimens treated the same as A and B but tempered for 1h at 180°C to fully age the dislocation substructures in order to eliminate possible complications arising from additional mobile dislocations introduced by the magnetically-induced martensitic transformation in the B specimen. The amount of retained austenite as a function of plastic strain is also plotted in the same figure. The data in Fig.2.3 allow comparison of the flow behavior of materials with the same UTS and identical martensite contents at the UTS but with a difference in initial austenite content of Δf_γ=0.05. The transformation plasticity associated with transformation of this amount of austenite provides an additional increment of uniform ductility of 4 to 5% strain. The curve-shaping influence of relatively modest austenite contents is clearly a potent mechanism for enhanced control of the stability of plastic flow.

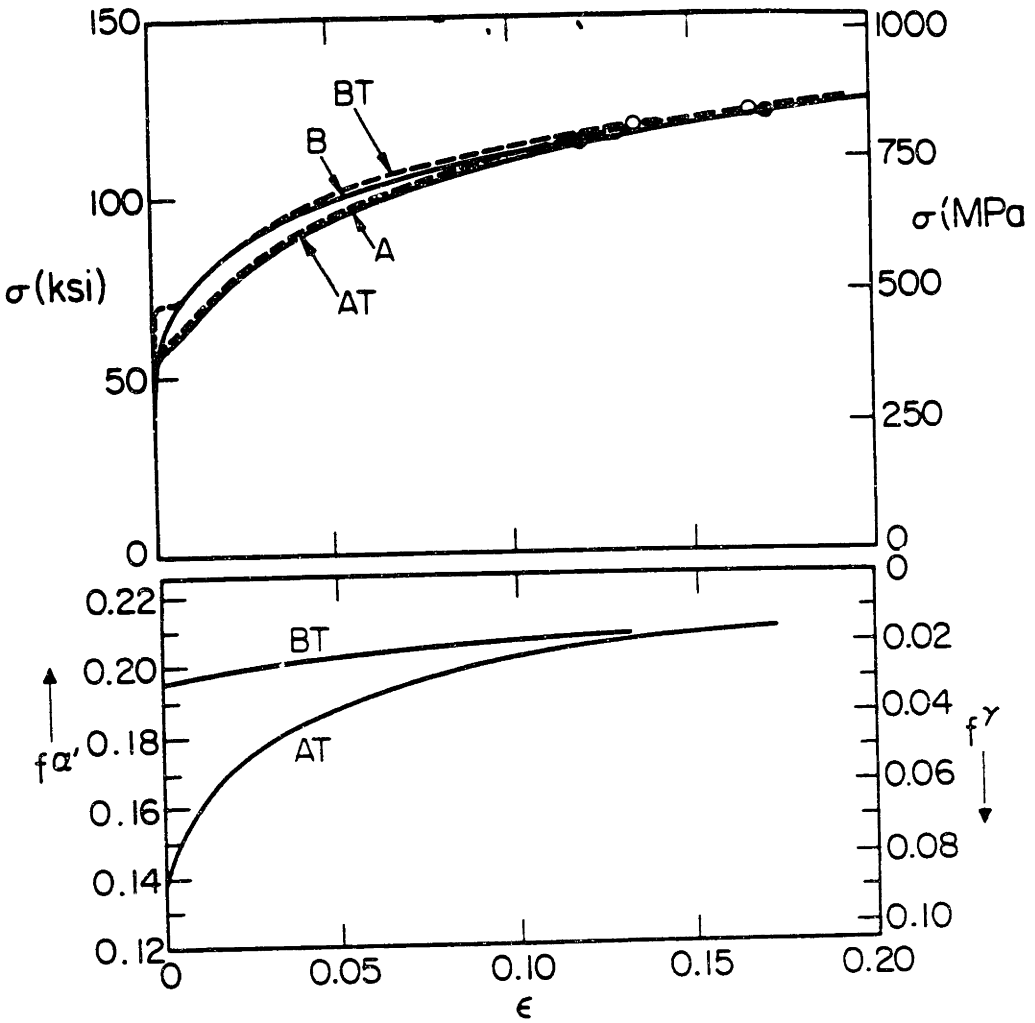

Fig.2.3 True stress-strain curves and corresponding martensite contents during tensile deformation of a dual-phase steel; curve A, as heat treated; curve B, magnetic-field treated; curves AT and BT, tempered 1/2 h at 180°C. Solid and open points indicate necking strains. (from reference 13).

2.2 Transformation Toughening

2.2.1 Ductile Solids

In ductile solids, such as ferrous alloys, transformation toughening has been investigated and has led to the development of TRIP steels[14]. Recent experiments in metastable austenitic steels have demonstrated that the flow-stabilizing influence of transformation plasticity can substantially enhance fracture toughness when fracture is controlled by shear instability[15]. Fig.2.4 summarizes the measured increment of J-integral toughness enhancement ΔJ_{IC} relative to the toughness of stable austenite J_{IC}^{A}, as a function of relative transformation stability, for a series of precipitation-hardened metastable austenitic steels. The relative transformation stability is expressed by a normalized temperature parameter θ, given by :

$$\theta = \frac{T-M_s^{\sigma}}{M_d-M_s^{\sigma}} \tag{2.15}$$

with $\theta>1$ ($T>M_d$) corresponding to stable austenite and $\theta\leq 0$ ($T\leq M_S^{\sigma}$) corresponding to stress-assisted transformation. Both the M_S^{σ} and M_d temperatures were experimentally determined for the crack-tip stress state. The shape of the $\Delta J_{IC}/J_{IC}^{A}$ vs θ behavior for shear-instability-controlled fracture is consistent with the effect of transformation plasticity on flow stability, indicating an optimum of crack-tip transformation near the M_S^{σ} temperature. Curves labeled HV in Fig.2.4 represent alloys with a relatively high transformation volume change of 4%, while LV represents a lower volume change of 2.5%. Toughness enhancement is clearly increased by a larger volume change. However, extrapolation to $\Delta V=0$ shows that even in the absence of dilatation, the σ–ε curve-shaping effect of transformation plasticity will delay shear instability.

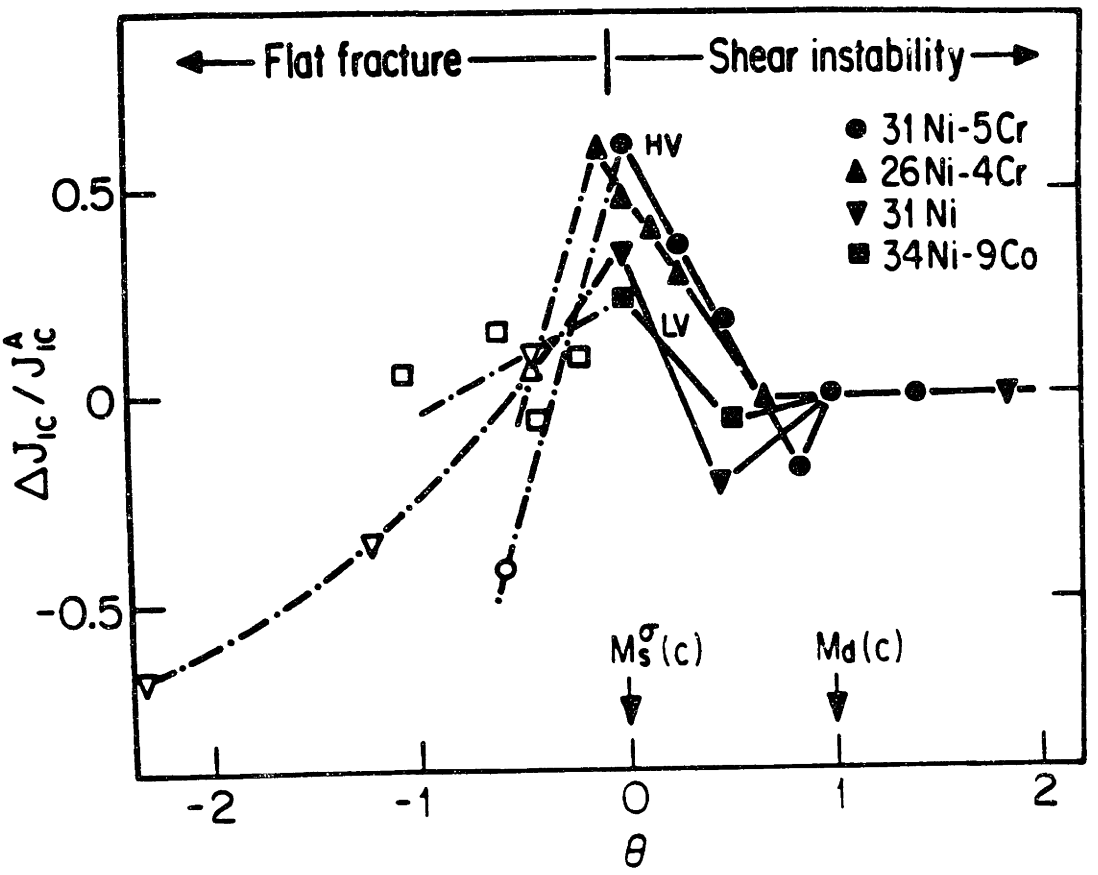

Fig.2.4 Increment of J-integral toughness enhancement ΔJ_{IC} relative to the toughness of stable austenite J_{IC}^{A} as a function of relative transformation stability, for a series of precipitation-hardened metastable austenitic steels. Curves labeled HV represent alloys with a relatively high transformation volume change of 4%, while LV represent a lower volume change of 2.5% (from reference 15)

Recent observations[16] of martensite forming around void-nucleating carbide particles during tensile deformation of a homogeneous metastable austenitic steel, suggest that transformation toughening can arise by suppressing microvoid nucleation to higher plastic strains.

2.2.2 Brittle Solids

The concept of dispersed-phase transformation toughening has been thoroughly investigated for the brittle ceramic systems failing by cleavage[17]. The most familiar example is the partially-stabilized zirconia ceramics (PSZ), where the metastable tetragonal precipitate is biased to transform to the monoclinic product phase by the intensified stress field ahead of a crack tip.

The strength / toughness relationships in these systems are illustrated schematically in Fig.2.5. When transformation toughening operates, the toughness K_C increases as the critical stress σ_C (at which the transformation nucleates) decreases. Then, when fracture is controlled by pre-existing flaws (of size a), the fracture strength varies as depicted in Fig.2.5. However, at low σ_C, another failure mechanism intervenes. As the critical transformation stress decreases, localized nonlinear deformation occurs in the form of shear bands which initiate fracture. At low σ_C then, failure is yield-limited causing the mechanism transition shown in Fig.2.5.

An analogy can now be made between transformation toughening in the brittle ceramic systems and in the ductile ferrous alloys. In both systems a characteristic peak toughening is associated with optimum transformation stability. In TRIP steels, Fig.2.4 indicates that peak toughness occurs at the M_S^{σ} temperature where the transformation mode changes from strain-induced to stress-assisted nucleation as the austenite stability decreases with decreasing temperature. On the other hand, in the PSZ ceramics the corresponding toughening peak is associated with the intervention of yield-limited fracture as the transformation stability is reduced.

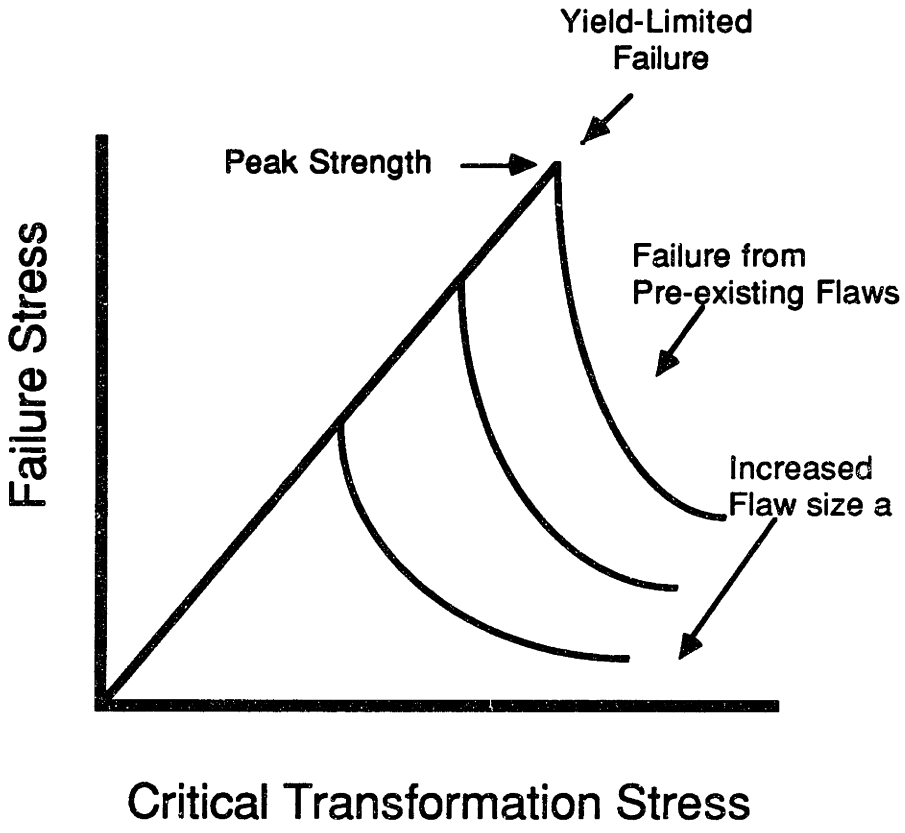

Fig. 2.5 Schematic representation of strength / toughness relations in zirconia-toughened ceramics. (From reference 17).

The toughness improvement in the ceramic systems has been rationalized in terms of the additional dissipative work of the transformation[18]. More recent models[19] indicate that the observed toughening is due to a reduction in the effective local stress intensity, caused by the volume change of the transformed particles which are left in the wake of the moving crack tip. In this case the toughening can be characterized by a stress intensity change ΔK, defined as:

$$\Delta K = K_{tip} - K_{\infty} \tag{2.16}$$

When $K_{tip} < K_{\infty}$, ΔK is negative and the transformation zone shields the tip from the applied loads. The change in stress intensity is given by:

$$\Delta K = - 0.22\ E\ f\ \varepsilon_{ii}^{T} \sqrt{h}\ /\ (1 - \nu) \tag{2.17}$$

where E is Young's modulus, ν is Poisson's ratio, ε_{ii}^{T} is the total dilatational transformation strain, f is the volume fraction of transforming particles, and h is the transformation-zone width [19].

2.3. Austenite Precipitation and Toughening Effects.

2.3.1 Austenite Precipitation Behavior

Mechanisms for austenite precipitation have been studied in low-carbon ferritic steels used for cryogenic applications[20-23], dual-phase steels[24-29], and high-strength tempered martensitic steels[30-33].

The Fe-Ni ferritic steels, which have been developed for structural use at cryogenic temperatures, are typically given a heat treatment which finishes with an intercritical temper at a relatively low temperature in the $\alpha+\gamma$ region. During the intercritical temper, austenite is precipitated within the prior martensitic matrix. If the tempering temperature is low and the tempering time is sufficiently long, a substantial

fraction of the precipitated austenite is retained after cooling to room temperature. Morris and co-workers[23] have developed a double tempering treatment (termed QLT) to promote the stability of the precipitated austenite in a Fe-5Ni steel. Enhanced stability results from the compositional enrichment of the interlath austenite. The austenite composition,.as determined by STEM microanalysis, was 8.8 Ni, 4.3 Mn, 3.2 Cr, balance Fe, which shows an enrichment in Ni, Mn, and Cr relative to the initial amounts of 5.8, 1.2,and 0.69 (w/o) in the steel. The QLT treatment consists of a two-step temper; 670°C/1h followed by 600°C/1h. The success of this treatment appears to result from the mode of austenite precipitation. The final austenite forms within regions previously enriched in Ni during the high-temperature step.

As discussed earlier, in addition to compositional enrichment, size refinement is also a very important parameter controlling the stability of precipitated austenite. This is because the austenite particle size influences the probability of finding a nucleation site in the particle. Size refinement can be achieved in two ways:

1. Tempering for short times to keep the austenite particle size small; and
2. Heterogeneous nucleation of austenite on another fine dispersion of second-phase particles, such as carbides.

The first method has been investigated by Marschall et al.[31], who showed that short times and low temperatures lead to more stable austenite. The second method has been investigated by Rao[34], who reported austenite nucleation on alloy-enriched cementite. In the latter case, a microalloyed steel with 0.16C and 1.5Mn (w/o) was tempered below the A3 temperature to partition Mn and C and to form fine, lenticular cementite particles. Then the steel was intercritically annealed (between the A1 and A3 temperatures). Relatively fine particles of austenite nucleated on the cementite particles which dissolved, thus enriching the austenite in C and Mn and enhancing the austenite stability.

2.3.2 Toughening Effects

While the effect of transformation plasticity on the toughness enhancement of homogeneous metastable austenitic steels is clearly evident, the toughening role of small amounts of dispersed metastable austenite in martensitic steels remains controversial. Toughness improvements associated with retained austenite have been reported for 4340 and 300M steels [35-38[as well as for tool steels [39]. Recent studies [40] indicate a decrease in toughness during the second stage of tempering, when the retained austenite decomposes to form interlath carbides. In Fe-Ni cryogenic steels, the toughness enhancement is associated with the presence of an austenitic dispersion, which is precipitated during intercritical annealing [41-43]. Similar phenomena have been observed in Fe-Mn steels [44].

Many attempts have been made in the past to clarify the toughening role of austenite dispersions. The most important explanations that appear in the literature are as follows:

1. Intrinsic toughness of dispersed austenite [38-45]. This explanation requires that the austenite be mechanically stable with respect to strain-induced transformation during the fracture process.

2. Scavenging action of austenite for carbon and other impurities from the ferritic matrix, which improves both low and high-temperature toughness [31-46].

3. Grain-refining effect of the austenite dispersions. In the Fe-Ni cryogenic steels, the austenite dispersions interrupt the cleavage planes in the martensitic matrix, thus refining the effective grain size of the alloy. According to Kim, Syn, and Morris [23], the austenite, which is located along the martensitic lath boundaries is transformed to martensite by the plastic deformation associated with the advancing crack. The crystallographic variant of the product is different from the dominant variant of the surrounding packet. The crystallographic alignment of the martensitic packets is then broken-up, resulting in an indirect grain-refining effect.

4. The transformation dilatation and the stress-strain curve-shaping effects of transformation plasticity improve the toughness of the homogeneous metastable austenitic steels when fracture is controlled by shear instability. The same mechanism should apply for dispersed austenite in martensitic steels, provided that the austenite has the optimum stability for the crack-tip stress state.

An attempt will be made in this work to correlate the toughening effects of dispersed austenite with its stability, since the stability is the most important parameter controlling the transformation behavior. This issue will be addressed for both retained and precipitated austenite.

3. EXPERIMENTAL PROCEDURES

3.1. Materials

The materials used in this work consisted of the following steels:

a) VAR 4340 steel, used to study the effects of retained austenite. This steel was supplied by the U.S. Army Materials Technology Laboratory.

b) AF1410 and 1410-4Mo steels, used to study the effects of precipitated austenite. These steels were supplied by Carpenter Technology Corporation.

The chemical compositions of the steels are listed in Table 3.1 (in w/o). AF1410 is a commercially available alloy with an excellent combination of strength and toughness[47,48]. The 1410-4Mo steel is based on the AF1410 matrix composition of 14Co-10Ni but with Cr taken out and Mo balanced to the C content in the stoichiometry of the Mo_2C strengthening phase for high coarsening resistance. The THERMOCALC software[49] was used to design the 1410-4Mo composition.

3.2. Heat Treatments

Two austenitizing treatments were adopted for the 4340 steel. A conventional 870°C and a high 1200°C, both for 1h. The material was oil-quenched and subsequently tempered to 200°C for 1h. A series of specimens received a high-magnetic-field cryogenic treatment (20 Tesla at -196°C for 1h) to reduce the amount of retained austenite.

The AF1410 steel was double vacuum melted (VIM/VAR). Then, a plate was forged from a 133x95 mm flat as follows:

Table3.1 Compositions of steels (w/o)

	1410-4Mo	1410-4Mo(L)	AF1410	VAR 4340
C	0.29	0.23	0.16	0.42
Co	14.06	14.17	14.25	-
Ni	10.20	10.24	10.15	1.74
Mo	3.88	3.96	1.05	0.21
Cr	0.01	0.06	2.10	0.89
Mn	<0.01	<0.01	0.02	0.46
Si	<0.01	<0.01	0.01	0.28
P	<0.005	<0.005	0.003	0.009
S	0.003	0.003	0.002	0.001
Fe	bal.	bal.	bal.	bal.

a) 133x95 mm to 165x38 mm from 982°C

b) reheat to 982°C

c) 165x38 mm to 190x25 mm

d) air cool

e) normalize (900°C/1h, AC)

f) overage (677°C/6h, AC)

Austenitizing treatments were performed for 1h at 830 to 885°C, followed by oil quenching. Tempering was carried out over a range of temperatures (400-600°C) and times (15min-several hours). For the short-time temperings, the specimens were immersed in a neutral salt bath which was maintained at ±1°C from the desired temperature. For longer tempering treatments (t>1h), the specimens were encapsulated in argon-containing quartz tubes to avoid decarburization during heat treatment.

A similar procedure was followed for the 1410-4Mo steel with the exception of a homogenization treatment (1200°C/8h) in a vacuum furnace followed by furnace cooling prior to austenitizing.

3.3. Electron Microscopy

3.3.1 Transmission Electron Microscopy

TEM was used to observe the austenite particles and determine their size, morphology and distribution. Two electron microscopes were available; a PHILLIPS EM400 operating at 120 KV, and a JEOL 200 CX operating at 200 KV. In both cases, a double-tilt specimen holder was employed. In order to identify the austenite particles, the BF/DF technique was used. A selected-area diffraction pattern was taken on the bright-field image. FCC diffraction spots were then aligned with the optic axis and a dark-field image was generated by

letting only the FCC diffracted beams pass through the objective aperture of the microscope.

Specimen preparation for the TEM consisted of the following:

a) wafering the samples down to 20-30 μm using a STRUERS ACCUTOM machine with SiC blades operating at 800 rpm

b) punching 3 mm diameter disks

c) thinning to ~5 μm on 400 and 600 grit emery papers

d) electropolishing, with a Fischione twin jet electropolisher operating at 12 V. The polishing solution consisted of 20% perchloric acid in methanol. The solution temperature was maintained at -10°C during polishing, using a mixture of acetone and dry ice as the cooling medium. To avoid oxidation of the prepared foils, microscopy was performed within 24 h from the completion of polishing.

3.3.2 Scanning-Transmission Electron Microscopy

High-resolution STEM microanalysis (energy dispersive X-ray microanalysis) was used to determine the chemical composition of the austenitic particles, which is a very important factor characterizing the stability of the dispersed austenite. A dedicated VG HB5 field-emission STEM operating at 100 kV was employed. The instrument was equipped with a high resolution windowless X-ray detector.

A counting time of 100 sec was adopted in collecting the X-rays to improve the statistics. Standard samples were used for the deconvolution of the overlapping peaks of Fe, Co, and Ni. A computer program was written to carry out the necessary calculations for the deconvolution and to perform straightforward Cliff-Lorimer analysis. This procedure is discussed in Appendix A

Most of the particles analyzed were hanging from the matrix into the perforation of the foil. Therefore, X-ray signals from the matrix did not contribute to the total number of X-rays counted. Several other particles located in very thin areas very close to the perforation but embeded or semi-embeded in the matrix were analyzed. In most cases the X-ray spectra from these particles were very similar to those of the hanging particles, and then the average X-ray count was considered in the determination of the particle composition.

Convergent beam electron diffraction patterns (microdiffraction) were obtained in several cases in order to identify the austenite particles in the STEM.

3.3.3 Scanning Electron Microscopy

The SEM was used to characterize fracture surfaces of broken CVN or J_{IC} test samples. An AMR 1000 SEM operating at 20 KV was employed. The fracture surfaces were previously coated with Au.

3.4. X-Ray Diffraction

The volume fraction of dispersed austenite was determined by the standard "direct comparison" X-ray diffraction technique[50] where the integrated intensity of an austenite line is compared to that of a martensite line. In the present study, the average integrated intensities of the (220) and (311) austenite peaks were compared to the (211) and (200) martensite peaks. The integrated intensity was taken to be the area below each corresponding peak after background subtraction. Specimens with area ≥ 1.5 cm^2 were prepared by usual metallographic grinding and polishing procedures. A DIANO diffractometer with vanadium-filtered CrK_α radiation was used, operating at 35 kV and 15 ma.

Fe, Ni, and Co have small differences in atomic scattering factors. Therefore, compositional effects on the integrated intensities were not expected to arise from these elements. However, Mo has a relatively high atomic scattering factor and Mo remaining in solution could conceivably contribute to the measured integrated intensity of the martensite peak. On the other hand, in all cases examined, the precipitation of M_2C carbides (M=Mo, Cr, Fe) was complete and therefore the Mo effects were negligible. A more important error in the determination of the volume fraction of retained austenite could arise from preferred orientation in the samples, but other combinations of diffraction peaks were found to yield similar results, indicating that texture was not an important factor in these measurements.

3.5. Electrical Resistivity Measurements.

Samples for resistivity measurements were cut from quenched and tempered bars on the Struers Accutom wafering machine using SiC blades. The samples were 4cm long and about 1.5mm square in cross section. Pure nickel lead wires insulated with teflon tubes were spot welded to each end of the samples for the measurements. A Keithley milliohmmeter was used to measure resistance with a rated accuracy of ±5%. The resistance and resistivity are related with the formula:

$$\rho = R\frac{L}{A} \tag{3.1}$$

where ρ is the resistivity, R is the resistance, A is the cross-sectional area of the sample, and L is the length of the sample. The measurements of L and A introduce additional errors in the calculation of the resistivity from eq(3.1). However, the resistance of each sample was measured in the as-quenched as

well as in the tempered condition and relative changes in the resistivity were calculated from eq(3.1) as follows:

$$\frac{\rho_T}{\rho_Q} = \frac{R_T}{R_Q} \tag{3.2}$$

The sensitivity of these measurements then was limited only by the accuracy of the milliohmmeter, ±5%.

A number of different measurements were performed in order to follow the precipitation of austenite. The resistance was measured first in the as-quenched condition. Then the samples were tempered and the resistivity was measured again at room temperature. Finally, the samples were immersed in a bath of liquid nitrogen and the resistivity was measured again. In this way, transformation of the precipitated austenite could be detected. In some instances, the resistivity was measured at the tempering temperature vs time. In this case, a tube furnace was used with the Ni lead wires extending out of the opposite ends of the furnace and linked to the milliohmmeter.

3.6. Saturation Magnetization Measurements

Magnetic measurements were performed to determine the volume fraction of retained austenite in 4340 steel and to monitor austenite precipitation in the 1410-4Mo steel.

The samples were 3mm diameter disks that were cut from heat-treated rods with a slow-speed diamond saw. The magnetization of the samples (emu) was measured as a function of applied magnetic field (KOe), using a DMS vibrating sample magnetometer. Fields up to 15 KOe were used. A computer-

driven X-Y plotter provided plots of M vs H, where M is the normalized magnetic moment (emu/gr) and H the applied magnetic field (KOe). Using data from these plots, the magnetization was plotted vs $1 / H^2$ and the saturation value was determined by extrapolating a least-squares fit through the data to infinite applied field ($1/H^2=0$).

The volume fraction was measured using the following procedure. In a sample containing f_γ volume fraction retained austenite (paramagnetic) and $1-f_\gamma$ martensite (ferromagnetic), the saturation magnetization M_{sat} of the sample is given by a simple rule of mixtures:

$$M_{sat} = f_\gamma M_{sat}^{\gamma} + (1 - f_\gamma) M_{sat}^{\alpha} \qquad (3.3)$$

where M_{sat}^{γ} and M_{sat}^{α} are the saturation magnetizations of 100% austenite and 100% martensite respectively. Since $M_{sat}^{\gamma} << M_{sat}^{\alpha}$, eq(3.3) can be written:

$$M_{sat} = (1 - f_\gamma) M_{sat}^{\alpha} \qquad (3.4)$$

so that f_γ can be determined if M_{sat}^{α} is known. In order to measure M_{sat}^{α}, a sample of ferromagnetic martensite was prepared by tempering the 4340 steel at 300°C for 1h to decompose the retained austenite. The saturation magnetization of this sample was taken to be M_{sat}^{α}. The effects of carbides on the saturation magnetization were taken to be negligible due to their low volume fraction.

A similar procedure for determining the volume fraction of precipitated austenite in the high Ni-Co steels was not successful because the saturation magnetization was found to be sensitive to compositional changes during

tempering. The magnetization increased as Mo precipitated out of solution to form Mo_2C carbides. However, because of the paramagnetic nature of the austenite, the saturation magnetization decreased rapidly when austenite precipitated. This technique, therefore, was found useful in monitoring austenite precipitation and its stability during tempering.

3.7. Mechanical Testing

3.7.1 Tension and Compression Testing

Tension and compression testing was performed in an INSTRON 1125 testing machine at a nominal strain rate of 10^{-4} s^{-1}. The tensile specimens complied with TR-6 specifications and are shown in Fig.3.1. The compression specimens were cylindrical, having 15mm length and 6mm diameter.

3.7.2 Single-Specimen Technique for M_S^{σ} Determination

A single-specimen technique originally developed by Bolling and Richman[51] was used to determine the M_S^{σ} temperature in tension and compression. The technique involved monitoring of the 0.2% flow stress as a function of temperature. The M_S^{σ} could be determined from a reversal in the temperature dependence of the flow stress. Starting at a high temperature, the specimen was loaded up to the 0.2% flow stress. Then the specimen was unloaded by 10% and the temperature was lowered by 10°C. The specimen was then reloaded to the new 0.2% flow stress. The procedure was repeated at progressively lower temperatures. A silicone oil bath heated by an electric resistance provided the heating medium for T>25°C. A mixture of dry ice and methanol or a mixture of liquid nitrogen and ethanol was used for T<20°C. The

temperature was measured with a thermocouple attached to the gage section of the specimen. The bath was stirred at all times to ensure temperature uniformity.

3.7.3 Determination of Elastic Limit

The tensile elastic limit was determined as a function of temperature in order to measure the M_s^{σ} temperature of the retained austenite in the tempered 4340 steel. The technique, also described by Muir et al.[52], employed a load-unload procedure in order to monitor the load as a function of residual strain. This procedure was repeated with increasing load to determine the load that resulted in the first detectable positive residual strain. The strain was measured with an accuracy of $\pm 10^{-5}$ using sensitive strain gages mounted on the gage section of the tension specimens. Because the test was conducted as a function of temperature in a silicone-oil bath, a dummy strain gage mounted on an identical unloaded test specimen immersed in the bath was provided for temperature compensation.

3.7.4 Thin-Wall Torsion Testing

Thin-wall torsion testing was conducted in order to determine the effects of retained austenite in delaying shear instability under pure shear deformation. Thin-wall torsion specimens with hexagonal ends were used (Fig.3.2). The tests were performed in an Instron 1125 testing machine at a nominal strain rate of $10^{-4}\ s^{-1}$. Shear strain profiles were determined from grid patterns that were formed on the gage section of the torsion specimens. For this purpose, a 200 mesh Ni grid was attached on the gage section. A Au-Pd coating was then applied in a vacuum evaporator. The Ni grid was then removed leaving a fine

grid pattern on the specimen that allowed local measurements of shear strain to be made.

3.7.5 Fracture Toughness Testing (CVN and J_{IC})

Charpy V-notch impact testing, according to ASTM E23 [53], was performed to assess the blunt-notch fracture toughness of the AF1410 steel subjected to various heat treatments. The standard Charpy specimen was used, which is shown in Fig.3.3. The longitudinal axis of the specimen corresponded to the L-T orientation. The specimens were machined after heat treatment and were tested in a Physmet Charpy Machine with full capacity of 163 J.

While CVN testing provides information about the blunt-notch toughness of a material, K_{IC} or J_{IC} test procedures are used to assess the sharp-crack fracture toughness. For very ductile alloys, such as AF1410, validity requirements for K_{IC} tests specify very large specimen thicknesses. For AF1410 the required thickness is in excess of 1 inch according to ASTM E399 [54]. Critical J values for the onset of crack growth and J-based crack-growth resistance curves are the most promising candidates for elastic-plastic material characterization and ductile failure assessment. Besides the multiple-specimen interrupted-loading method described by the ASTM standard for J_{IC}, ASTM E813 [55] single-specimen procedures have become available and they form the basis of a tentative test procedure for determining crack-growth resistance curves (R-curves) [56].

A three-point bend specimen, shown in Fig.3.4, was used in this work. The specimen axis corresponds to the L-T orientation. Fatigue precracking was performed on an INSTRON 1331 servohydraulic machine above the anticipated M_d temperature of the precipitated austenite (100°C) to avoid transformation of

the precipitated austenite during precracking. A heating tape was attached to heat the specimen to the required temperature. J_{IC} testing was performed on an INSTRON 1125 machine.

The single-specimen technique eliminates the effect of material variability on the R-curve. Instead of using the interrupted-loading technique, the increasing crack length can be inferred from successive measurements of the elastic compliance $C=\Delta v/\Delta P$ of the specimen that is derived from small superimposed unloadings ($\Delta P=0.1P$) and a known function $a=f(C,B,E)$, where v is the displacement, P is the load, a is the crack length, B is the specimen thickness, and E is Young's modulus[57].The compliance was measured from the unloading slope. For this purpose the unloading slopes were amplified to increase the accuracy of the measurements. In this work, only part of the unloading slope was used to determine the compliance because of nonlinear behavior at the beginning and at the end of unloading. This nonlinear behavior is due to machine and fixture relaxations. To minimize these effects, the load was allowed to relax before unloading. Compliance calculations were done using the slope of the unloading curve between 15 and 70% of the maximum load.

The following equation was used to calculate the crack length from the compliance measurements[58]:

$$\frac{a}{W} = C_0 + C_1 U + C_2 U^2 + C_3 U^3 + C_4 U^4 + C_5 U^5 \qquad (3.5)$$

with

$$U = \frac{1}{\sqrt{E' C B} + 1}$$

where $E'=E/(1-\nu^2)$ for plane strain, C is the compliance and B is the specimen thickness.

For the three-point bend specimen, the coefficients C_i were taken to be [59]: $C_0=.994$, $C_1=-3.492$, $C_2=-2.740$, $C_3=-101.362$, $C_4=1289.364$, $C_5=-4545.959$.

The value of J was calculated from the equation:

$$J = \frac{2A}{B b} \tag{3.6}$$

where A is the area under the load vs. load-point displacement curve and b=W-a is the remaining uncracked ligament. With the values of J from eq(3.6) and the values of the crack length from eq(3.5), the R-curve (J vs. Δa) was constructed for each specimen and the J_Q value was determined. The procedure was subjected to the qualification requirements set by ASTM E813[54].Finally J_{IC} was taken to be equal to J_Q if:

$$B \text{ and } W - a_0 > \frac{25 J_Q}{\sigma_0}$$

where

$$\sigma_0 = \frac{\sigma_y + \sigma_{UTS}}{2}$$

A	B	C	D	E	F
57.14	12.70	4.06	0.125R	25.40	0.32

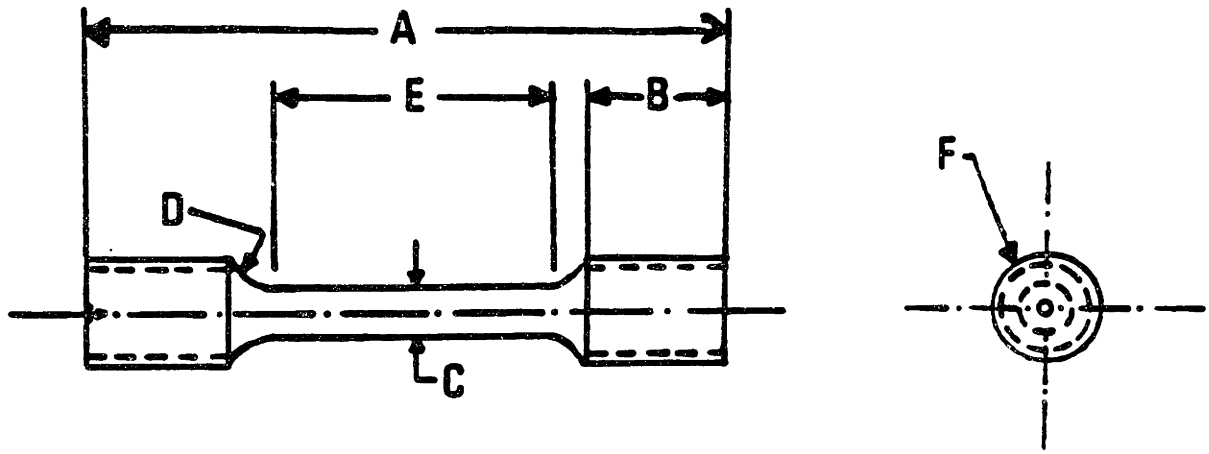

Fig.3.1 Tensile specimen. Dimensions in mm.

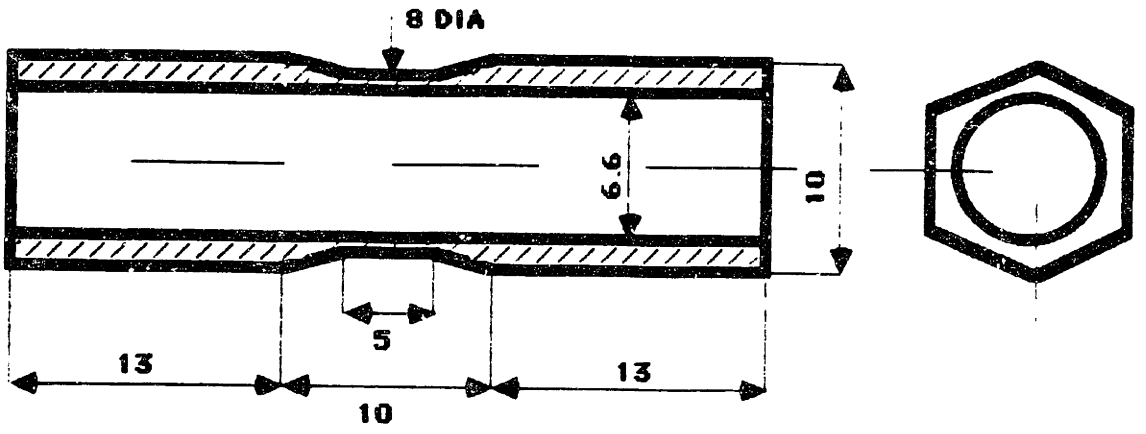

Fig.3.2 Thin-wall torsion specimen. Dimensions in mm.

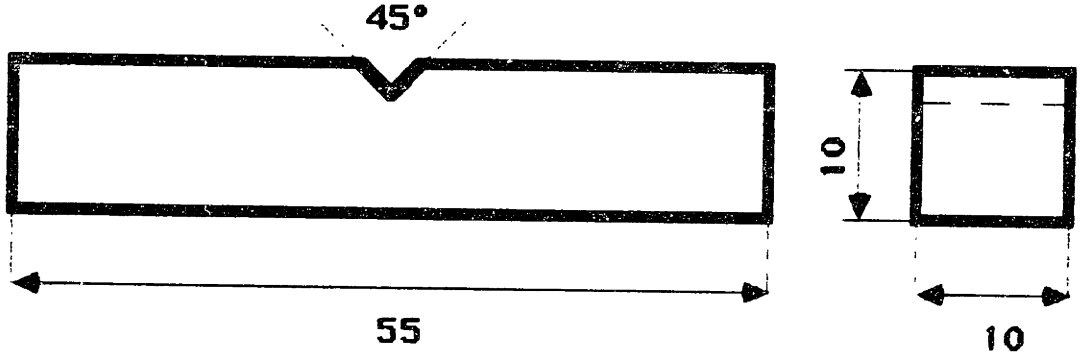

Fig.3.3 Charpy-V-Notch specimen. Dimensions in mm.

A	B	C	D	E
53.34	5.08	1.14	11.43	5.715

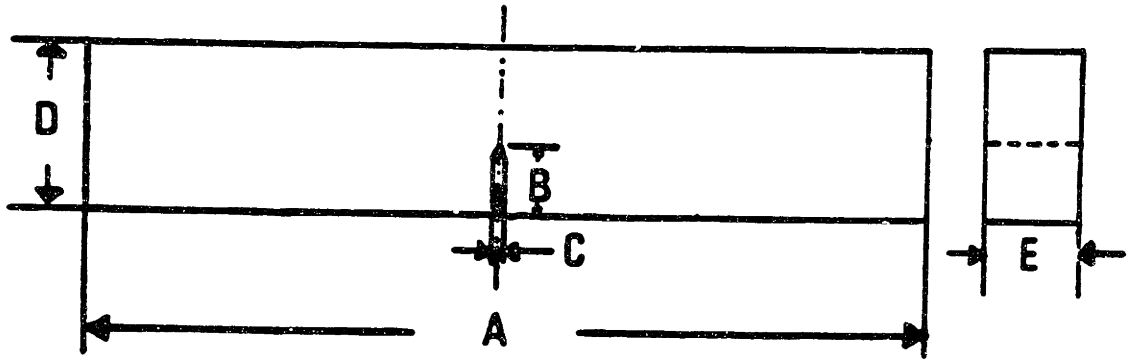

Fig.3.4 Three-point bend fracture toughness specimen for J-integral testing. Dimensions in mm.

4. RETAINED AUSTENITE

4.1 Introduction - Controlled Heat Treatments

Retained austenite is the form of dispersed austenite that remains untransformed after quenching from the austenitizing temperature. The alloy system selected to study the transformation plasticity associated with retained austenite was a VAR 4340 steel. Controlled experiments were designed to isolate the role of retained austenite. For this purpose, high-magnetic-field cryogenic treatments were used to reduce the amount of retained austenite in otherwise identically treated specimens. Two austenitizing treatments were used, 870°C and 1200°C for 1h. The specimens were oil-quenched and tempered at 200°C for 1h. The amount of retained austenite was determined by measuring the saturation magnetization of pre-weighed samples, using a vibrating sample magnetometer. Table 4.1 shows the four different treatments used, the resulting volume fraction of retained austenite, and corresponding hardness.

Table 4.1 Controlled Heat Treatments for 4340 Steel.

Austenitizing Temperature	Treatment	Volume Fraction Retained Austenite	Hardness (Rc)
870°C	200°C/1h	4.0%	54.0
870°C	20 Tesla/1h/-196°C 200°C/1h	2.5%	53.5
1200°C	200°C/1h	9.0%	53.3
1200°C	20 Tesla/1h/-196°C 200°C/1h	6.8%	53.4

4.2 Characterization of the retained austenite stability. M_s^σ temperatures.

It was mentioned earlier that the M_s^σ temperature provides a quantitative characterization of the stability of dispersed austenite. For this purpose, the M_s^σ temperature was measured in uniaxial tension, M_s^σ(u.t), and uniaxial compression, M_s^σ(u.c). A single specimen technique, originally developed by Bolling and Richman[50] was used. The temperature dependence of the 0.2% flow stress in tension and compression are shown in Fig.4.1a for the material containing 9% retained austenite (1200°C austenitizing temperature). Both flow stresses increase with decreasing temperature as expected from the thermally-activated flow theory. However, the tensile flow stress undergoes a plateau region, starting at about 40 to 50°C. At this temperature yield-point phenomena appear, which increase in magnitude with decreasing temperature. These yield points (designated Y.P. in Fig.4.1a) should not be attributed to strain aging, which being thermally activated, should disappear with decreasing temperature.* They are, instead, attributed to mechanical relaxations associated with the transformation of retained austenite. It is important to note the absence of a complete reversal of the flow stress such as that shown schematically in Fig.2.1. This is because the 0.2% flow stress is a composite flow stress, controlled by the flow properties of both martensite and retained austenite. Therefore, the M_s^σ(u.t) temperature corresponds to the onset of the plateau region and yield-point phenomenon (40-50°C). Smooth yielding dominates the

* The hold time between each loading cycle was kept constant in these tests.

compressive flow stress down to about -25°C, where again the yield-point phenomenon appears. Here M_s^{σ}(u.c)=-20 to -30°C.

The corresponding results for the steel containing 4% retained austenite (870°C austenitizing temperature) are shown in Fig.4.1b. A plateau region is absent in this case due to the much lower amount of retained austenite. However, the tensile flow stress undergoes an inflection at about 10 to 20°C. The transition from smooth yielding to discontinuous yielding also occurs in the same temperature range, indicating that M_s^{σ}(u.t)=10 to 20°C. No yield points were observed for the compressive flow stress indicating that M_s^{σ}(u.c)<-50°C

From the flow stresses in tension and compression, the strength-differential effect (S-D)# was calculated and plotted vs temperature in Fig.4.2. The steel that contains 4% retained austenite exhibits the normal S-D behavior, i.e, a few percent in magnitude and slowly increasing with decreasing temperature. However, the steel that contains 9% retained austenite exhibits a quite different S-D behavior. Approaching the M_s^{σ}(u.t) from high temperatures, the S-D undergoes a local minimum and then assumes high values of up to 7% where it shows a second local minimum at the M_s^{σ}(u.c). It is interesting to note that around the M_s^{σ}(u.t) the S-D effect assumes negative values, corresponding to a higher yield stress in tension. Such "pre-transformation strengthening" has also been observed in TRIP steels and has been attributed to dislocation core-structure rearrangements just prior to the general transformation[60]. The local minima in the temperature dependence of the S-D effect can be used to define the approximate M_s^{σ} temperatures for the corresponding stress states.

The strength-diferential effect is defined as S-D = $2(\sigma_c-\sigma_t)/(\sigma_c+\sigma_t)$, where σ_c and σ_t are the flow stresses in compression and tension respectively.

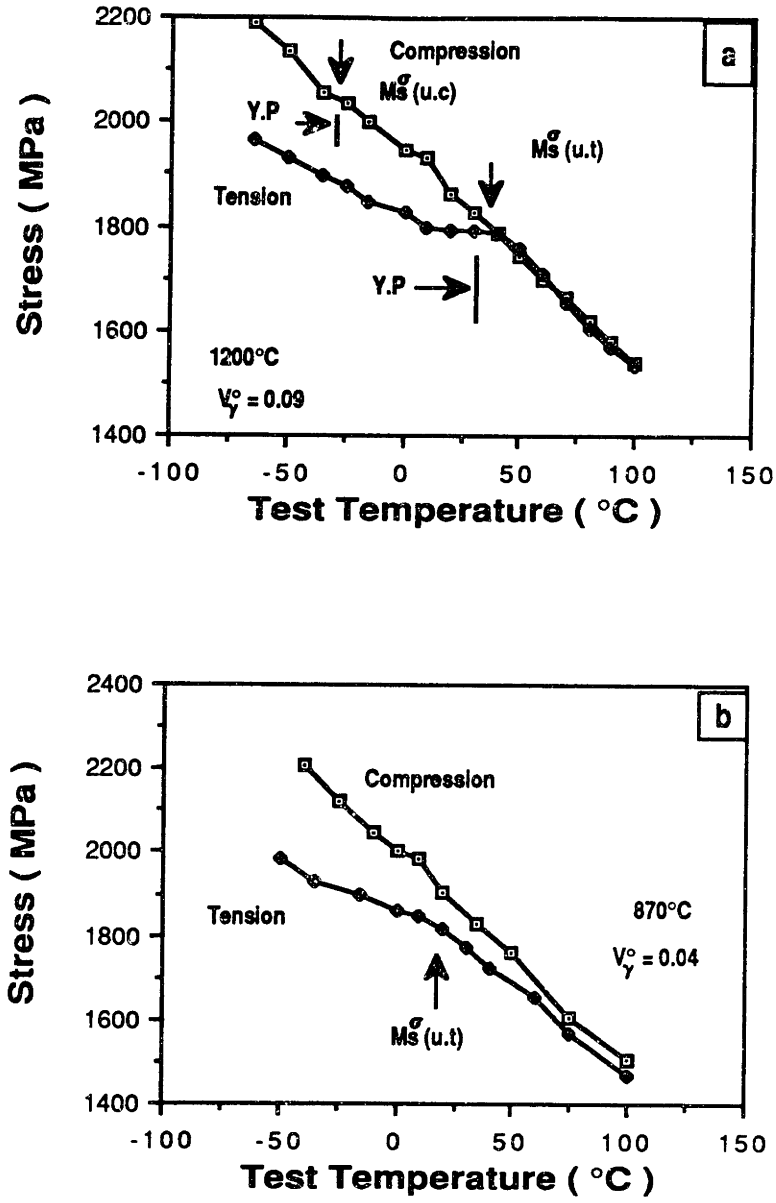

Fig.4.1 Temperature dependence of the 0.2% tensile and compressive flow stresses determined with the single-specimen technique, indicating the M_s^σ temperatures. Y.P denotes the transition from smooth yielding to yield-point phenomena. (a) is for the 1200°C austenitizing temperature and (b) is for the 870°C austenitizing temperature.

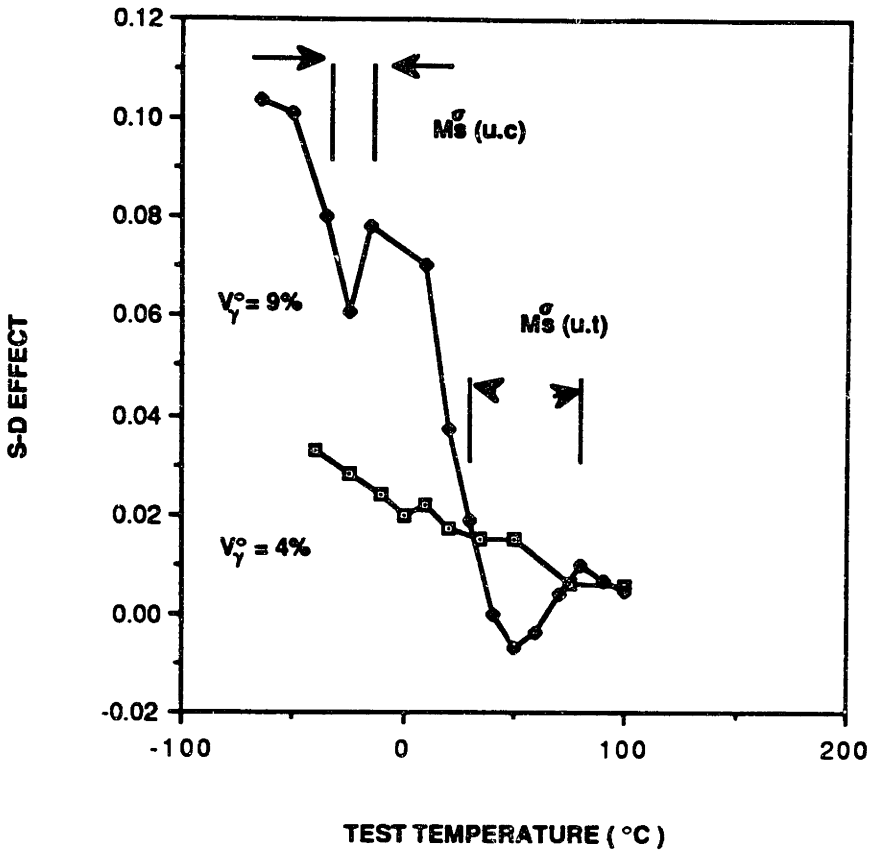

Fig.4.2 Temperature dependence of the strength-differential effect (S-D) for two different volume fractions of retained austenite in 4340 steel. The 9% retained austenite is for the 1200°C austenitizing temperature while the 4% retained austenite is for the 870°C austenitizing temperature. The arrows indicate the M_s^σ temperature ranges determined by the local minima in the S-D vs temperature behavior.

4.3. Transformation Microyielding of Retained Austenite.

4.3.1 Temperature dependence of the elastic limit.

The elastic limit was measured in tension with a load-unload technique that is described in chapter 3. The measurements were performed on a VAR 4340 steel austenitized at 1200°C and tempered at 200°C for 1h. The volume fraction of retained austenite was found to be 0.09 as measured by a vibrating-sample magnetometer.

The temperature dependence of the elastic limit is shown in Fig.4.3. The 0.2% flow stress and smaller-strain offsets are also indicated in the same figure. A definite reversal of the temperature dependence occurs at 40°C designating the tensile M_s^{σ} temperature of the retained austenite. However, the 0.2% flow stress does not undergo a reversal, consistent with the behavior obtained from the single-specimen technique.

Fig.4.4 presents stress-strain curves obtained in the microyielding region at temperatures above and below M_s^{σ}. Above M_s^{σ}, the stress-strain curves have the normal downward-curving shape, while below M_s^{σ} the stress-strain curves have a sigmoidal shape characteristic of stress-assisted transformation.

4.3.2. Constitutive Behavior in the Microyielding Regime.

In the stress-assisted nucleation regime ($T<M_s^{\sigma}$), initial yielding is controlled by the transformation of the retained austenite. Therefore, the theory of martensitic nucleation can predict the constitutive behavior of the steel in the microyielding regime. The observed stress-strain behavior can be understood by considering the effect of stress on the nucleation-site potency distribution[61].

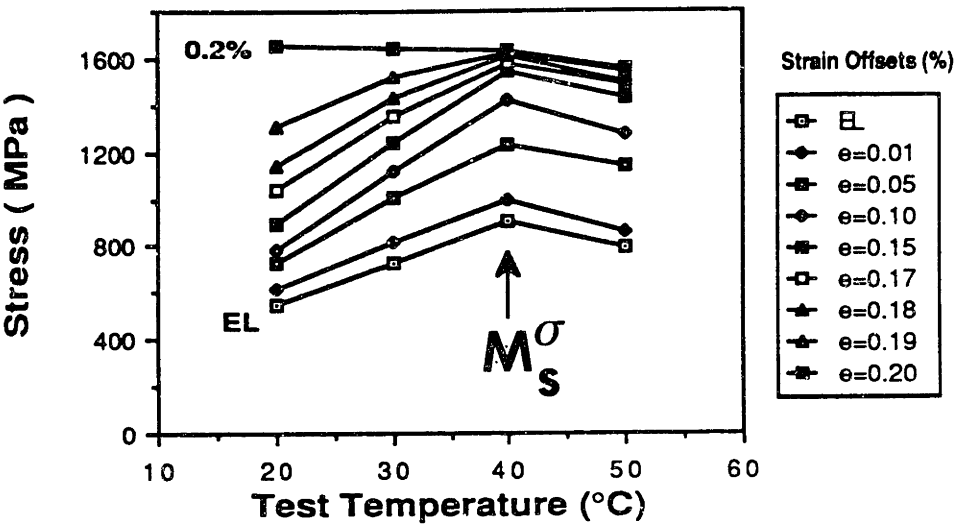

Fig.4.3 Temperature dependence of the elastic limit (EL) and strain offsets between the elastic limit and the 0.2% flow stress in uniaxial tension for 4340 steel containing 9% retained austenite. The arrow indicates the M_s^σ temperature.

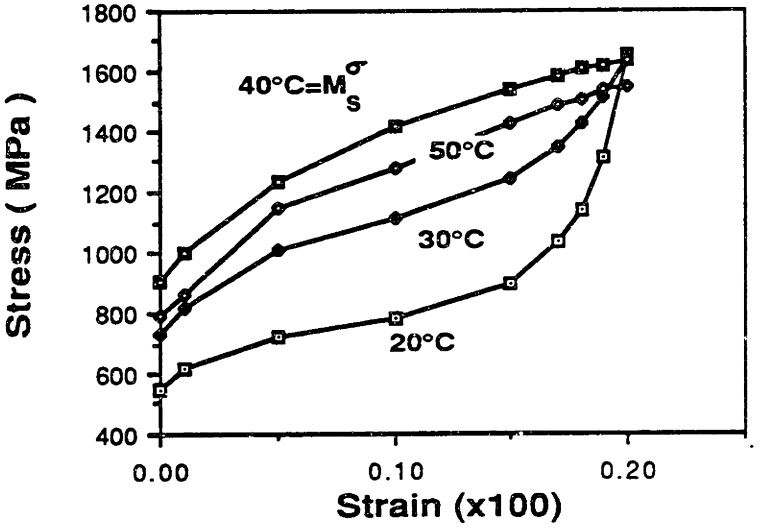

Fig.4.4 Stress-strain curves in the microyielding region for temperatures above and below the tensile M_s^σ temperature. 4340 steel containing 9% retained austenite.

The stress-strain curve at T=20°C is selected to represent the stress-assisted transformation behavior. Two models for the nucleation-site potency distribution are compared. The first model assumes that the transformation is controlled by the pre-existing nucleation sites in the retained austenite. The second model assumes that the transformation is controlled by nucleation sites created due to autocatalysis during the quench from the solution temperature.

4.3.2.1 Exponential Distribution of Pre-Existing Nucleation-Site Potencies.

According to this model the applied elastic stress assists the transformation kinetics by modifying the effective potency distribution of the pre-existing nucleation sites. This distribution has been defined in Chapter 2, eq(2.2). For stress-assisted transformation, yielding is controlled entirely by the transformation, and then f and ε are linearly related:

$$f = \frac{\varepsilon}{\varepsilon_1} \tag{4.1}$$

where ε_1 is the plastic strain at the completion of the stress-assisted transformation (f=1).

Combining equations (2.5),(2.6) and (4.1), we obtain the stress-strain relation in the stress-assisted region:

$$\sigma = \frac{1}{\left(\frac{\partial \Delta G}{\partial \sigma}\right)} \left[\frac{2\alpha\gamma_s/\rho}{\ln\left[-\frac{1}{N_v^o V_p}\ln\left(1-\varepsilon/\varepsilon_1\right)\right]} - \Delta G^{ch} - W_f - E^{str} \right] \tag{4.2}$$

where $(\partial\Delta G/\partial\sigma)$ has the values of $(\partial\Delta G/\partial\sigma)_{max}$ and $1/3(\partial\Delta G/\partial\sigma)_{max}$ for the fully-biased and fully-random distributions of nucleation sites, respectively.

Eq(4.2) can be fitted to the experimental stress-strain curve for T=20°C, with $N_v^0 V_p$ and ΔG^{ch} being the parameters to be determined from the best fit. The strain ε_1

can be determined from a linear extrapolation of the high-temperature elastic limit ($T>M_S^{\sigma}$) to lower temperatures. For T=20°C this extrapolation gives ε_1=0.17%. At this strain the stress would reach the elastic limit of the steel in the absence of transformation (the slip-controlled elastic limit). For $\varepsilon>\varepsilon_1$, plastic yielding by slip introduces new nucleation sites in the retained austenite and the transformation becomes strain-induced. Thus, pure stress-assisted transformation operates up to $\varepsilon=\varepsilon_1$. The frictional work of interfacial motion in eq(4.2) was estimated using the expression given by Kuroda[8]: $W_f=1.310X10^4\ X_C^{2/3}$. For 0.40wt% C in 4340 steel, this gives W_f=1000 J /mol. The remaining parameters in eq(4.2) are E^{str}=500 J/mol, $\rho=3x10^{-5}$ mol/m^2, γ_s=0.15 J/m^2, and α=0.866.

Fig.4.5 compares the experimental stress-strain curve (at T=20°C) with the curve calculated using eq(4.2). Although the calculated σ–ε curve possesses the sigmoidal shape of the experimental σ–ε curve, it does not fit the data well at low and high strains. In particular, the assumption of the exponential nucleation-site potency distribution fails to account for a non-zero value of the elastic limit as well as to predict the onset of rapid work hardening at medium strains. The parameters determined from the best fit are: $N_v^0V_p=1.48x10^4$ and ΔG^{ch}=-1687 J/mol for the fully-biased distribution, and $N_v^0V_p=6.44x10^6$ and ΔG^{ch}=-1811 J/mol for the fully-random distribution. The chemical driving forces calculated in this way, can be compared with the value ΔG^{ch}=-3028 J/mol, estimated from the THERMOCALC database for the composition of 4340 steel at room temperature. The values of ΔG^{ch} determined from the best fit imply a very large discrepancy in ΔG^{ch} which cannot be accounted for by carbon stabilization of the retained austenite. In view of the above considerations, we conclude that the exponential distribution of the pre-existing nucleation sites does not satisfactorily describe the constitutive behavior of the steel in the microyielding region. The next

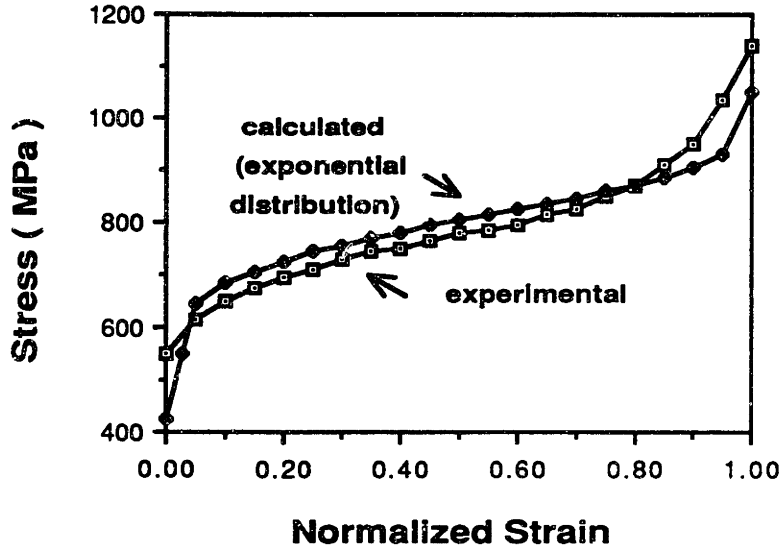

Fig.4.5 Comparison between the experimental stress-strain curve at T=20°C with the model based on the exponential distribution of pre-existing nucleation sites.

section presents a more realistic model, based on the distribution of nucleation sites created due to autocatalysis.

4.3.2.2 Nucleation-Site Potency Distribution of Autocatalytic Sites.

In this model the applied elastic stress assists the transformation kinetics by modifying the effective potency distribution of autocatalytic sites. The following assumptions are employed:

1. The nucleation sites created due to autocatalysis are much more plentiful than the pre-existing sites, i.e. $p f_q >> N_i$, where p is the autocatalytic factor[61], f_q is the fraction transformed during quenching, and N_i is the density of the pre-existing sites. Then, since $f_q \cong 1$, the number of available nucleation sites N_V is:

$$N_V = p$$

2. The potency of the autocatalytic sites follows a Gaussian distribution[62], as shown in Fig.4.6a. A linear approximation is adopted here for the cumulative distribution of nucleation sites (Fig.4.6b):

$$p = C_1 + C_2 n$$

where C_1 and C_2 are constants.

3. Furthermore, the distribution is truncated at $n = n_{RT}$ due to the consumption of sites during quenching and $N_V = \Delta p$ (Fig.4.6c). The potency of the nucleation sites at room temperature n_{RT}, as calculated from eq(2.1) is 6.5.

Under the above set of assumptions, the cumulative distribution of nucleation sites is given by the linear approximation as:

$$N_v(\sigma) = C_2 [\, n(\sigma) - n_{RT}]$$

(4.3)

The potency under an applied stress σ in the present tensile testing is given by:

$$n(\sigma) = - \frac{2\gamma_s / \rho}{\Delta G^{ch,T} + W_{f,T} + E^{str} + \Delta G^{\sigma}}$$

(4.4)

where the chemical driving force $\Delta G^{ch,T}$ and the frictional work of interfacial motion $W_{f,T}$ are now evaluated for the tempered condition and are different from the corresponding ΔG^{ch} and W_f values of eq(2.1) due to carbon enrichment of the retained austenite. Since $\Delta G^{ch,T}$ and $W_{f,T}$ are functions of carbon content, we can write:

$$\Delta G^{ch,T} + W_{f,T} = F(X_c)$$

(4.5)

where $F(X_C)$ is a function of the mole fraction carbon X_C.

Combining eq(2.6) and eq(4.3), the fraction of particles to transform is given by:

$$f = 1 - \exp\left[- C_2 V_P [\, n(\sigma) - n_{RT}]\right]$$

(4.6)

Finally, the stress-strain relation in the microyielding region can be found by combining eqs(4.3),(4.4),(4.5),and (4.6) to obtain:

$$\sigma = \frac{1}{\left(\frac{\partial \Delta G}{\partial \sigma}\right)} \left[\frac{(-2\gamma_s / \rho)(C_2 V_P)}{n_{RT}(C_2 V_P) - \ln(1 - \varepsilon / \varepsilon_1)} - F(X_c) - E^{str} \right]$$

(4.7)

where $(\partial \Delta G/\partial \sigma)$ takes the values of $(\partial \Delta G/\partial \sigma)_{max}$ and 1/3 $(\partial \Delta G/\partial \sigma)_{max}$ for the fully-biased and fully-random distributions of nucleation sites respectively.
Eq(4.7) will be fitted to the experimental stress-strain curve for T=20°C, with $F(X_C)$ and C_2V_p being the parameters to be determined from the best fit.

Fig.4.7 compares the experimental stress-strain curve (at T=20°C) with the curve calculated from eq(4.7). Although the model predicts a higher elastic limit, it agrees very well at higher plastic strains, especially in the rapid work-hardening regime. The rapid increase in the rate of work hardening is suggestive of the exhaustion of available nucleation sites at strains close to ε_1. This, however, does not necessarily imply complete transformation of the retained austenite, since a single nucleation event is generally not expected to give rise to complete transformation of film-like austenite particles. Complete transformation would require more than one nucleation event per particle, the probability of which is negligible. It is estimated that at T=20°C only approximately 30% of retained austenite transforms up to $\varepsilon=\varepsilon_1$, while the fraction of austenite particles containing martensite is approaching unity.

Using non-linear curve-fitting, the values of the parameters for the best fit are: C_2V_p = -2.614 and $F(X_C) = \Delta G^{ch,T} + W_{f,T}$ = -1455 J / mol for the fully-biased distribution model, and C_2V_p=-6.871 and F(Xc) = -1845 J / mol for the fully-random distribution model.

From the calculated value of $F(X_C)$, the extent of carbon enrichment of the retained austenite due to tempering can now be estimated. From eq(4.5) and using THERMOCALC to express the chemical driving force as a function of carbon $\Delta G^{ch}=\Delta G^{ch}(X_C)$, we find that X_C=0.026 or 0.57wt% C for the fully-biased distribution model and X_C=0.022 or 0.46wt% for the fully-random distribution model. This is the carbon content of the retained austenite after tempering. Similar levels of carbon enrichment of the retained austenite have been observed by Barnard et al.[63] in a 0.26C, 2Cr, 1.98Mn, 0.5Mo, 0.01Ni steel by means of atom probe/field-ion microscopy.

The slope $\partial\sigma/\partial T$ in the stress-assisted transformation regime can now be calculated and compared with the experimental slope of 15.2 MPa/K for the temperature dependence of the elastic limit from Fig.4.3. The slope $\partial\sigma/\partial T$ is related to the entropy change $\Delta S^{\gamma\alpha}$ for the martensitic transformation through the relation:

$$\frac{\partial \sigma}{\partial T} = - \frac{\Delta S^{\gamma\alpha}}{(\partial \Delta G / \partial \sigma)}$$

$\Delta S^{\gamma\alpha}$ was evaluated at room temperature for the carbon content estimated above. For the two limits we have $\Delta S(0.57wt\%C)=4.609$ J/mol.K and $\Delta S(0.46wt\%C)=4.755$ J/mol.K. This gives $\partial\sigma/\partial T=5.3$ MPa/K for the fully-biased distribution and $\partial\sigma/\partial T=16.5$ MPa/K for the fully-random distribution. The actual behavior is therefore bracketed by these two limits but is closer to the fully-random distribution of nucleation sites.

The parameter C_2 in the model corresponds to the slope dp/dn of the autocatalytic-site potency distribution. Using $V_p=3x10^{-14}m^3$ from TEM observations of retained austenite by Rao and Thomas[64] and the result $C_2V_p=-6.871$ from above, we get $C_2=2.3x10^{14}/m^3$ which is in very good agreement with the value dp/dn= $8x10^{13}/m^3$ obtained by Lin[62] for a Fe-29.5 Ni alloy.

The reduction of the driving force due to the carbon enrichment is $d(\Delta G)=(\Delta G^{ch}+W_f) - F(X_C) = 183$ J/mol. The stress required to compensate for the decrease in the chemical driving force can be calculated from the condition:

$$\sigma \left(\frac{\partial \Delta G}{\partial \sigma} \right) = d (\Delta G)$$

and is $\sigma=641$ MPa. This transformation stress is also the elastic limit of the tempered steel in the stress-assisted transformation regime.

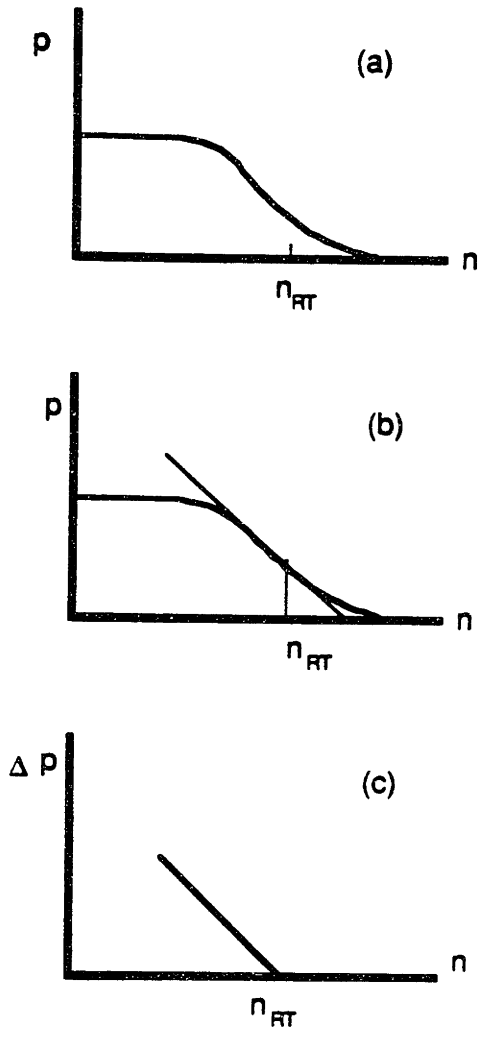

Fig.4.6 Potency distribution of autocatalytic sites. p is the autocatalytic factor, n is the structural potency of nucleation sites, and n_{RT} is the potency of nucleation sites at room temperature, immediately after the steel is quenched from the solution temperature to room temperature. The Gaussian distribution of autocatalytic sites is shown in (a), the linearization in (b) and the truncation of the distribution at n_{RT} due to the consumption of sites during quenching in (c).

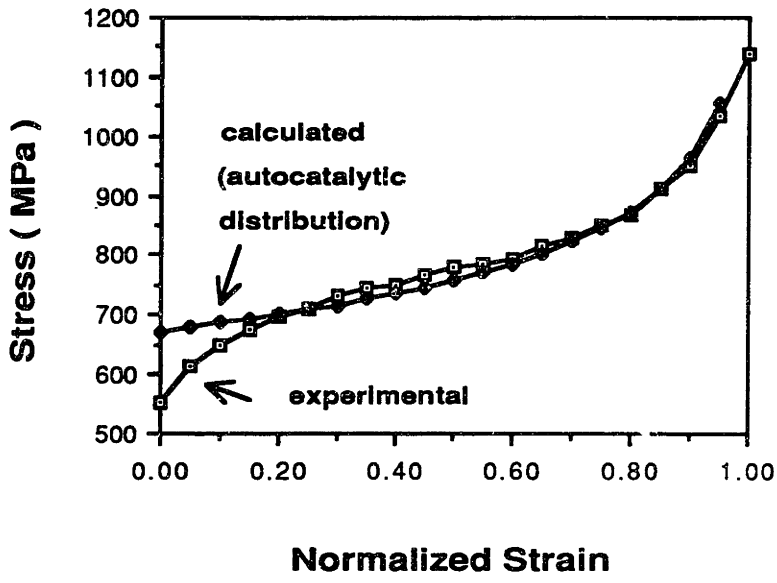

Fig.4.7 Comparison of experimental stress-strain curve at T=20°C with the model based on the distribution of autocatalytic sites .

4.4 Stress-state Dependence of M_S^σ Temperature.

Table 4.2 shows the experimentally determined M_S^σ temperatures for tension and compression. Two more entries are shown in the same table corresponding to the M_S^σ temperatures for the pure shear and crack-tip stress states, M_S^σ(p.s) and M_S^σ(c) respectively. The M_S^σ(p.s) was taken to be $1/2[M_S^\sigma(u.t)+M_S^\sigma(u.c)]$ assuming a linear relationship between M_S^σ and stress state. The M_S^σ(c) was estimated from a simple extrapolation to the crack-tip stress state. Table 4.2 gives a relatively complete picture of the stress-state dependence of the M_S^σ temperature underlying the varying degree of stability of the retained austenite with stress state. It is interesting to note that the M_S^σ temperature varies with the austenitizing temperature, indicating that a lower austenitizing temperature results in retained austenite of a higher stability.

Two points regarding the stability of the retained austenite have to be made. First, The carbon enrichment of the retained austenite, that was estimated in the previous section by modelling the constitutive behavior in the microyielding regime, is not enough to stabilize the retained austenite for crack-tip interactions that could lead to transformation toughening. The second point regards the assumption that stabilization was due to carbon enrichment. Another phenomenon that contributes to stabilization is the distortion of the retained austenite/lath martensite interfaces after the transformation on cooling. However, this type of stabilization is extremely difficult to quantify both analytically and experimentally and was not considered in this work.

Table 4.2 M_s^{σ} Temperatures for Retained Austenite in 4340 Steel.

Austenitizing Temperature	Volume fraction Ret. Austenite	Tension M_s^{σ}(u.t)	Compression M_s^{σ}(u.c)	Pure Shear M_s^{σ}(p.s)	Crack-tip M_s^{σ}(c)
1200°C	0.09	45 ± 5°C[1] 47 ± 27°C[2]	-25 ± 5°C[1] -37 ± 17°C[2]	7.5°C[3]	> 150°C[3]
870°C	0.04	15 ± 5°C[1]	< -50°C[1]	< -17°C[3]	> 150°C[3]

1. Determined from onset of plateau region and yield-point phenomena
2. Determined from local minima in the S-D effect
3. Estimated values

4.5 Plastic Flow Stabilization In Pure Shear

One of the most important effects of transformation plasticity is the stabilization of plastic flow. In pure shear deformation, the strain-induced transformation of the retained austenite can delay shear localization to higher strains. These effects were investigated with controlled experiments where the amount of retained austenite was varied using the high-magnetic-field cryogenic treatments described in Table 4.1. Thin-wall torsion testing was performed for the four conditions listed in Table 4.1. The tests were run at room temperature, i.e. above the estimated M_s^{σ}(p.s) shown in Table 4.2 to ensure a high stability of retained austenite against stress-assisted transformation. The shear stress-strain curves to the point of instability are shown in Fig.4.8a and Fig.4.8b for the 870°C and 1200°C austenitizing temperatures respectively. A delay in shear instability is associated with the higher amounts of retained austenite. The increase in shear instability strain is of the order of 25 to 30%. It should be emphasized that the amount of retained austenite is the only variable in these experiments. The specimens have otherwise received identical heat treatments resulting in identical hardness.* The retained austenite content as a function of shear strain was determined by saturation magnetization measurements after interrupted straining of identically treated specimens. The results are shown in Fig.4.8c and Fig.4.8d for the 870°C and 1200°C austenitizing temperatures respectively, indicating that the retained austenite transforms during the test. The curves also indicate a complete exhaustion of the transformation at the point of shear instability.

---

* Any additional mobile dislocations introduced by the magnetically-induced martensitic transformation are fully "aged" after tempering to 200°C for 1h.

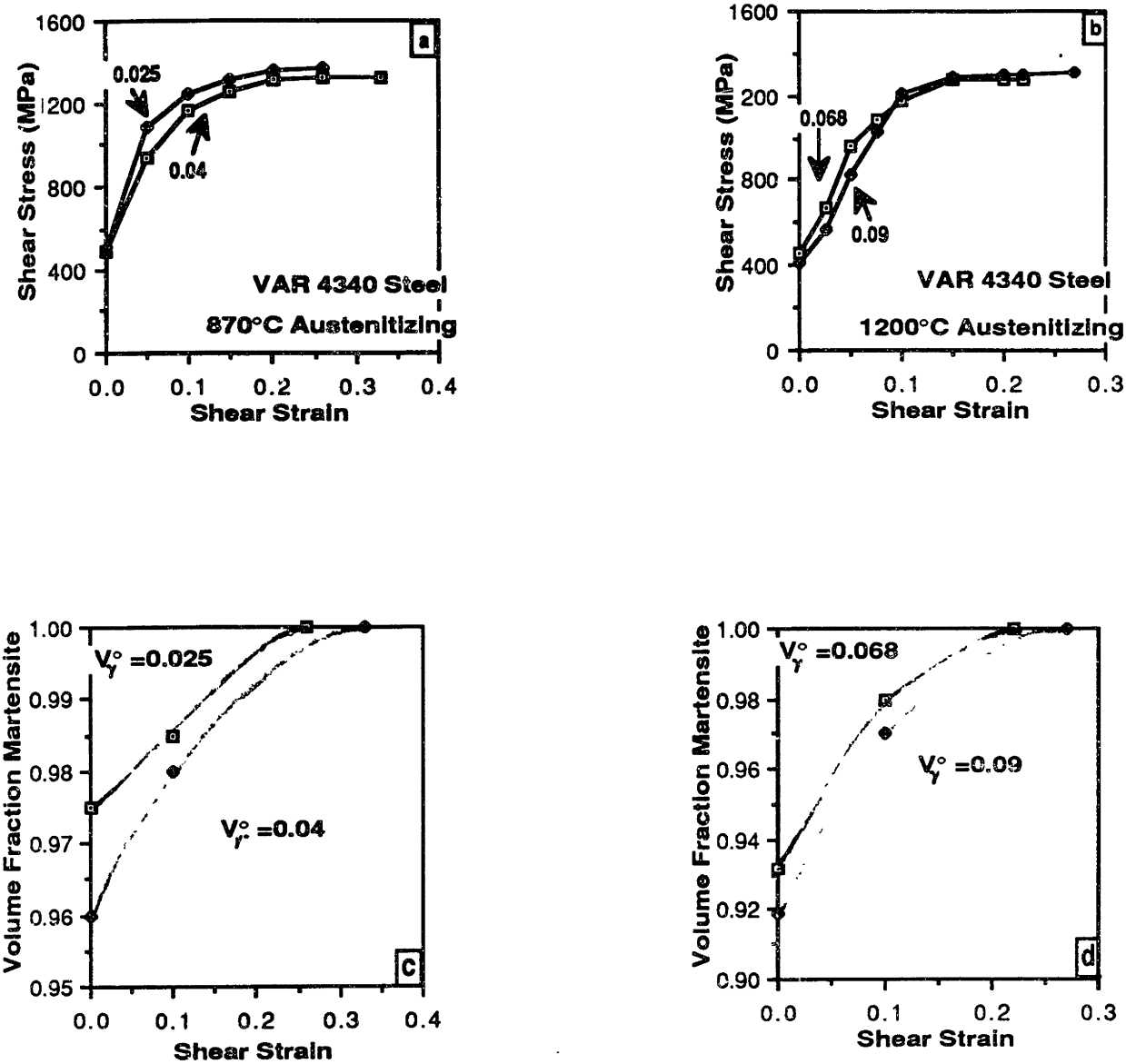

Fig.4.8 Stress-strain curves (a,b) and corresponding martensite volume fraction as a function of plastic strain (c,d) during pure-shear deformation of 4340 steel. (a),(c) are for the 870°C austenitizing temperature while (b),(d) are for the 1200°C austenitizing temperature. Isothermal thin-wall torsion test.

4.6 Implications On Toughening

It was demonstrated in the previous section that the strain-induced transformation of the retained austenite delayed shear instability during pure shear deformation. Since fracture in these steels is often controlled by shear localization, it is expected that such delocalizing effects arising from the transformation plasticity of the retained austenite should enhance the fracture toughness. However, the stability of the retained austenite for the crack-tip stress-state is very low, as indicated by the high $M_S^{\sigma}(c)$ temperature in Table 4.2. A toughening effect associated with the strain-induced transformation of the retained austenite would only be observed above the $M_S^{\sigma}(c)$ temperature, i.e., above 150°C. This temperature is too close to the tempering temperature (200°C) for K_{IC} testing of a stable material to be performed.# Therefore, the toughening role of retained austenite cannot be assessed directly. To confirm this point, K_{IC} testing was performed at room temperature, and as expected, no correlation was found between retained austenite and fracture toughness beyond experimental scatter. The K_{IC} results, together with the shear instability strains determined from the thin-wall torsion tests, are given along with the corresponding M_S^{σ} temperatures in Table 4.3. It is apparent from this table that the retained austenite is sufficiently stable for the pure-shear stress state but unstable for the crack-tip stress state when testing is performed at room temperature. Transformation toughening can result only by lowering the $M_S^{\sigma}(c)$

Fatigue precracking would have to be performed at an even higher temperature (above Md).

below room temperature by stabilizing the austenite. It will be shown that this can be achieved in reformed or precipitated austenite which can then be stabilized by size refinement and compositional enrichment, using multistep heat treatments.

Table 4.3 Shear Instability Strains and KIC Fracture Toughness for 4340 Steel.

Austen.Temp.	Vol.Fraction Retained Aust.	Shear M_s^{σ}(p.s)	Shear Instability Strain	Crack-tip M_s^{σ}(c)	K_{IC} (Ksi.in$^{1/2}$)
870°C	0.04	<-17°C **	0.34	> 150°C **	48.4 (+1.5,-1.0)
870°C	0.025	-	0.27	-	47.1 (+1.8,-2.1)
1200°C	0.09	7.5°C**	0.28	> 150°C **	84.5 *
1200°C	0.068	-	0.22	-	84.4 (+13.8,-10.)

* The reported value is K_Q

** Estimated values

5. PRECIPITATED AUSTENITE

5.1 Introduction

"Precipitated"* austenite is the form of dispersed austenite that precipitates on high-temperature tempering or intercritical annealing. It is different from retained austenite which is the parent phase that remains untransformed after quenching from the solution temperature. This fundamental difference in the mode of formation makes the precipitated austenite attractive for the study of transformation toughening. Since it is formed through a precipitation reaction rather than being the leftover of a martensitic transformation, its amount and distribution can be controlled. Its size and composition can be varied through heat treatment and its stability can be tuned for transformation-toughening effects.

The focus of this chapter is on austenite stabilization and toughening. First, the parameters that affect austenite stability are identified and a functional form relating austenite stability with these parameters is constructed. For this purpose the M_s^{σ} temperature is used as a single-parameter characterization of the austenite stability.

Thermodynamic calculations, using the Thermocalc software and database, deal with the compositional effects on austenite stability. Alloy design criteria for transformation toughening are then presented based on

---

* The terms "reverted" or "reformed" austenite have also been used in the literature to describe precipitated austenite. Since the austenite under consideration in this work forms through a precipitation reaction rather than a reverse martensitic transformation it is refered here as "precipitated".

thermodynamics.

In the experimental part, austenite precipitation is studied in the high Ni-Co steels. Single tempering treatments are compared with multi-step treatments regarding austenite stability. Finally, fracture toughness results for various treatments are presented and correlated with austenite stabilization.

5.2 Austenite Stabilization

5.2.1 Parameters Affecting Austenite Stability. M_s^σ Temperature.

The stability of dispersed austenite is the most important parameter controlling its tranformation plasticity and toughening effects. The stability depends on the following factors:

1) chemical composition of the austenite particles (affects the chemical driving force for the martensitic transformation)

2) austenite particle size (affects the probability of finding nucleation sites in the particle)

3) stress state (due to the interaction of the transformational volume change with stress triaxiality)

4) strength of the matrix (affects the mechanical driving force contribution to the total driving force for the martensitic transformation)

It was discussed earlier that the M_s^σ temperature provides a single-parameter characterization of the stability of the dispersed austenite. The M_s^σ temperature depends on the size and composition of the austenite particles, the yield strength of the matrix, and the stress state:

$$M_s^{\sigma} = M_s^{\sigma}\left(\sigma_y, \frac{\sigma_h}{\bar{\sigma}}, V_p, \text{wt\% Ni}\right) \tag{5.1}$$

where σ_y is the yield strength, σ_h is the hydrostatic stress, σ is the effective stress, and V_p is the average austenite particle size.

The maximum toughening occurs when the M_s^{σ} temperature for the crack-tip stress state is just below room temperature. The required microstructure can then be prescribed by model predictions of the M_s^{σ} temperature for the 14Co-10Ni steels of interest to this work. A functional form will be developed for the M_s^{σ} temperature in eq (5.1) that will enable the prediction of required particle size and Ni enrichment to set $M_s^{\sigma}(c)$=300K.

For a dispersion of metastable particles in a stable matrix, the stress-assisted transformation is controlled by the pre-existing nucleation sites. The stress-modified cumulative distribution of nucleation sites was introduced in Chapter 2, and has the exponential form :

$$N_v = N_v^o \exp\left(-\alpha n\right) \tag{5.2}$$

where n is the structural potency given by:

$$n = -\frac{2\gamma_s / \rho}{\Delta G^{ch} + \Delta G^{\sigma} + W_f + E^{str}} \tag{5.3}$$

where ρ is the density of atoms in a closed-packed plane and all other parameters appearing in eq(5.2) and (5.3) have been previously defined in Chapter 2. For particles of average volume V_p, the probability of finding at least one nucleation site in the particle is given by:

$$f = 1 - \exp\left(-N_v V_p\right) \tag{5.4}$$

Assuming that a single nucleation event transforms the particle, then, for a large number of particles, the fraction of particles to transform will be given by the probability defined above.

Taking the Patel-Cohen criterion for the mechanical driving force:

$$\Delta G^{\sigma} = \sigma \left(\frac{\partial \Delta G}{\partial \bar{\sigma}}\right)_{max} \tag{5.5}$$

the transformation stress can be found by combinig eq(5.2), (5.3), (5.4) and (5.5):

$$\sigma_t = \frac{1}{\left(\frac{\partial \Delta G}{\partial \bar{\sigma}}\right)} \left[\frac{2 \alpha \gamma_s / \rho}{\ln \left[- \frac{\ln (1-f)}{N_v^o V_P} \right]} - \Delta G^{ch} - W_f - E^{str} \right] \tag{5.6}$$

The chemical driving force can be expressed as a function of temperature and wt% Ni using the Thermocalc database. For the Fe-14Co system a linear expression was obtained as follows:

$$\Delta G^{ch} = -8885.82 + 200.48 \, (\, wt\%Ni \,) + 5.91 \, T \tag{5.7}$$

The frictional work of interfacial motion W_f was calculated as a function of Ni content from the composition dependence of the critical driving force ΔG_{crit} at M_S for Fe-Ni alloys[65]:

$$W_f = 2.93 \, (\, wt\% \, Ni \,)^{2/3} \tag{5.8}$$

The parameter $(\partial \Delta G / \partial \sigma)$ is given as a function of stress state by Olson and Cohen [60] as follows:

For compression -0.58 J/mol MPa, for tension -0.86 J/mol MPa and for the crack-tip -1.42 J/mol MPa. These data are shown in Fig.5.1 where the stress-state is represented by the parameter σ_h/σ. A straight line fit of the data gives:

$$\frac{\partial \Delta G}{\partial \bar{\sigma}} = -0.715 - 0.3206 \left(\frac{\sigma_h}{\bar{\sigma}} \right) \tag{5.9}$$

At the M_s^σ temperature, the transformation stress equals the yield stress. Setting $\sigma_t \simeq \sigma_y$ and substituting eq(5.7), (5.8), and(5.9) into eq(5.6), the M_s^σ temperature can be obtained as follows:

$$M_s^\sigma = \sigma_y \left[0.121 + 0.0542 \left(\sigma_h / \bar{\sigma} \right) \right] + \frac{1465.3}{- 4.6 - \ln N_v^o \, V_P} + \left[1418.92 - 33.92 \left(\text{wt\% NI} \right) - 0.5 \left(\text{wt\% Ni} \right)^{2/3} \right] \tag{5.10}$$

This equation shows the effects of yield strength, stress state, austenite particle size, and Ni enrichment on the stability of the dispersed austenite as it is expressed by the M_s^σ temperature. It indicates that in order to get very high stability of the dispersed austenite, so that the M_s^σ temperature for the crack-tip stress state can be as low as room temperature, the austenite has to be very fine (small V_p) and enriched in Ni. The relationship between particle size and compositional enrichment can now be explored with the aid of eq(5.10). Setting $M_s^\sigma(c)$=300K for the crack-tip stress state, and taking σ_y =1400 MPa for AF1410 steel, the resulting relationship is indicated in Fig.5.2 which shows the Ni content of the austenite particles vs their size. The size here is represented by a scaled radius $(N_V^o Vp)^{1/3}$. The figure indicates that the destabilizing effect of increasing the austenite particle size should be compensated by a corresponding increase in Ni enrichment to keep the degree of stability constant. The parameter N_V^o represents the total number of nucleation sites of

all potencies and was introduced in chapter 2. Its magnitude is not known for dispersed systems; however, the value $2x10^{17}m^{-3}$ has been obtained for Fe-Ni polycrystals[66]. Experimental results on the size and composition of austenite particles can be used to estimate the value of N_V^O for the dispersed austenite. This issue will be addressed later in this chapter.

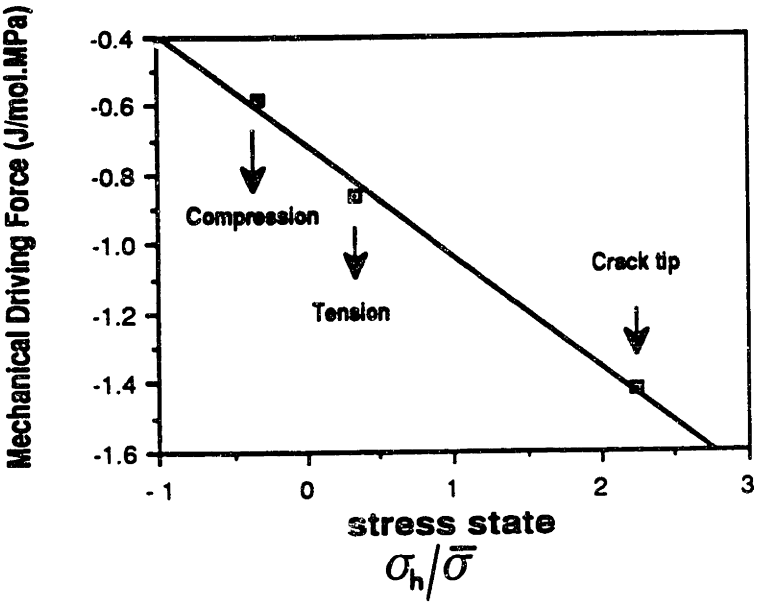

Fig.5.1 Stress-state dependence of the mechanical driving force for deformation-induced transformation. The data points are from Olson and Cohen[59]. The solid line indicates a linear fit of the data.

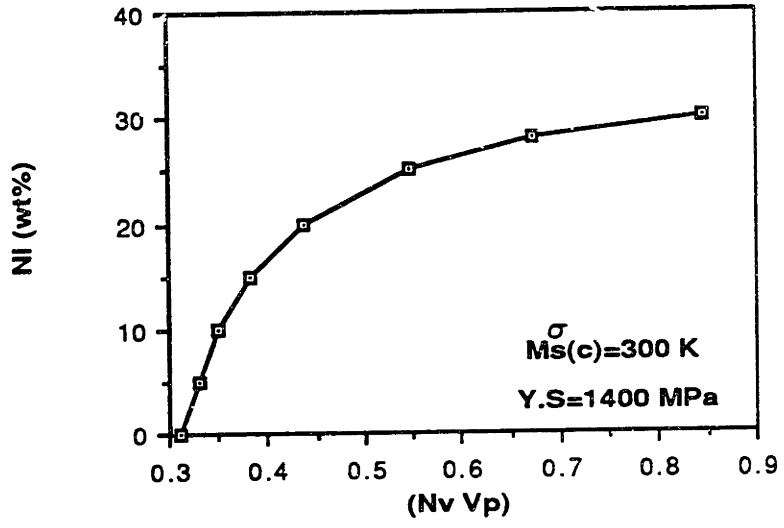

Fig.5.2 Normalized austenite particle volume vs Ni content in the Fe-14Co-Ni system, for a yield strength of 1400 MPa and crack-tip M_s^{σ}(c)=300 K.

5.2.2.2 Thermodynamic Calculations

This section presents thermodynamic calculations regarding the compositional effects on austenite stability. The calculations were performed with the Thermocalc software. Fig.5.3 and 5.4 show two isothermal sections of the ternary Fe-Ni-Co system at 510°c and 600°C respectively. The $\alpha+\gamma / \gamma$ phase boundary shifts to the left as the temperature is raised from 510 to 600°C. This causes the Ni content of the austenite in equilibrium with ferrite to decrease. Therefore, the austenite has lower stability at higher temperatures.

The intersection of the tie-lines with the $\alpha+\gamma / \gamma$ two-phase boundary in Fig.5.4 define the austenite compositions in equilibrium with ferrite at a given temperature. The locus of these intersection points as a function of temperature for the Fe-14Co-10Ni system is shown in Fig.5.5. As the tempering temperature decreases, the austenite is enriched in Ni and depleted in Co. Fig.5.6 shows the amount of austenite (mole fraction) as a function of tempering temperature, indicating that at the tempering temperatures of interest (500-600°C), about 20% austenite can form at equilibrium.

Specific calculations were performed for the 6-component AF1410 steel. Table 5.1 gives the compositions and volume fractions of the equilibrium austenite at 510 and 600°C, while Table 5.2 gives the compositions and volume fractions of the other phases in equilibrium with austenite at the same temperatures. The austenite is more enriched in Ni at 510°C than at 600°C. but has a lower volume fraction at 510°C.

Since the material is designed for transformation toughening at room temperature, a quantitative characterization of austenite stability that can also be used for alloy design can be provided by the free-energy change for martensitic transformation evaluated at room temperature. This quantity $\Delta G^{ch}(RT)$ was calculated for the Fe-Ni-Co system. The martensitic phase was

represented by the BCC phase with the same composition as FCC since the transformation is diffusionless. Fig.5.7 shows the contours of the free energies of FCC and BCC as a function of composition, evaluated at 300K. The difference between these free energies is the free-energy change for the martensitic transformation $\Delta G^{ch} = G^{bcc}-G^{fcc}$. The more positive this quantity, the more stable the austenite. Fig.5.8 shows contours of ΔGch as a function of composition for the ternary Fe-Ni-Co system. Superimposed on the same plot is the isothermal section of Fe-Ni-Co at 510°C (dotted lines) with two tie-lines shown. This combined plot allows one to select alloy compositions for austenite stabilization. Starting with an alloy composition Xo, the corresponding tie-line defines the composition of the austenite Xγ that precipitates at 510°C. That composition then defines, from the ΔG^{ch} contour plot, the chemical driving force at room temperature. Therefore, alloy compositions that maximize austenite stability can be selected. Table 5.3 lists alloy compositions with the corresponding values of ΔG^{ch}(RT) and volume fraction of austenite that precipitates at 510°C.

Table 5.1 Equilibrium Austenite in AF1410 steel.

COMPOSITIONS (WT%)

ELEMENT	TEMPERATURE 510°C	600°C
Ni	38.50	27.60
Co	4.10	6.79
C	5.4x10-4	8.5x10-3
Cr	0.98	1.33
Mo	0.23	0.27
Fe	Balance	Balance
VOLUME FRACTIONS	0.167	0.240

Table 5.2 Compositions and volume fractions of phases in equilibrium with austenite at 510 and 600°C in AF1410 steel.

	BCC	$M_{23}C_6$	M_2C	M_6C
Volume Fraction	**0.803** 0.730	**0.025** 0.0244	**0.0042** 0.00467	**2.1E-4** -
Ni	**4.45** 4.61	**-** -	**-** -	**-** -
Co	**16.58** 16.92	**-** -	**-** -	**-** -
Cr	**0.51** 0.70	**52.20** 42.62	**19.71** 26.71	**5.26** 7.36
Mo	**0.14** 0.19	**20.21** 19.89	**73.37** 65.87	**68.51** 64.46
C	**8E-5** 1.23E-3	**5.06** 5.03	**6.87** 7.22	**2.48** 2.54

* Compositions are in wt%
*Boldface numbers are for 510°C. The plain numbers are for 600°C.

Table 5.3 Alloy Compositions and corresponding stabilities and volume fractions of equilibrium austenite at 510°C.

Alloy	ΔG_{ch}	**Mole Fraction Austenite**
Fe-14Co-10Ni	1.1 KJ/mol	0.177
Fe-14Co-15Ni	1.2	0.300
Fe-18Co-10Ni	1.4	0.172
Fe-18Co-15Ni	1.6	0.291

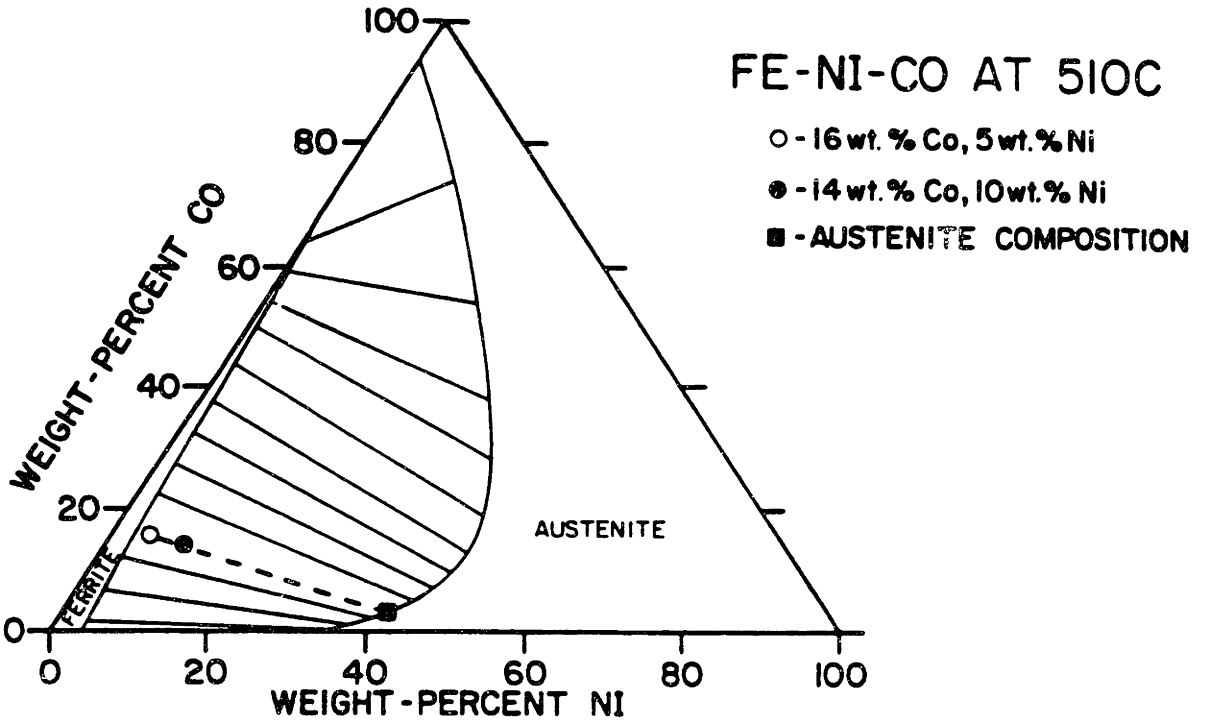

Fig.5.3 Ternary section of the Fe - Ni - Co system at 510°C computed with the Thermocalc software. The solid round point indicates the 14Co-10Ni composition.

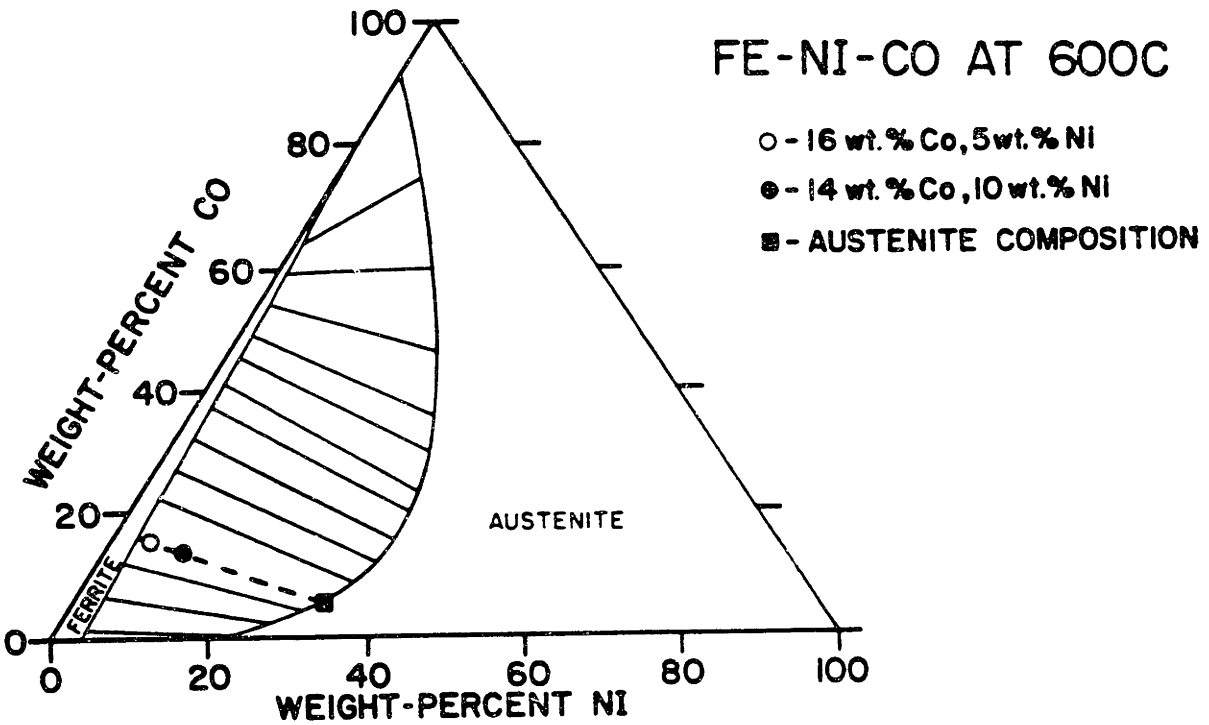

Fig.5.4 Ternary section of the Fe - Ni - Co system at 600°C computed with the Thermocalc software. The solid round point indicates the 14Co-10Ni composition.

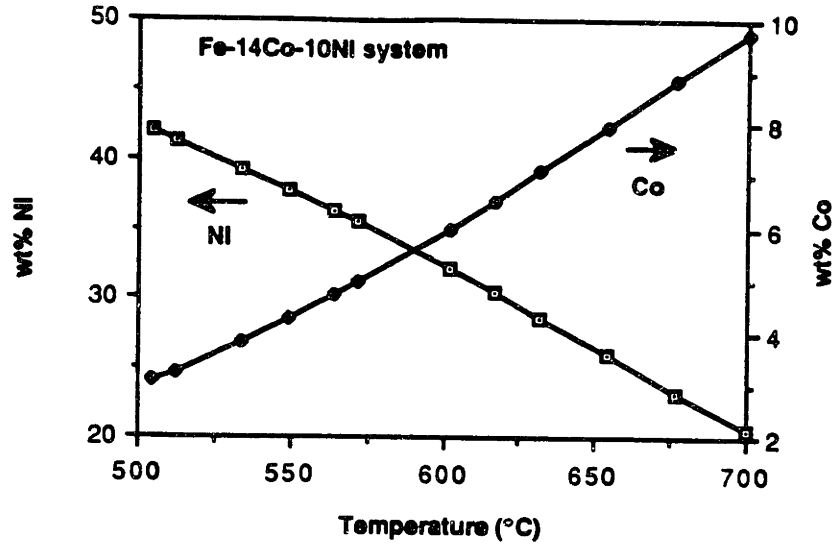

Fig.5.5 Composition of the austenite (in wt% Ni and Co) in equilibrium with ferrite as a function of tempering temperature in the Fe-14Co-10Ni system. The calculations were performed using the Thermocalc software and represent the locus of the tie-lines for the austenite composition in the ternary sections shown in Fig.5.4.

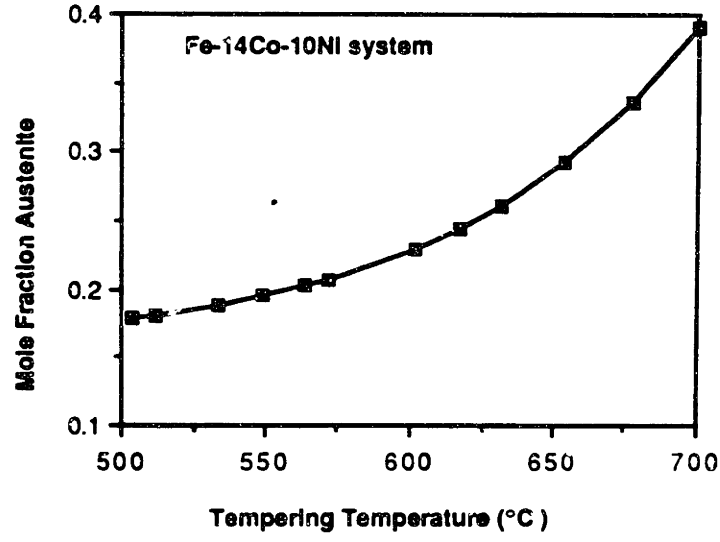

Fig.5.6 Mole fraction of austenite as a function of tempering temperature in the Fe-14Co-10Ni system. The austenite is in equilibrium with ferrite. The calculations were performed using the Thermocalc software.

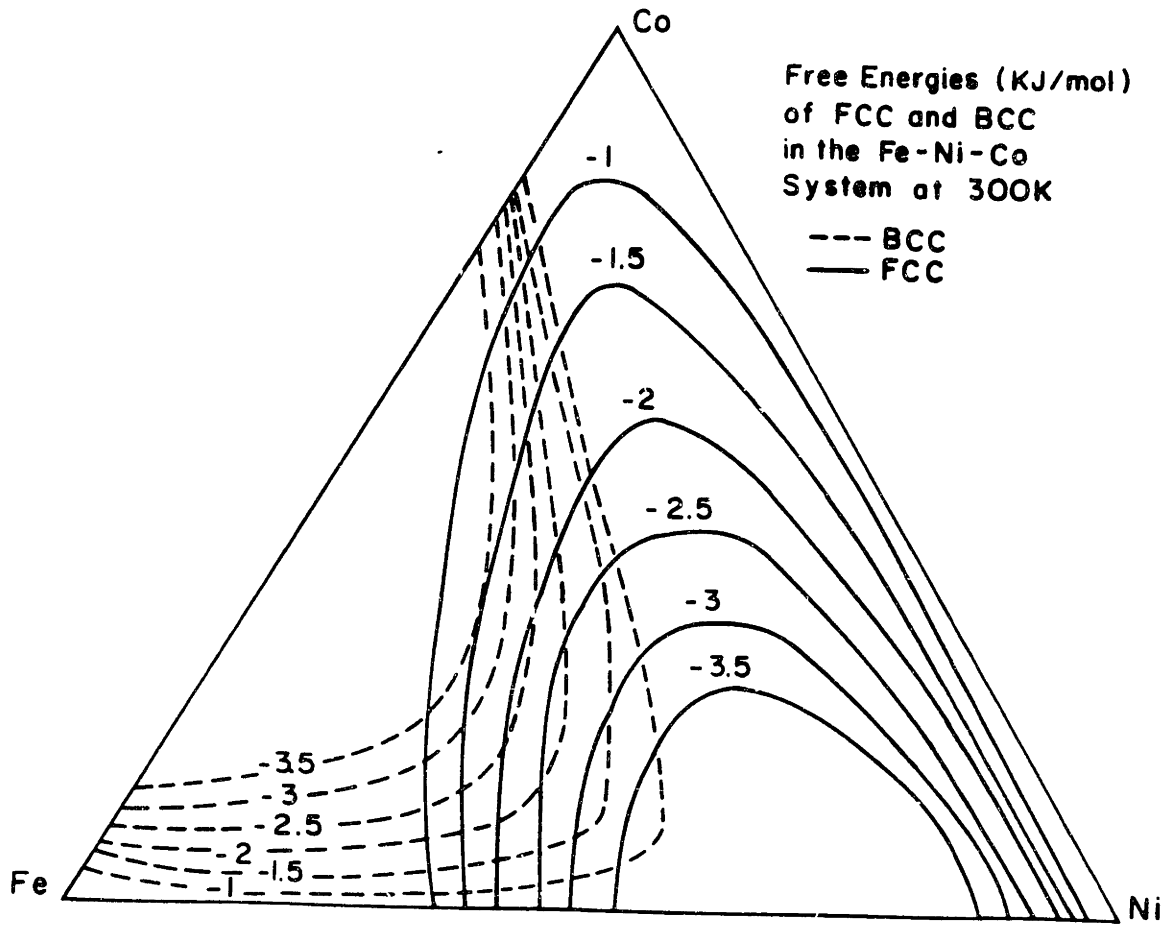

Fig.5.7 Free energy contours (in KJ/mol) of the FCC and BCC phases in the Fe-Ni-Co system at 300K.

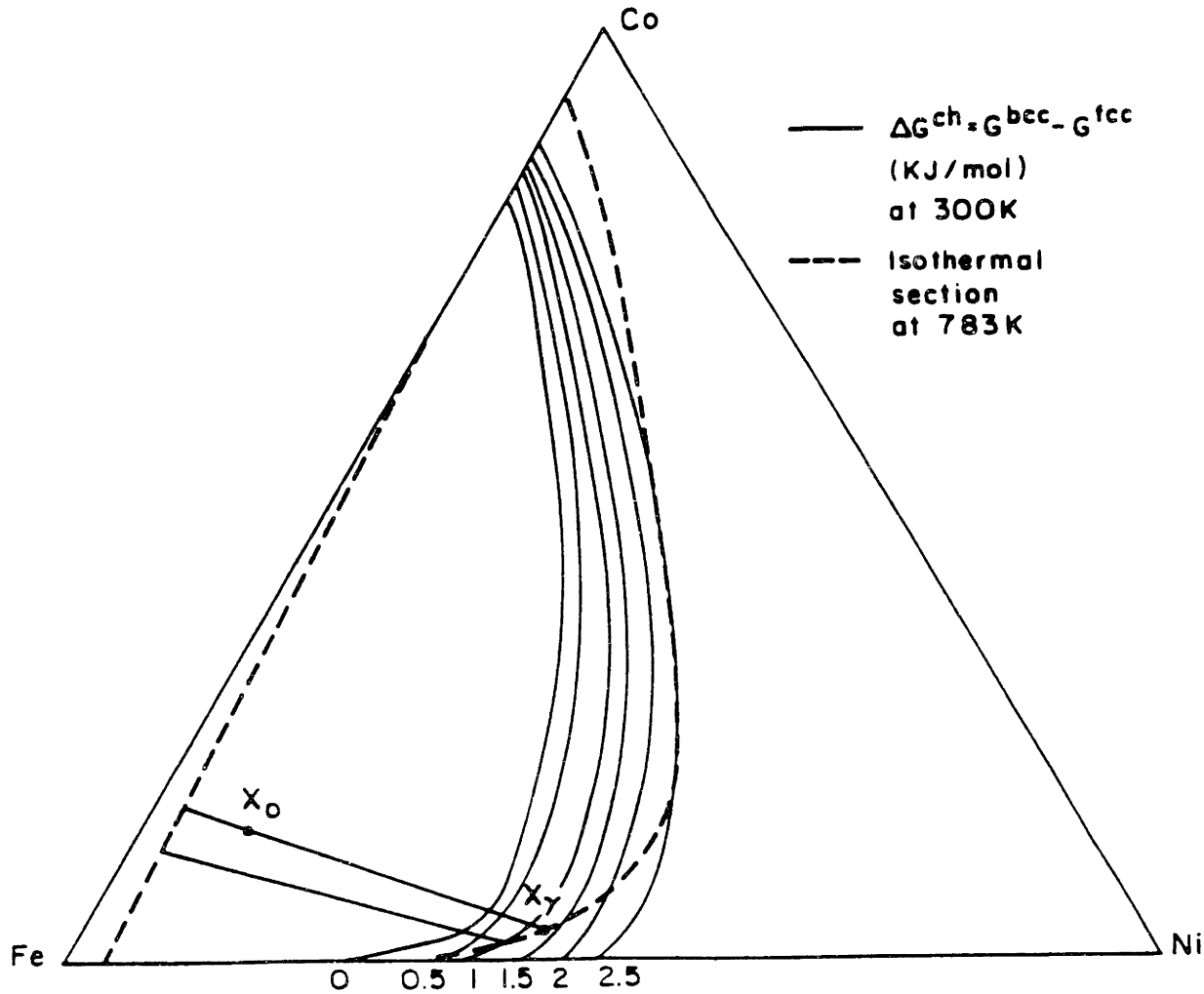

Fig.5.8 Contours of the free energy change (in KJ/mol) for the martensitic transformation at 300K (solid lines) and superimposed isothermal section (dotted lines) at 783K of the Fe-Ni-Co system. Xo represents the alloy composition and $X\gamma$ the austenite composition.

5.3 Single Tempering Treatments

1410-4Mo Steels.

The computer-designed 1410-4Mo composition is based on the commercially available AF1410 steel. Thermocalc calculations were directed at finding coarsening-resistant M_2C carbide compositions. The results indicated that although an optimum M_2C carbide free energy of formation favors significant Cr content, minimization of solubility (taking into account activities in the Fe-Ni-Co matrix) favors almost pure Mo_2C. Accordingly a complete substitution of Cr with Mo was made and the carbon level was increased for a balanced composition with respect to the M_2C stoichiometry. The composition of the steel is shown in Table 3.1. A low-carbon version 1410-4Mo(L) was also prepared.

The tempering response of 1410-4Mo is shown in Fig.5.9. The figure indicates that 1410-4Mo belongs to the class of secondary-hardening steels, where high strength is obtained through precipitation of alloy M_2C carbides during tempering at relatively high temperatures (500-600°C). As Fig.5.9 shows, the hardness initially drops relative to the as-quenched condition due to cementite precipitation. The coarse cementite is then replaced by a very fine Mo_2C carbide dispersion, resulting in a secondary-hardening peak. The hardness drops at longer tempering times due to carbide coarsening.

Austenite precipitation during tempering was monitored by measuring the changes in resistivity and saturation magnetization of heat-treated specimens relative to the as-quenched condition. Fig.5.10 shows the changes in relative resistivity with tempering time for the 1410-4Mo tempered at 500°C. The upper curve in Fig.5.10 indicates the relative resistivity at 500°C. After an initial drop of the resistivity due to recovery processes and carbide precipitation, the resistivity rises due to austenite precipitation. The resistivity continues to

increase with time as more austenite precipitates at 500°C. The intermediate curve in Fig.5.10 shows the resistivity changes that occur after the specimens have been tempered and then cooled to room temperature (25°C). After an initial drop of the resistivity as before, a local maximum is observed at 8h of tempering time. This is because the austenite that forms as a result of 8h of tempering at 500°C is unstable and transforms to martensite when cooled to room temperature, thus decreasing the resistivity. The bottom curve represents the resistivity changes with tempering time for specimens tempered at 500°C and then cooled to liquid nitrogen temperature. The behavior is similar with that of the previous curve, but the peak height at 8h has decreased in magnitude indicating further transformation of the precipitated austenite upon cooling to -196°C. This experiment demonstrates that on simple tempering relatively stable austenite precipitates between 5 and 8h, but since this austenite transforms on cooling to -196°C it is not stable enough for transformation toughening effects, where higher stability is required.

The austenite precipitation in 1410-4Mo was also monitored with saturation magnetization measurements. Fig.5.11 shows the relative resistivity and magnetization changes with tempering time for specimens tempered at 500°C and then cooled to room temperature. Due to the paramagnetic nature of the austenite, the saturation magnetization decreases when austenite precipitates. The minimum in the saturation magnetization curve corresponds to stable austenite precipitation and occurs at 8h consistent with the increase in resistivity.

Saturation magnetization measurements on the 1410-4Mo and 1410-4Mo(L) were also performed as a function of tempering temperature for 5h of tempering time. The results are shown in Fig.5.12 which indicates that higher carbon causes the austenite to precipitate at lower tempering temperatures.

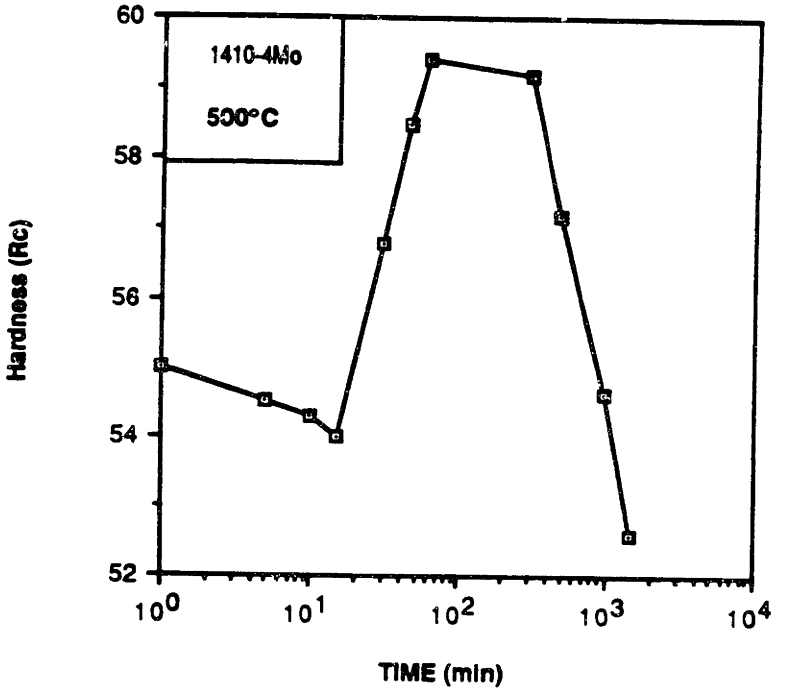

Fig.5.9 Tempering response (hardness vs tempering time) of 1410-4Mo steel at 500°C.

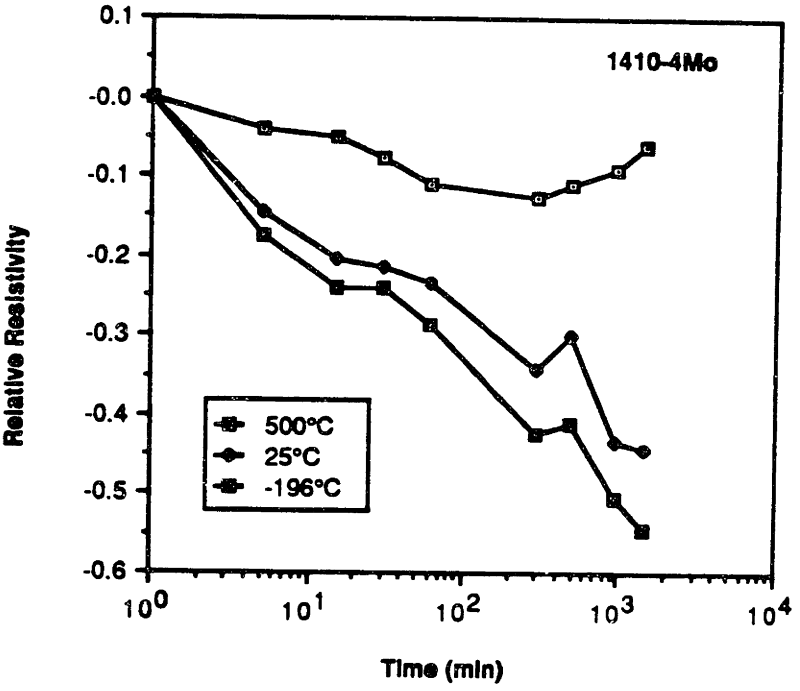

Fig.5.10 Relative resistivity as a function of tempering time for 1410-4Mo tempered at 500°C. The upper curve represents measurements performed at temperature (500°C), the middle curve represents measurements performed after the specimens were cooled to room temperature, and the lower curve corresponds to measurements performed after the specimens were further cooled to liquid nitrogen.

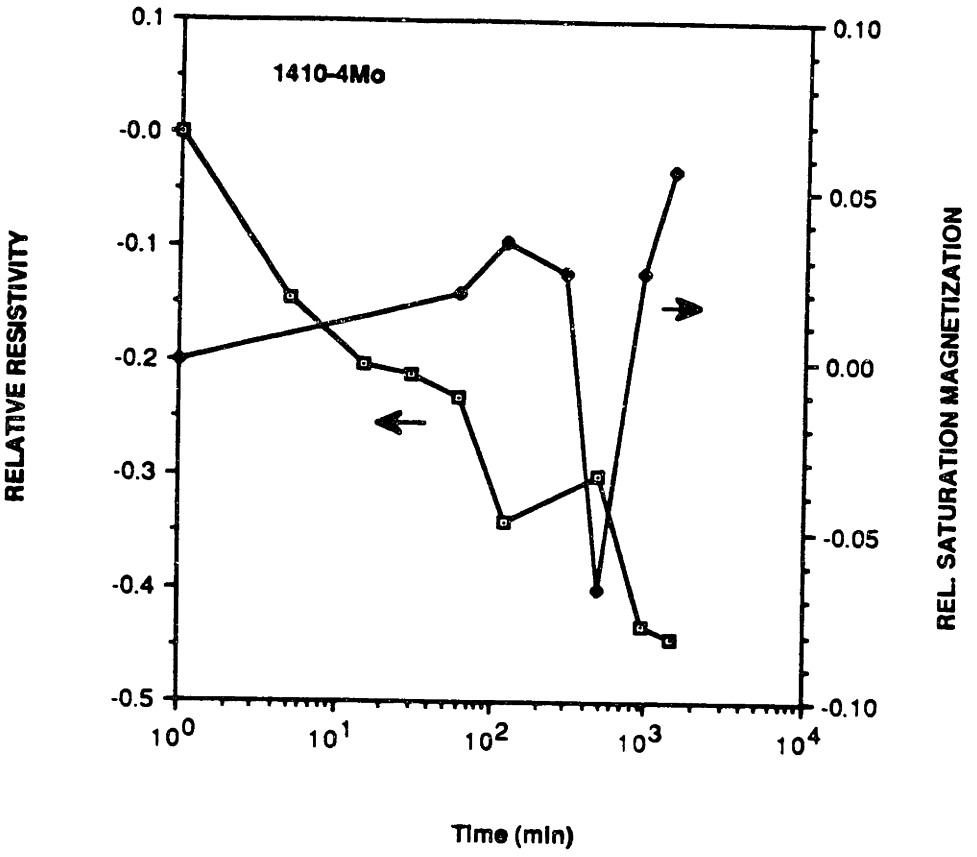

Fig.5.11 Relative resistivity and saturation magnetization as a function of tempering time for 1410-4Mo steel tempered at 500°C and cooled to room temperature.

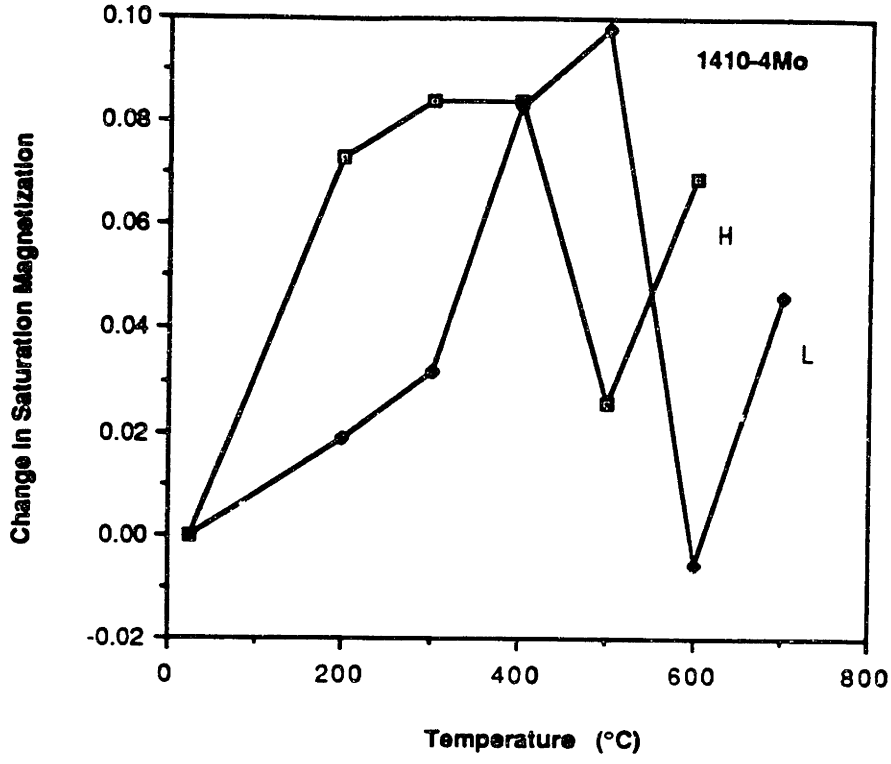

Fig.5.12 Saturation magnetization change relative to the as-quenched condition vs tempering temperature in 1410-4Mo steel for two carbon contents, H: 0.29wt%C and L: 0.23wt%C.

TEM observations revealed that the austenite in the 1410-4Mo precipitates on the lath boundaries of the martensitic matrix thus forming , an interlath dispersion. Fig.5.13 shows a BF/DF image of interlath austenite films for specimens tempered for 8h at 500°C. Note that at this tempering time the size of the films is still quite small. However, after tempering beyond 8h, the films grow and lose stability. This is shown in Fig.5.14 for 13h at 500°C and indicates that austenite particles link together along a given lath boundary and form relatively long austenite films resulting in loss of austenite stability. These TEM observations are consistent with the resistivity results discused earlier, indicating loss of austenite stability for tempering times beyond 8h.

Therefore, at short tempering times, the austenite is stabilized due to size effects but it very soon loses stability with tempering time due to growth of the interlath films. However, at longer tempering times the austenite tends to be chemically stabilized due to Ni enrichment. To explore these effects, a single treatment of 300h at 600°C was performed on the 1410-4Mo steel. Fig.5.15 shows a STEM micrograph in (a) and a corresponding Ni X-ray map, indicating particles highly enriched in Ni. These particles were identified with microdiffraction (shown in (c)) to have an FCC structure. The Ni content of the austenitic particles, measured by STEM microanalysis, was 30 wt%. This value is in good agreement with the Thermocalc prediction of 34 wt% Ni for austenite in equilibrium with ferrite at 600°C in the Fe-Ni-Co system, as Fig.5.5 indicates.

However, this type of stabilization, i.e.long-time tempering to reach the equilibrium Ni composition in the austenite, is not recommended for two reasons. First, dramatic decreases in strength occur due to coarsening of the M_2C carbide strengthening dispersion as indicated in Fig.5.9. Moreover, more stable carbides ($M_{23}C_6$ and M_6C) form with a much coarser dispersion which is detrimental to fracture toughness. These effects are illustrated in Fig.5.16. In

(a) the M_2C carbides (needle-shaped) are transforming to more stable carbides, while in (b) the M_2C carbides measure 200Å in length; this represents significant coarsening compared to the 50Å carbide length at peak toughness.

The most important conclusion from these experimental observations is that size stabilization dominates at short tempering times while chemical stabilization dominates at longer tempering times when the system is approaching equilibrium.

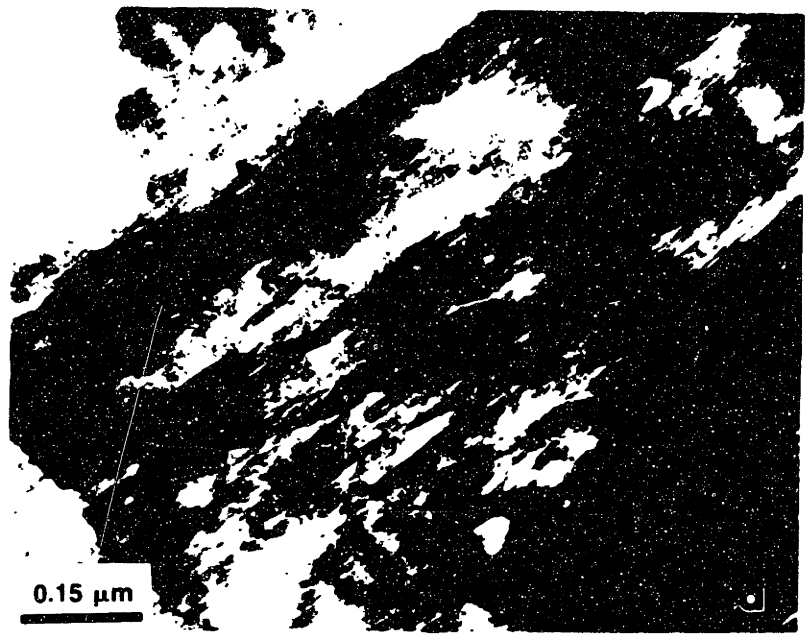

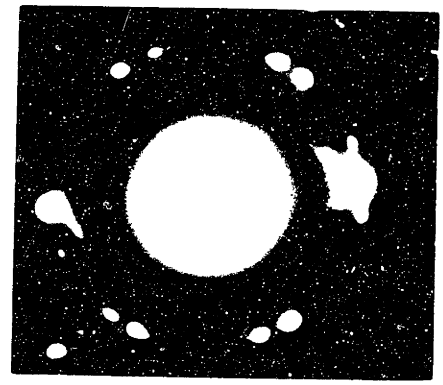

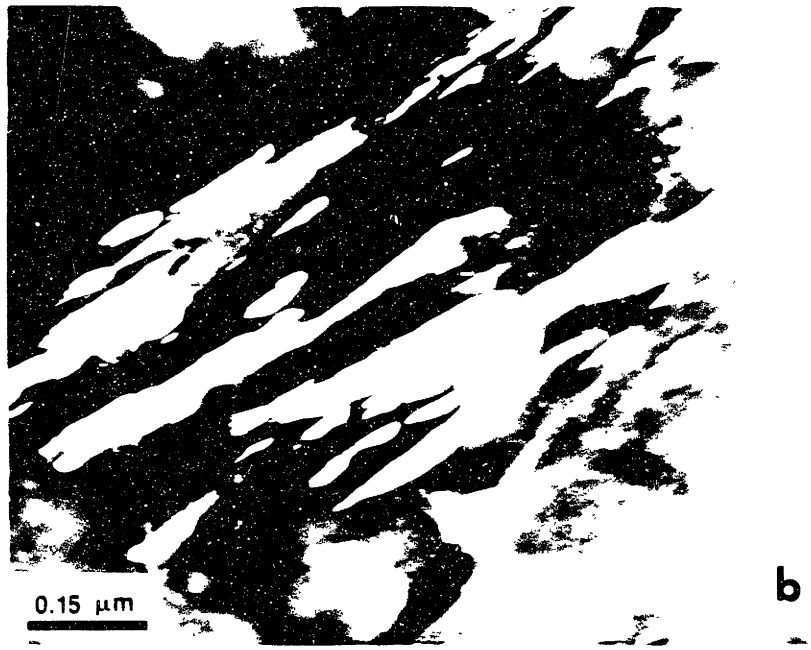

Fig. 5.13

TEM micrograph showing a bright field (a) and a dark field(b) image of interlath austenite films in 1410-4Mo tempered for 8h at 500°C. The dark field image was formed using austenite reflections from a selected area diffraction pattern of (a).

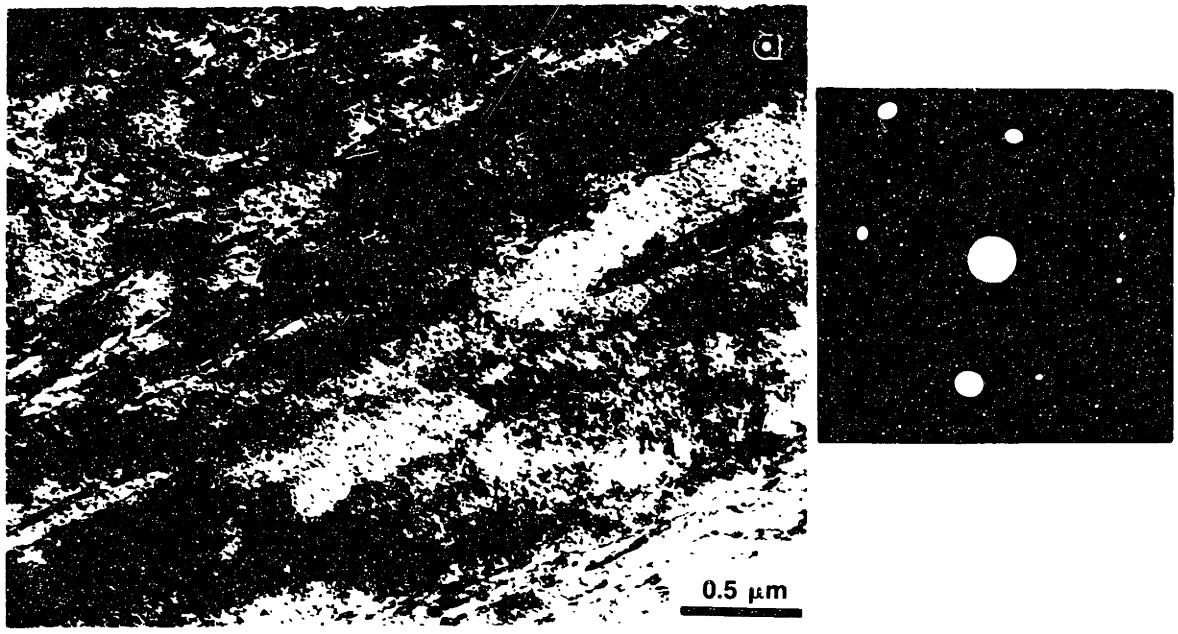

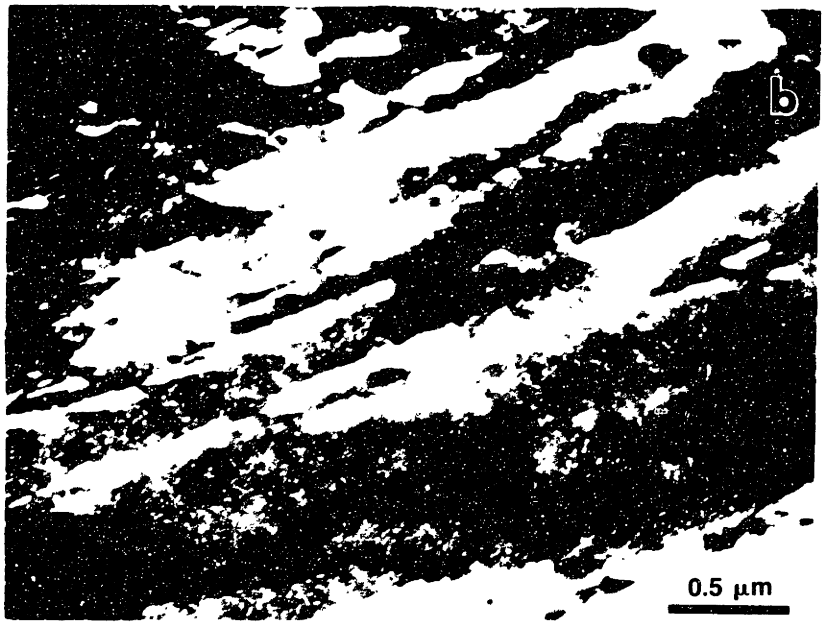

Fig. 5.14

TEM micrograph showing a bright field (a) and a dark field (b) image of interlath austenite films in 1410-4Mo tempered for 13 h at 500°C.

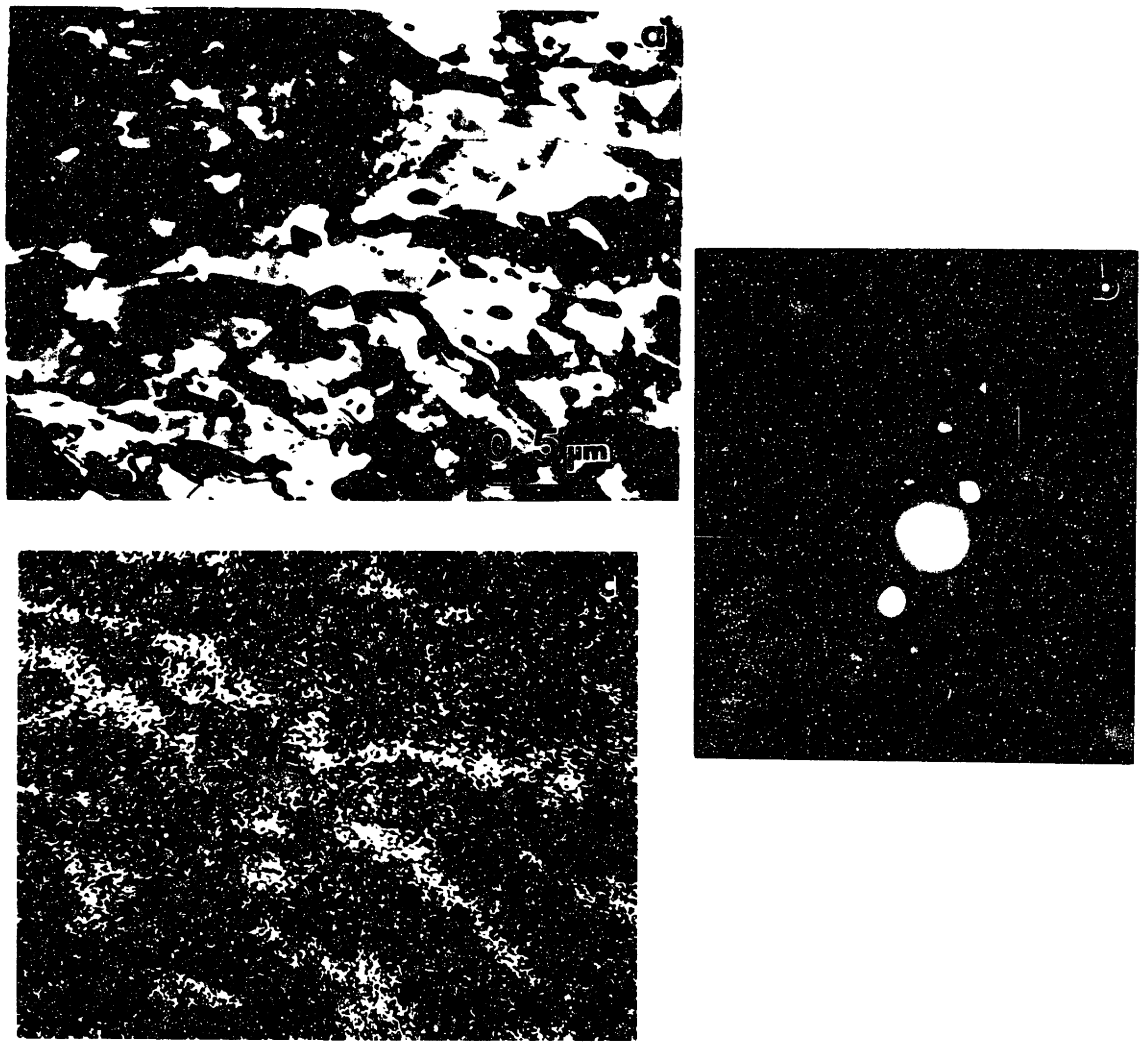

Fig. 5.15

STEM micrograph (a) indicating austenite particles that formed during tempering of 1410-4Mo steel at 600°C for 300h. The austenite particles were identified with microdiffraction shown in (b). The Ni X-ray map in (c) corresponds to the area shown in (a) and indicates a considerable Ni enrichment of the austenite particles.

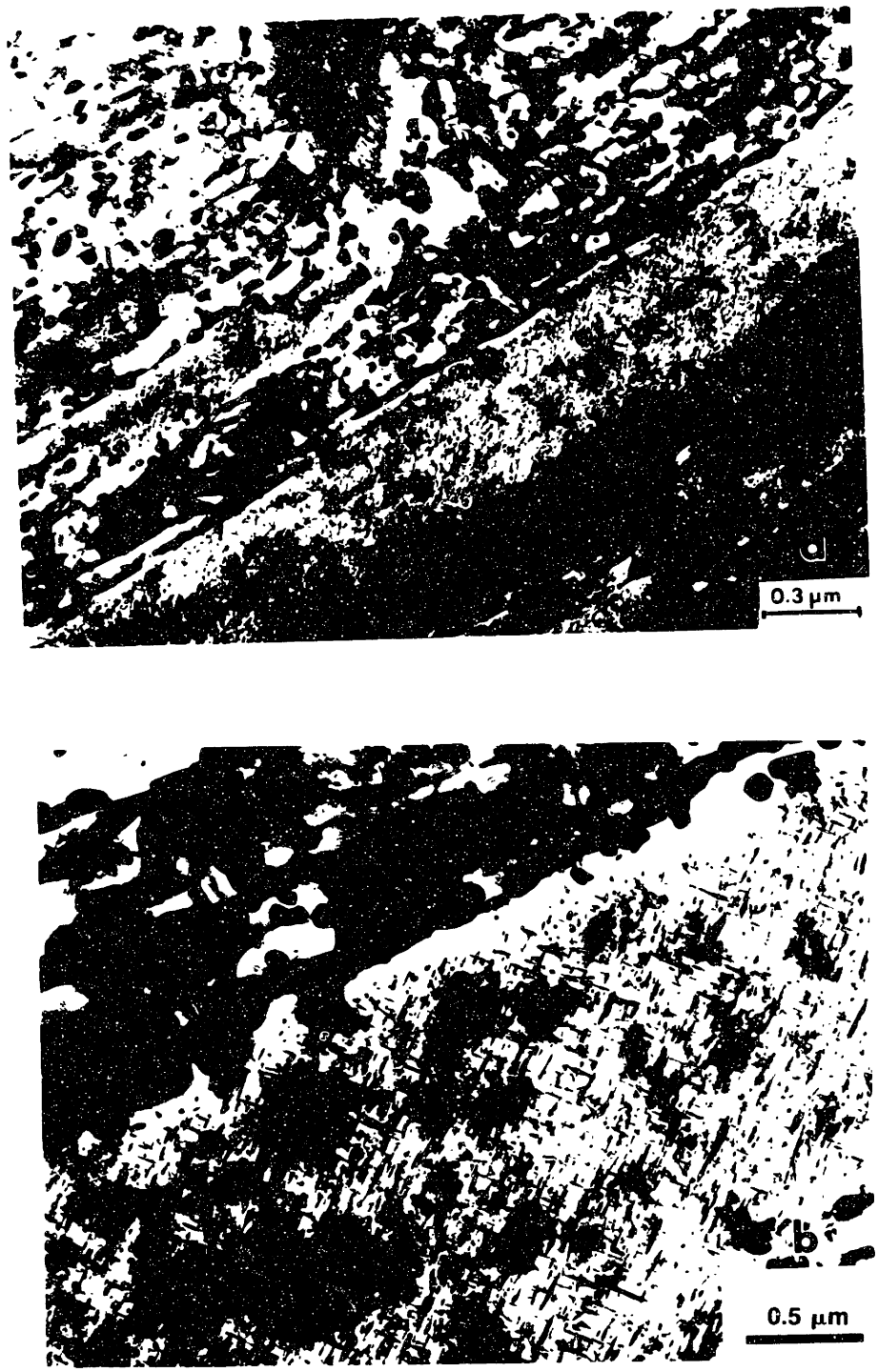

Fig. 5.16

TEM micrograph indicating transformation of M_2C carbides (needle-shaped) to other more stable carbides in (a) and significant coarsening of the M_2C dispersion in (b). 1410-4Mo steel, tempered at 600°C for 300h.

AF1410 Steel

AF1410 is a commercially available steel with an excellent combination of strength and toughness. It was selected for the present research to study the austenite stabilization and transformation toughening effects because of existing information in the literature about its tempering response and mechanical behavior[47,48].

Austenite volume fraction was measured using X-ray diffraction techniques, described in chapter 3. Fig.5.17(a) shows the volume fraction of austenite as a function of tempering temperature for 5h of tempering time. The curve labeled RT corresponds to measurements performed after the specimens were quenched to room temperature from the indicated tempering temperature. The curve labeled LN denotes measurements performed after the specimens were further cooled to liquid nitrogen temperature. The difference between these two curves gives a good indication of the thermal stability of the precipitated austenite. Austenite that forms between 500 and 600°C is very stable but loses stability at higher tempering temperatures. Fig.5.17(b) presents the volume fraction of precipitated austenite vs tempering time for 500°C and 650°C tempering temperatures. Again stable austenite precipitates at short tempering times. These results suggest that stable austenite dispersions form on simple tempering when low temperatures and short tempering times are used. However, under these conditions the amount of austenite is relatively small. A combination of large amounts and stability can be achieved only through multi-step heat treatments aiming at size refinement and compositional enrichment of the austenite dispersion. This topic is treated in the next section.

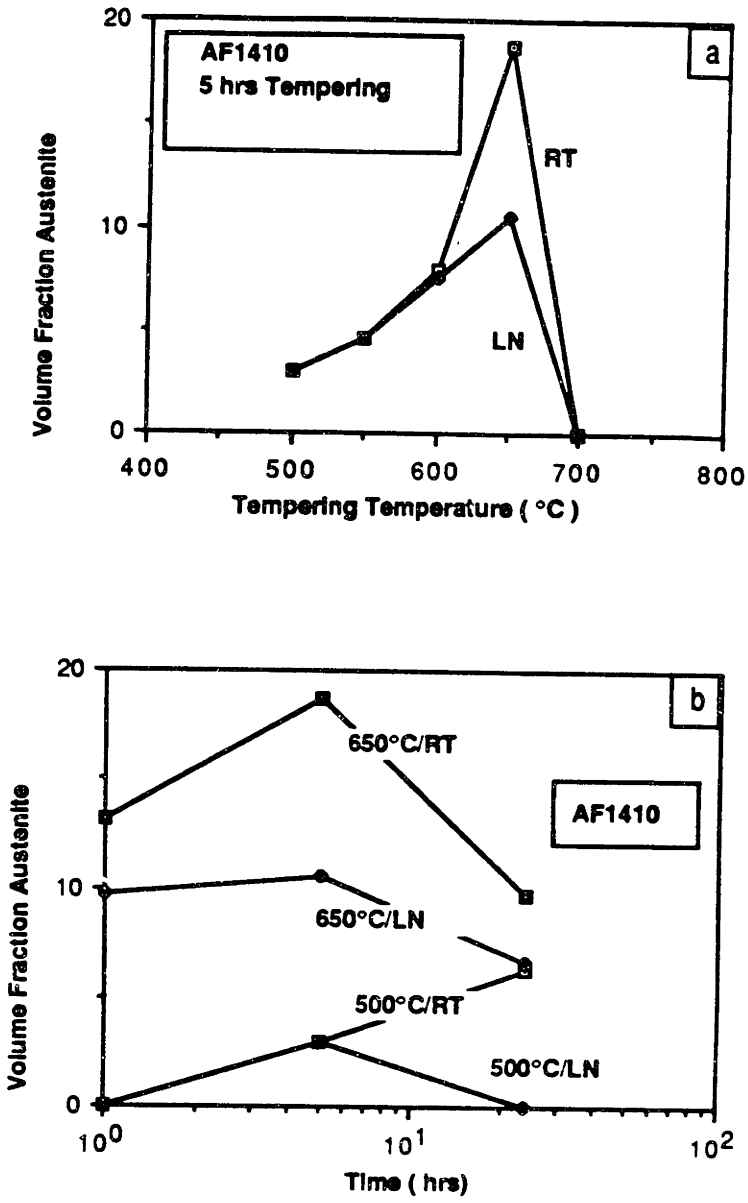

Fig.5.17 Austenite volume fraction vs tempering temperature (a) and vs tempering time in (b) in AF1410 steel. RT represents measurements performed after the specimens were quenched to room temperature while LN represents measurements performed after the specimens were further cooled to liquid nitrogen temperature. The austenite volume fraction was measured by standard X-ray diffraction techniques.

5.4 Multi-step Heat Treatments For Austenite Stabilization.

5.4.1 Model Treatments

Heat treatment for austenite stabilization is directed at size refinement and compositional enrichment of the austenite particles. Two methodologies were employed to achieve this goal.

First, a fine dispersion of intralath austenite can form if a second dispersed phase can provide nucleation sites for the austenite. Furthermore, if this dispersed phase can be previously enriched in γ-stabilizing solutes, then the austenite will inherit a considerable amount of these elements and be chemically stabilized. In the present study, a dispersion of alloy-enriched cementite was adopted for heterogeneous nucleation of the austenite. The cementite was precipitated at a low-temperature step (420°C), whereas the austenite was formed at a higher-temperature step (510°C). The resulting austenite is termed cementite-nucleated austenite.

On the other hand, a fine ,uniform dispersion of intralath austenite can form directly by increasing the driving force for austenite precipitation. This was achieved by a short-time high-temperature step (600°C/15min), followed by a lower-temperature step (510°C/8h). An additional feature of this treatment was that the diffusivity of Ni is enhanced at the high-temperature step resulting in higher Ni-enrichment of the austenite particles. The resulting austenite is termed direct-nucleated.

A common characteristic of both treatments is the formation of interlath austenite. Later in this section, it will be shown that this austenite has lower stability than the intralath austenite.

Table 5.4 summarizes the heat treatments used for austenite stabilization in the AF1410 steel. The Table also lists the resulting hardness values after the

completion of these treatments. In all these instances, the austenitizing temperature was 830°C for 1h followed by oil quenching.

The 510°C/5h treatment is standard for the AF1410 steel, providing the best combination of strength and toughness to date.

The 510°C/8h treatment produces stable austenite on simple tempering as evident from the resistivity, magnetization and TEM results discussed earlier. This treatment was used for reference purposes since the last step in all multi-step treatments was 510°C/8h.

The next two double treatments in Table 5.4, 420°C/1h+510°C/8h and 420°C/5h+510°C/8h correspond to the cementite-nucleated austenite treatments. The 600°C/15min+510°C/8h is the direct-nucleated austenite treatment, and the triple treatment 420°C/1h+600°C/15min+510°C/8h is a combined treatment. It is interesting to note that all these multi-step treatments yield the same hardness, with the exception of the 420°C/5h+510°C/8h treatment which results in considerable hardening. The discussion will be focused now on the 420°C/5h+510°C/8h and 600°C/15min+510°C/8h treatments because they reflect the general characteristics of cementite-nucleated and direct-nucleated austenite treatments.

Cementite-nucleated austenite treatment (420°C/5h+600°C/8h)

As mentioned before, the purpose of this treatment is to produce a fine dispersion of stable intralath austenite by heterogeneous nucleation on alloy-enriched cementite. Table 5.5 shows the high-resolution STEM microanalysis results obtained for this treatment. At 420°/5h a dual dispersion of cementite forms; Mo-rich and Cr-rich cementite. Then at 510°C the Mo-rich cementite dissolves completely to form the M_2C carbide strengthening dispersion while the Cr-rich cementite being stabilized by Cr does not dissolve. A fine dispersion

Table 5.4 Heat Treatments for Austenite Stabilization in AF1410 Steel.

TREATMENT	HARDNESS (R_C)	REMARKS
510°C / 5h	48	Standard Treatment
510°C / 8h	46	Slightly Overaged
420°C / 1h 510°C / 8h	48	Cementite-Nucleated Austenite
420°C / 5h 510°C / 8h	51.5	//
600°C / 15min 510°C / 8h	48	Direct-Nucleated Austenite
420°C / 1h 600°C / 15min 510°C / 8h	48	Combined Treatment

NOTE : Austenitizing treatment 830°C / 1h

of intralath austenite nucleates then on the Cr-rich cementite particles at 510°C. Fig5.18 shows a STEM micrograph illustrating multiple nucleation of austenite particles from a single cementite particle.The compositions of the austenite particles, together with the compositions of the cementite particles that they nucleated on, are given in Table 5.5. The results indicate a considerable Ni enrichment of the austenite particles to about 19wt% and a concurrent depletion of Ni in the cementite particle, suggesting solute transfer from the cementite to the austenite. The resulting austenite dispersion is very fine (<100nm) and enriched in Ni. Also present in the microstructure are interlath austenite particles which nucleate on the lath boundaries of the martensitic matrix. These austenite particles are also quite small but with a lower Ni enrichment (14w/o) than the intralath austenite particles, having therefore lower stability. A shortcoming of this treatment however is the isolated cementite particles which remain undissolved and can act as void-nucleating particles degrading the fracture toughness of the material.

An important characteristic of the treatment is the resulting hardening (51.5 Rc compared to 46 Rc for the 510°C/8h). This is most likely due to an increased driving force for M_2C carbide precipitation, leading to a much finer dispersion and decreased mean free path of the M_2C carbides. This is indicated in Fig.5.19 which shows FIM images of the M_2C carbides for the two treatments. The increase in driving force is attributed to a reduction in Cr in solution due to the formation of Cr-rich cementite during the first step of the treatment.

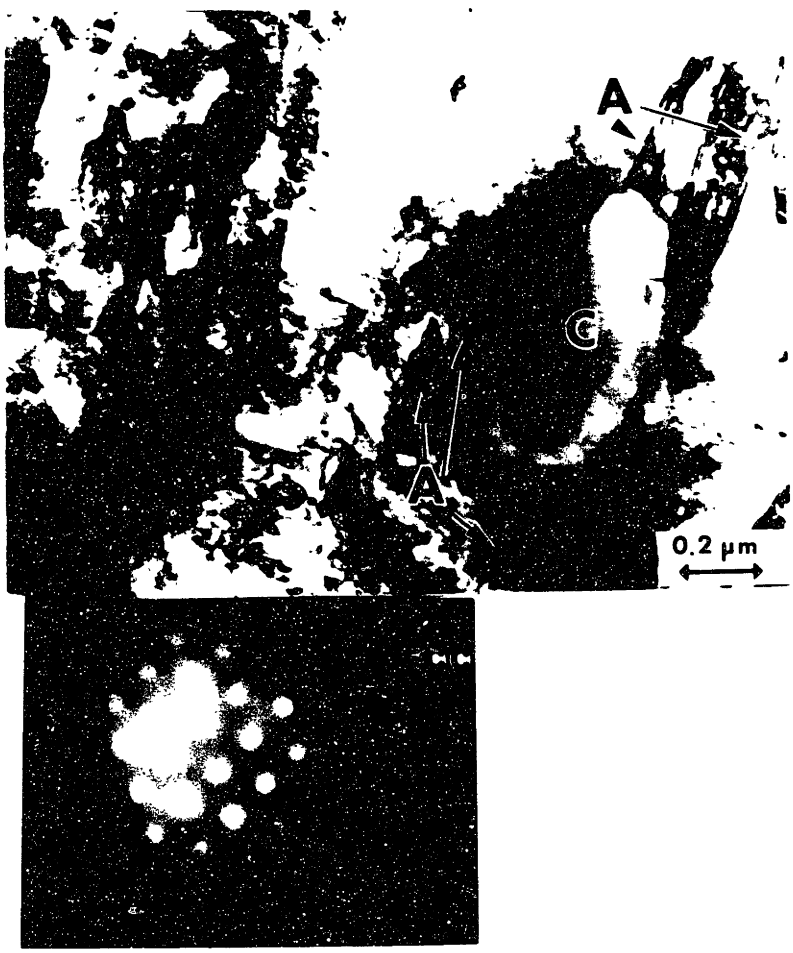

Fig. 5.18

STEM micrograph showing austenite particles (A) nucleating on a cementite particle (C) during the "cementite" treatment (420°C/5h + 510°C/8h) in AF1410 steel. The microdiffraction pattern was taken from one of the austenitic regions and reveals the FCC structure.

Table 5.5 STEM Microanalysis 420°C/5h + 510°C/8h Treatment

	420°C / 5h			510°C / 8h		
	Mo-rich Cementite	**Cr-rich Cementite**	**Intralath Austenite**	**Cementite**	**Interlath Austenite**	**Isolated Cementite**
Size	30-50 nm	30-70 nm	< 100 nm	300 nm	100-200nm	50 nm
Fe	14.91	30.00	69.1	31.3	70.7	55.0
Co	3.93	2.76	10.19	3.2	11.9	7.45
Ni	1.00	2.74	**18.80**	0.3	**14.1**	4.6
Cr	15.46	61.00	1.85	60.6	3.3	30.56
Mo	64.56	3.35	0.00	4.40	0.00	2.45

* Compositions are in wt%

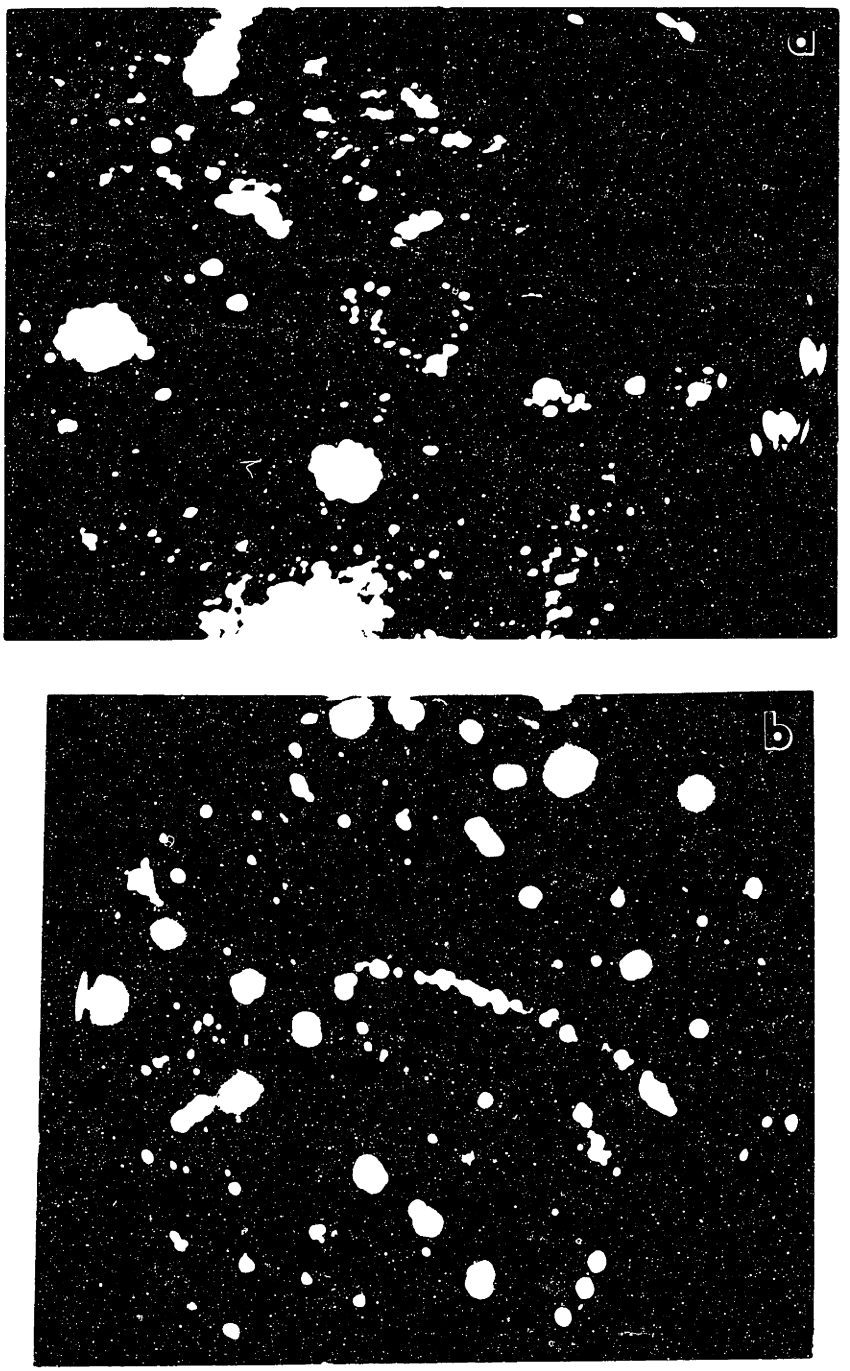

Fig. 5.19

FIM images of M_2C carbides in AF1410 steel for the single treatment (510°C/8h) in (a) and the "cementite" treatment (420°C/5h + 510°C/8h) in (b) taken under the same operating voltage of 15 kV.

Direct-nucleated austenite (600°C/15min+510°C/8h)

As mentioned earlier, the purpose of this treatment was both to increase the driving force for austenite precipitation and to enhance the diffusivity of Ni. The combination of these effects produces an exceptonally stable austenitic dispersion. Fig.5.20 presents a TEM micrograph indicating the presence of a uniform intralath ultra-fine (10-20 nm) austenitic dispersion. Fig.5.21 is a BF/DF high-magnification image of the intralath austenite particles. An interlath austenitic dispersion also forms heterogeneously on the lath boundaries of the martensitic matrix. This dispersion is much coarser than the intralath dispersion.

The composition of the austenite particles was measured by high-resolution STEM microanalysis and the results are shown in Table 5.6. Data for the 510°C/8h as well as for the cementite-nucleated austenite treatments are shown for comparison. These findings indicate substantial Ni enrichment of the austenite particles (up to 30wt%) This compositional enrichment together with their very small size makes these particles extremely stable.

Fig. 5.20

TEM micrograph showing a very fine dispersion of intralath austenite that precipitated during the "direct" treatment (600°C / 15min + 510°C/8h) in AF1410 steel. Interlath particles (on the lath boundaries of the martensitic matrix) are also shown.

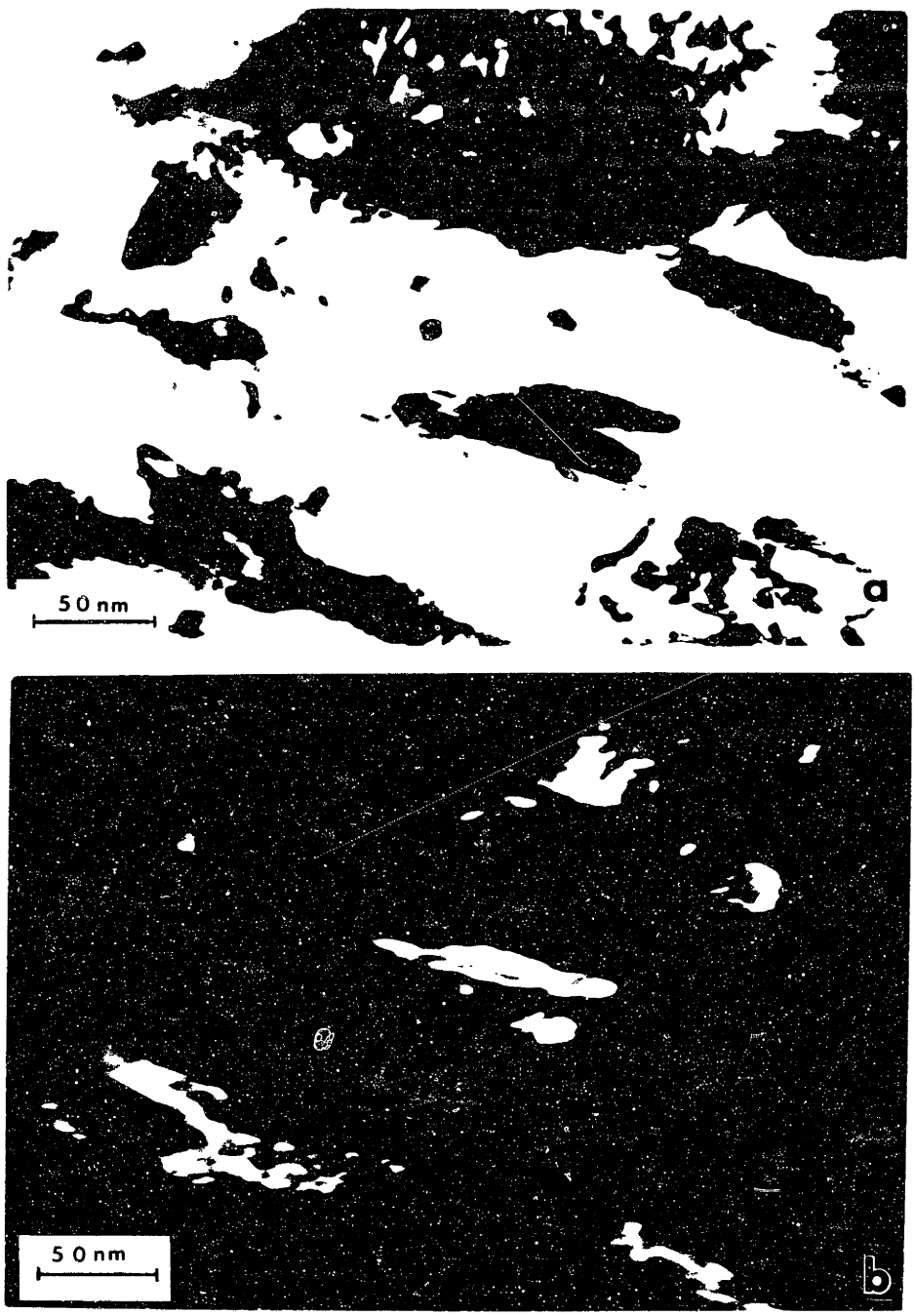

Fig. 5.21

TEM micrograph showing a BF image in (a) and a DF image in (b) of intralath austenite particles nucleated during the "direct-nucleation" treatment (600°C/15min+510°C/8h).

Table 5.6 STEM Microanalysis of Precipitated Austenite in AF1410 Steel

	Single Treatment	Cementite-nucleated		Direct-nucleated	
	510°C/8h	420°C/5h + 510°C/8h		600°C/15min + 510°C/8h	
	Interlath	Interlath	Intralath	Interlath	Intralath
Size(nm)	200	100-200	< 100	100-200	10-20
Ni	14.0	14.1	18.8	16.57	29.1
Co	13.2	11.9	10.19	14.85	10.5
Cr	2.8	3.3	1.85	4.2	4.2
Mo	1.0	0.0	0.0	2.1	1.9
Fe	69.0	70.7	69.1	62.28	54.3

* Compositions are in wt%.

Fracture Toughness (CVN).

Room temperature Charpy-V-notch impact testing was performed for preliminary assessment of the transformation toughening contributed by precipitated austenite. Testing was performed for all treatments listed in Table 5.4 and the resulting impact energy is shown vs hardness in Fig.5.22.

The direct-nucleated austenite treatment for 600°C, 15min provides considerable toughening (105 J) relative to the standard treatment (84 J) at no loss of hardness. The 20 J toughness increment is attributed to dispersed-phase transformation toughening arising from the ultra-stable austenite dispersion.

The cementite-nucleated austenite treatment causes a decrease in toughness due to the cementite left undissolved. A similar situation exists with the 420°C/1h+510°C/8h treatment.

Although the combined triple treatment gives a higher toughness than the standard treatment, it does not provide the high toughness of the direct-nucleated austenite treatment because of undissolved cementite from the first step.

Table 5.6 shows that the highest Ni enrichment of the austenite particles is achieved with the direct-nucleated austenite treatment. The average austenite particle size is also the smallest with this treatment. These factors in combination with the absence of undissolved cementite produce substantial toughening, and should prove of considerable technological importance to this class of ultrahigh-strength high-toughness steels.

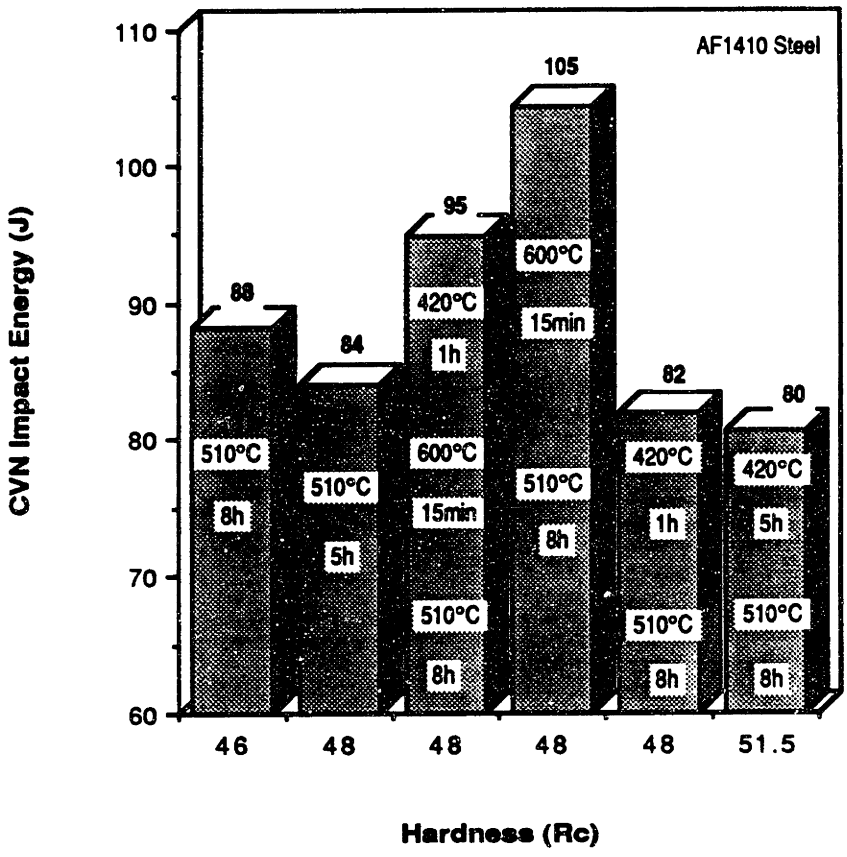

Fig.5.22 Charpy V-notch impact energy vs hardness comparing a series of single and multi-step heat treatments in AF1410 steel.

5.4.2 The Direct Treatment For Austenite Stabilization

5.4.2.1 Introduction

It was demonstrated in the previous section, that from all the model treatments examined, the direct-nucleated austenite treatment (called "direct" from now on) led to substantial size refinement and compositional enrichment of the precipitated austenite. This resulted in a significant enhancement of the Charpy energy relative to the standard single treatment with identical hardness. An attempt will be made in this section to analyze in more detail the direct treatment. First, variations in the first step of the treatment (the high-temperature step) are examined in terms of strength/toughness combinations. This enables the optimum condition to be found. Then follows a discussion on austenite nucleation, and finally the tensile properties and sharp-crack fracture toughness (J_{IC}) for the direct treatment are compared with the standard single treatments for the AF1410 steel.

5.4.2.2 Variations of the direct treatment.

The effect of the first step of the direct treatment on the strength/toughness combinations is now examined. The second step of the treatment was kept fixed at 510°C/8h. The following first-step tempering treatments were performed: 570°C/15min, 570°C/30min, 600°C/5min, 600°C/30min, 630°C/15min, and 630°C/30min. The Charpy impact energy is plotted vs hardness (in Rc points) in Fig.5.23. The contours correspond to iso-K lines, where K is defined by the relation:

$$K = \frac{C_v}{1356} \, (HRC - 35)^{-3}$$

where Cv is the Charpy impact energy in Joules and HRC is the hardness in Rokwell "C" points. The above equation represents the strength/toughness combinations to which steel manufacturers compare their products. K then defines the technological value of a steel in terms of strength/toughness combinations. The current technology limit is given by the standard treatment for the AF1410 steel (510°C/5h) and is K=140. Relative to that, the direct treatment (600°C/15min+510°C/8h) yields a K-value equal to 170 which represents a technological advance relative to the standard treatment. The 570°C treatments yield even higher K-values, but since the direct treatment had identical hardness with the standard treatment, it was selected for further study.

5.4.2.3 Austenite Nucleation.

The composition of the austenite precipitated during the direct-nucleation treatment (shown in Table 5.6) is close to the equilibrium austenite composition (shown in Table 5.1). This suggests nucleation of equilibrium austenite with full partitioning. Estimated driving forces, using Thermocalc, for austenite precipitation were used as input to the calculation of nucleation energetics. The results, presented in detail in appendix B, showed that homogeneous nucleation, either coherent or semicoherent, is not feasible under the available driving forces, due to the large strain energy accompanying austenite nucleation.

The very high dislocation density present in the martensite of this class of high-Co/Ni steels, suggests that austenite particles could be dislocation-nucleated. As the calculations in appendix B show, the interaction energy between coherent austenite embryos with the stress field of edge dislocations can contribute to the total driving force. However, the large strain energy contribution results in a minimum in the ΔG vs r curve (free energy vs nucleus

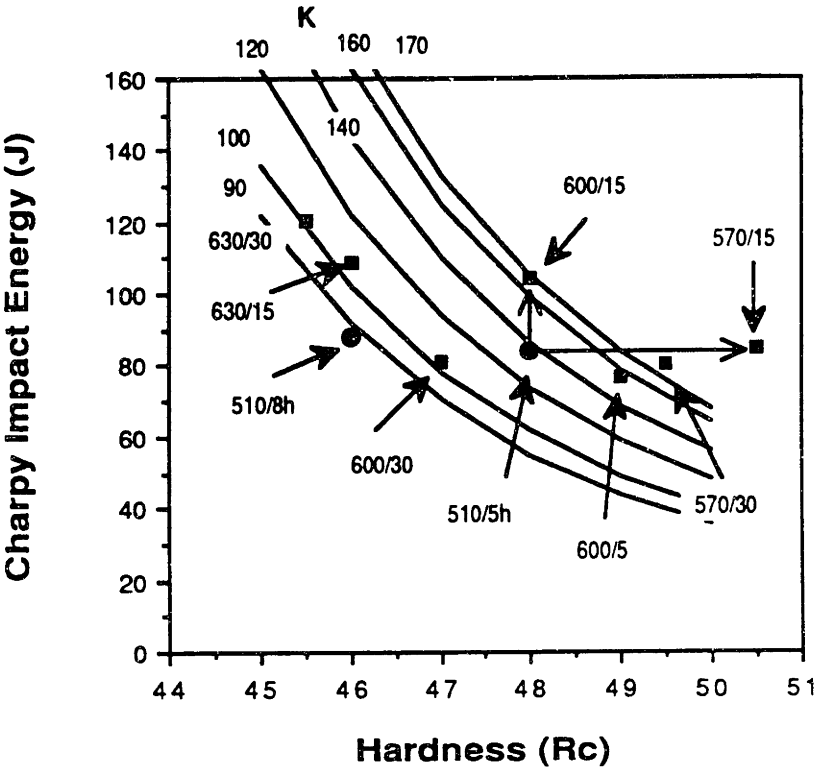

Fig.5.23 Charpy V-notch impact energy (C_v) vs hardness (HRC) for a series of direct treatments in AF1410 steel were the second step of the treatments is fixed at 510°C/8h and the first step varies as indicated. The solid lines correspond to iso-K contours where K is defined by the relation: $C_v = 1356K(HRC-35)^{-3}$. The solid round points correspond to the single tempering treatments. The light arrows originating from the 510°C/5h treatment indicate advances in the strength/toughness combinations relative to the standard treatment. The temperatures are in °C and the times in min.

size) corresponding to the formation of stable austenite nuclei that cannot grow with further reduction in the free energy of the system. In contrast, the interaction between semicoherent nuclei and edge dislocations reduces the strain energy enough to lead to barrierless nucleation. Therefore, nucieation of semicoherent austenite on dislocations is cosidered to be a feasible mechanism of austenite precipitation. The point has to be made, however, that a complete description of the dislocation structure of the martensite/austenite semicoherent interphase boundary is required to accurately determine the interfacial energy term.

Another possible nucleation mechanism is the interaction of austenite nuclei with carbides, mainly M_2C, which are precipitated simultaneously with austenite. However, a complete treatment of austenite nucleation is not within the scope of this research.

5.4.2.4 Tensile properties and sharp-crack fracture toughness.

Tensile testing and J_{IC} fracture toughness tests were performed for the direct treatment (600°C/15min+510°C/8h) and for the single treatments 510°C/5h and 510°C/8h. The yield strength, UTS, uniform strain, fracture strain, reduction in area (RA), elongation, and J_{IC} fracture toughness are listed in Table 5.7. The volume fraction of precipitated austenite, determined by X-ray diffraction, is also shown in the same table. Here, the direct treatment should be compared with the 510°C/8h single treatment since they have almost identical yield strengths and UTS. The direct treatment possesses higher uniform ductility and fracture strain as well as reduction in area and elongation relative to the single treatment. The percent increase in these properties varies from 5 to 15%.

The J_{IC} fracture toughness for the direct treatment is significantly higher than for the single treatment (250 KJ/m^2 relative to 201KJ/m^2) an increase of 25%. The percentage increase in J_{IC} is higher than the percentage increase in

the tensile properties, and suggests that the precipitated intralath austenite interacts more with the crack-tip stress state rather than with the uniaxial tension stress state. This indicates that the fine intralath austenite has near optimum stability for the crack-tip stress-state and is too stable for uniaxial tension. The enhancement of the tensile uniform ductility is most probably due to the less stable interlath austenite.

Fig.5.24 presents the J-Δa curves (R-curves) for the direct and the single treatments. The direct treatment not only possesses higher resistance for the initiation of crack growth (J_{IC}) but higher resistance for crack propagation as well, compared to the single treatments. This is shown by the larger slope of the R-curve for the direct treatment.

Table 5.7 Tensile Properties and J_{IC} Fracture Toughness for the Single and Double Treatments in AF1410 Steel.

	Treatments		
	Single 510°C/5h	**Single** 510°C/8h	**Direct** 600°C/15m+510°C/8h
Yield Stress, Mpa	1551 (225)	1362 (197)	1370 (199)
UTS	1796 (261)	1576 (228.6)	1573 (228)
Uniform Strain	0.07	0.096	0.111
Fracture Strain	0.559	1.21	1.35
% RA	45.4	70.3	74.0
% EL	17.7	21.8	23.4
J_{IC} (KJ/m^2)	**178**	**201**	**250**
Austenite			
Volume fraction	0.03	0.06	0.15

* Values in parentheses are in Ksi

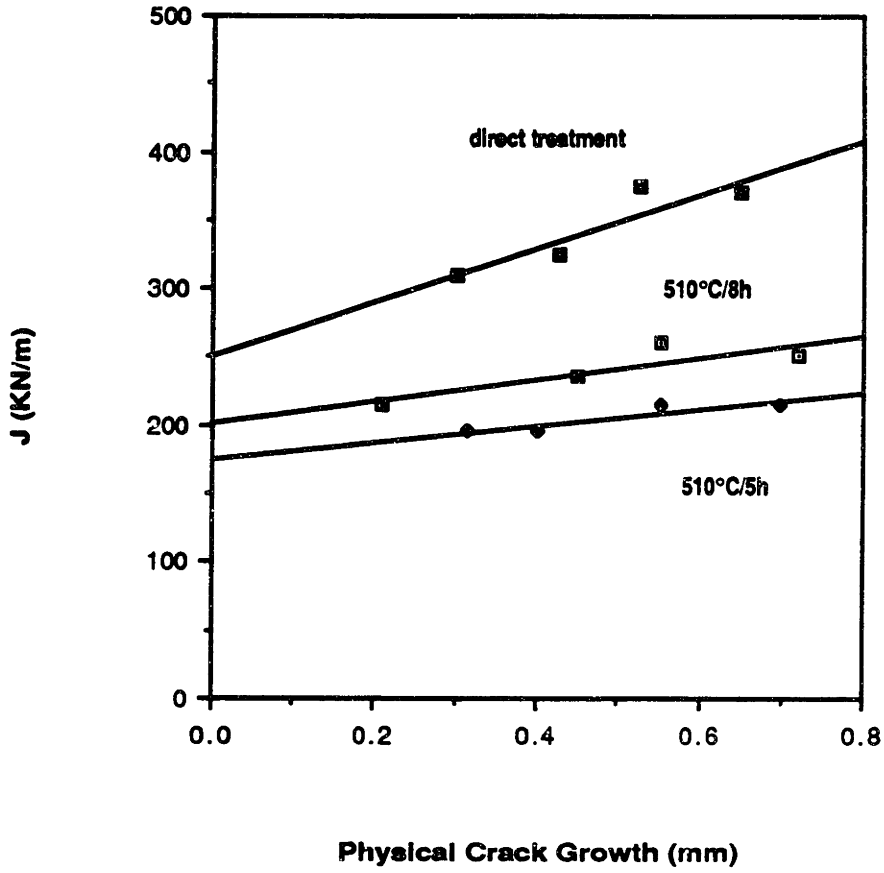

Fig.5.24 J vs Δa curves comparing the direct treatment with the single standard treatments in AF1410 steel. The direct treatment possesses higher J_{IC} and higher resistance for crack growth.

6. ALLOY DESIGN FOR ENHANCED TRANSFORMATION TOUGHENING

6.1 Basic Principles

The alloy design principles discussed in this section are aimed towards selecting alloy compositions that optimize austenite stability and transformation volume change. Austenite stabilization is important because it determines the transformation-plasticity interactions of the dispersed austenite with the shear localization process ahead of a crack tip. The amount of toughening is also affected by the transformation volume change.

In quantitative terms, for transformation toughening to occur, the M_S^{σ} temperature for the crack-tip stress state of the austenitic dispersion should be just below the anticipated service temperature, in this case room temperature. This condition then prescribes the microstructural requirements, i.e., austenite particle size and composition, to obtain this degree of stability. Thermodynamic calculations can then be used to select alloy compositions that achieve this stability of the precipitated austenite.

The alloy design procedure, outlined above, is then subjected to the constraint that the alloy compositions selected should maximize the transformation volume change. Alloy compositions affect the volume change through the composition dependence of the lattice parameters of the austenite and martensite. Magnetic changes, such as ferromagnetism and the INVAR effect, become important in the austenite, which can reduce the transformation volume change and the resulting toughening.

It is, therefore, important to select alloy compositions that ensure high austenite stability while promoting a large transformation volume change. This then establishes the framework for alloy design to achieve transformation toughening.

6.2 Transformational Volume Change.

Enhanced transformation toughening can be achieved through a large transformation volume change. The volume change interacts in two ways with the stress field at the crack tip to increase toughness: 1. $p\Delta V$ energetic interaction, and 2. reduction of stress triaxiality, which in turn lowers the critical strain-hardening rate for void-induced shear instability.

The transformational volume change is subjected to some control through the composition dependence of the lattice parameters of austenite and martensite. Alloy compositions can then be designed that result in high $\Delta V/V$ and, hence, enhanced toughening. The volume change resulting from the martensitic transformation FCC⇒BCC is related to the lattice parameters α_{FCC} and α_{BCC} of the two phases as:

$$\frac{\Delta V}{V} = 2\left[\frac{\alpha_{BCC}}{\alpha_{FCC}}\right]^3 - 1 \qquad (6.1)$$

The lattice parameters are functions of composition:

$\alpha_{FCC}=f_1(X_i)$, $\alpha_{BCC}=f_2(X_i)$, i=Fe,Co,Ni,Cr

where X_i is the mole fraction of element i. In particular, the form of the function f_1 for the FCC phase is influenced by magnetic changes, such as volume magnetostriction and the INVAR effect, both of which increase the value of α_{FCC}

and, hence, reduce $\Delta V/V$. An attempt will be made here to develop analytical expressions for α_{FCC}, taking into account these magnetic effects. The two-gamma states formalism developed by Tauer and Weiss[68] is used to describe the INVAR effect on α_{FCC}.

6.3 The Two-Gamma States Model.

In a study designed to separate the contribution of magnetic structure to phase transformations, Tauer and Weiss[69,70] attempted an analysis of the specific heat of various substances, including iron, by separation into magnetic, electronic, and lattice contributions. In order to equate the free energy of BCC and FCC iron at the α/γ transition at 910°C, it was necessary to postulate a sizeable magnetic entropy term for γ-iron, which was inconsistent with the absence of a specific heat anomaly at the Néel temperature. The high-temperature properties of γ-iron suggested ferromagnetic behavior with a large saturation magnetic moment, while the low-temperature properties suggested antiferromagnetic behavior with a much smaller magnetic moment. It was therefore proposed that there existed two discrete electronic states of γ-iron, γ_1 and γ_2, separated by a specific energy difference in equilibrium with each other in a manner corresponding to a two-level Schottky excitation[71]. Individual atoms are not considered to permanently possess either of the electronic configurations, but have a probability of exhibiting both states on a time-transient basis according to the ratio:

$$a = \frac{f}{1 - f} = (g_1 / g_0) \exp (- \frac{\Delta E}{RT}) \qquad (6.2)$$

where a is the probability of the upper energy state being occupied and f the corresponding fraction of iron atoms in the upper energy state. ΔE represents the energy difference between the two states and g_0 and g_1 the degeneracies of the upper and lower states respectively. The properties of the γ_1 and γ_2 states are presented in Table 6.1. In pure γ-iron, the antiferromagnetic (low volume) state is the ground state (T=0K). Addition of Ni, Co, and Cr reverses the relative stability between γ_1 and γ_2 promoting the ferromagnetic (high volume) γ_2 state. On the other hand, addition of Mn stabilizes the γ_1 state. These effects are shown in Fig.6.1, which presents the composition dependence of ΔE, the energy difference between the two states.

Table 6.1 Approximate values of lattice parameter, spin per atom, and Curie or Néel temperature of the two electronic structures of gamma-iron (reference 72).

	Crystal Structure	Lattice Parameter	Magnetic Structure	Spin per Atom (μ_B)	Curie or Néel Temp.
γ_1	FCC	3.54 Å	Anti-Ferro	0.5	80 K
γ_2	FCC	3.64	Ferro	2.8	1800 K

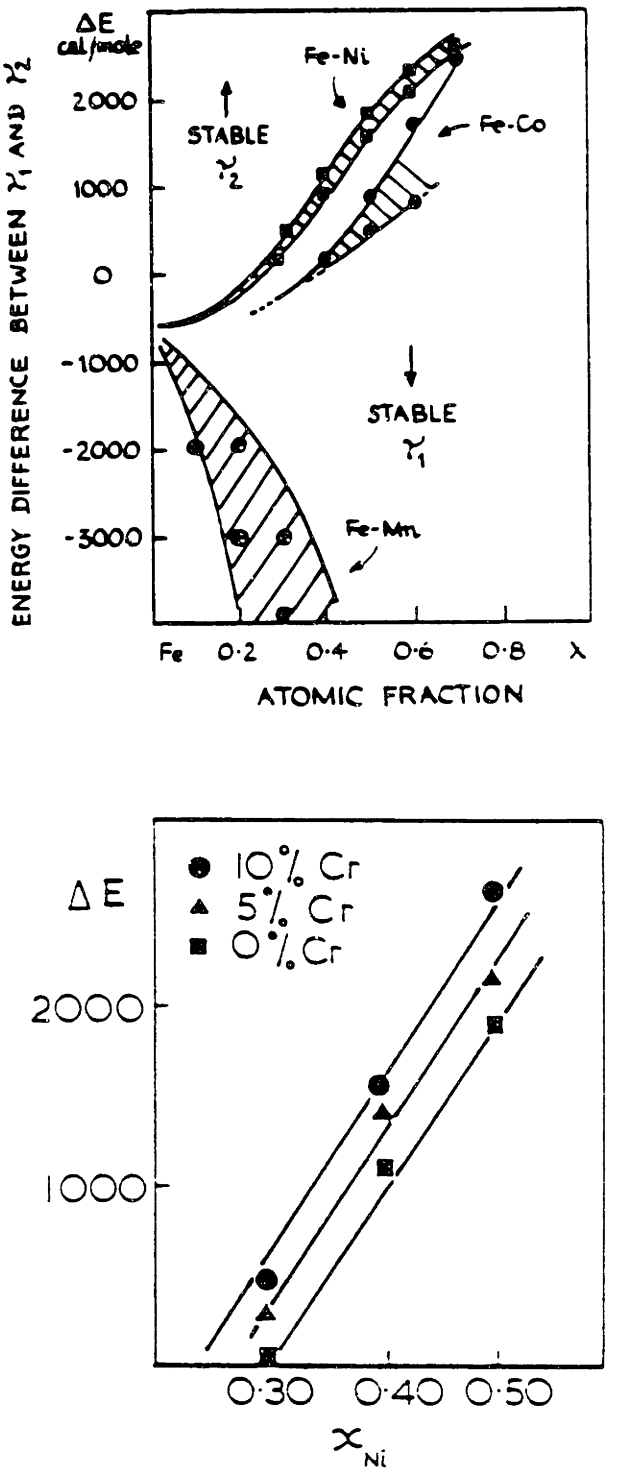

Fig.6.1 The effect of alloy additions Ni, Co, and Mn [70]in (a) and Cr [72] in (b) on the difference in energy ΔE between γ_1 and γ_2 states.

6.4 Lattice Parameters.

The formulation of the compositional dependence of the lattice parameter α_{FCC} is based on the description of two composition-dependent effects:

1. the effect of composition on the relative occupancy of the γ_1 and γ_2 states through the compositional dependence of ΔE, the energy difference between the two gamma states and;

2. the effect of composition on the overall magnetic moment, which influences the magnitude of volume magnetostriction.

These effects are studied in the Fe-Ni-Co-Cr system with the following procedure: an expression for the lattice parameter is derived in the Fe-Ni binary system which is adopted as a reference. Then the effect of Cr and Co on both the relative stability of γ_1 and γ_2 states and the magnetic moment is considered, to derive the final expression for α_{FCC}.

Using Vegard's law, the lattice parameter a for the Fe-Ni system is:

$$\alpha_{FCC} = (1 - X_{Ni}) \left[\alpha_{\gamma_2} . f_{\gamma_2} + \alpha_{\gamma_1} . f_{\gamma_1} \right] + X_{Ni}\ \alpha_{Ni} \qquad (6.3)$$

where $f_{\gamma 1}$ and $f_{\gamma 2}$ are the fractions of iron atoms in the γ_1 and γ_2 states respectively as defined by eq(6.2), and $\alpha_{\gamma 1}$,$\alpha_{\gamma 2}$ are the lattice parameters of the γ_1 and γ_2 states given in Table 6.1. X_{Ni} and α_{Ni} are the mole fraction and lattice parameter of Ni respectively. According to data on the composition dependence of ΔE by Weiss[70], $\Delta E=0$ at $X_{NI}=0.29$. Therefore, for $X_{Ni}>0.29$ the γ_2 state is stable. In order to develop eq(6.3) further, an analytical expression for $\Delta E(X_{Ni})$ is required. The following expression was assumed:

$$\Delta E = A + B X_{Ni} + C X_{Ni}^2 + D X_{Ni}^3 + E X_{Ni}^4 \qquad (6.4)$$

This expression was fitted to data on ΔE vs X_{Ni} reported by Weiss[70], giving A=-820, B=668.85, C=-11107.9, and D=62030 for $X_{Ni}<0.29$, and A=-1.07×10^5, B=1.28×10^6, C=-5.71×10^6, D=1.11×10^7, and E=-8.03×10^6 for $0.29<X_{Ni}<0.45$. Having established the compositional dependence of ΔE, the lattice parameter α_{FCC} in the Fe-Ni system is found to be:

$$\alpha_{FCC} = 3.54\left[1 - \lambda_1 X_{Ni} + \frac{\lambda_2 (1 - X_{Ni})}{1+g/1.79}\right] \quad \text{for } X_{Ni} < 0.29 \qquad (6.5a)$$

$$a_{FCC} = 3.64\left[1 - \lambda_1' X_{Ni} - \frac{\lambda_2' (1 - X_{Ni})}{1 + g}\right] \quad \text{for } X_{Ni} > 0.29 \qquad (6.5b)$$

with $g=\exp(\Delta E/RT)$ and $\lambda_1=0.0075$, $\lambda_2=0.0293$, $\lambda_1'=0.0338$, and $\lambda_2'=0.0273$. ΔE is given by eq(6.4). Fig.6.2 presents the lattice parameter α_{FCC} as a function of mole fraction Ni in the Fe-Ni system for $X_{Ni}<0.29$ (Fig.6.2a) and $0.29<X_{Ni}<0.5$ (Fig.6.2b). Stabilization of the high-volume ferromagnetic γ_2 state with the addition of Ni, as depicted in Fig.6.2b, results in an increase in the lattice parameter in the composition range X_{Ni}=0.30 to 0.40. However, with further addition of Ni, the γ_2 state becomes saturated and the effect of the low-volume Ni becomes evident in reducing the lattice parameter above X_{Ni}=0.40. The data presented here for the lattice parameter of the Fe-Ni system are in very good agreement with experimental data obtained by Ruhl[73].

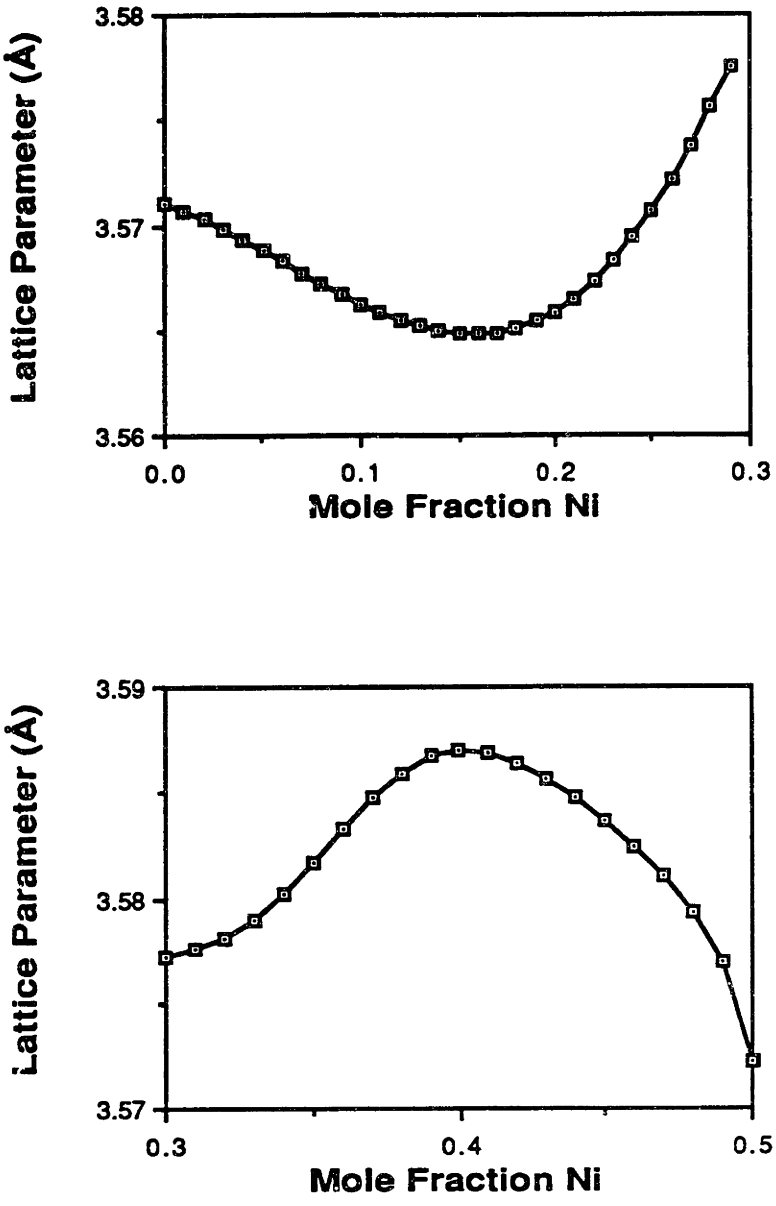

Fig.6.2 Lattice parameter α_{FCC} in the Fe-Ni system for $X_{Ni}<0.29$ in(a) and $X_{Ni}>0.29$ in (b).

Effect of Chromium

Addition of Cr markedly reduces the saturation magnetization[74], which results in a decrease in the lattice parameter irrespective of Ni content. However, Cr stabilizes the γ_2 high-volume state and, therefore, the transition from γ_1 to γ_2 occurs at lower Ni contents ($X_{Ni}<0.29$). The data of Miodownik[74] for ΔE vs X_{Cr} in the Fe-Ni-Cr system were fitted to an expression of the form:

$$\Delta E = A' + B' X_{Cr} + C' X_{Cr}^2$$

yielding $A'=50$, $B'=9180$, and $C'=-50800$, while ΔE is in cal/mol. Then, with Vegard's law, the lattice parameter α_{FCC} in the Fe-Ni-Cr system becomes:

$$\alpha_{FCC} = 3.64 \left[1 - \lambda_1' X_{Ni} - X_{Cr} + \frac{\lambda_2' (1 - X_{Ni} - X_{Cr})}{1 + \frac{g_1}{g_0} \exp(-\Delta E/RT)} \right] + X_{Cr} \left[C_1 - C_2 (X_{Ni} - C_3)^2 + C_4 (X_{Ni} - C_3)^4 \right] \quad (6.6)$$

Eq(6.6) was fitted to experimental data of Pearson[75] for lattice parameters in the Fe-Ni-Cr system to give $C_1=3.433$, $C_2=2.838$, $C_3=0.506$, and $C_4=-162.605$.

Effect of Cobalt

The effect of Co on the lattice parameter α_{FCC} will now be examined. Co stabilizes the γ_2 high-volume state as Fig.6.1 indicates. It also increases the saturation magnetic moment, which should lead to larger lattice parameters. From Fig.6.1 $\Delta E=0$ at $X_{Co}=0.4$ in the Fe-Co system. Since the ΔE vs X curves in

Fig.6.1 have similar shapes for Co and Ni, the ΔE vs X_{Cr} curve can be derived from the ΔE vs X_{Ni} curve by substituting $X_{Ni}=X_{Co}(0.29/0.40)$ in eq(6.4). The result is:

$$\Delta E = A'' + B'' X_{Co} + C'' X_{Co}^2 + D'' X_{Co}^3 \qquad (6.7)$$

where A''=-820, B''=594.5, C''=-8053.2, and D''=44971.7. Eq(6.7) then represents the effect of Co on the relative stability between the γ_1 and γ_2 states. The magnetic moment (in Bohr magnetons) was calculated for the FCC phase in the Fe-Ni-Co-Cr system using the following equation:

$$B = \sum_i X_i B(FCC, i, 0) + \sum_{i \neq j} \sum X_i X_j \left[B(FCC,i,j;0) + (X_i - X_j) B(FCC,i,j;1) + (X_i - X_j)^2 B(FCC,i,j;2) + \ldots \right]$$

where i=Co,Cr,Fe,Ni, and B(FCC,i,j) are defined in the THERMOCALC database and their values are given in Table 6.2.

Table 6.2 Coefficients B(FCC,i,j) in Bohr magnetons for the magnetic moments defined in the THERMOCALC database.

Magnetic Moment	Value
B(FCC,Fe;0)	-2.1
B(FCC,Ni;0)	0.52
B(FCC,Co;0)	1.35
B(FCC,Cr;0)	-2.1
B(FCC,Fe,Ni;0)	9.55
B(FCC,Fe,Ni;1)	7.23
B(FCC,Fe,Ni;2)	5.93
B(FCC,Fe,Ni;3)	6.18
B(FCC,Co,Fe;0)	9.74
B(FCC,Co,Fe;1)	-3.51
B(FCC,Co,Ni;0)	1.04
B(FCC,Co,Ni;1)	0.16
B(FCC,Cr,Ni;0)	-1.91

Fig.6.3 shows the variation of the magnetic moment with Ni content for the Fe-Ni ,Fe-Ni-5Co, and Fe-Ni-5Cr systems evaluated using eq(6.8). The contribution of the magnetic moment to the lattice parameter of Fe-Ni-Cr can now be calculated with the aid of eq(6.6). For X_{Ni}=0.4 and X_{Cr}=0.05 this equation gives α_{FCC} =3.5775Å, while excluding the last term in brackets (eq.6.6) from the calculation (representing the effect of the magnetic moment) gives α_{FCC} =3.5924Å. Therefore, the addition of 5% Cr reduces the lattice parameter by $\Delta\alpha$=0.01495Å. This reduction in the lattice parameter is due to a reduction in the magnetic moment ΔB caused by the addition of 5% Cr. The value of ΔB is 0.35 from Fig.6.3 for X_{Ni}=0.40. Therefore, $\Delta\alpha$=(0.01495/0.35)ΔB or $\Delta\alpha$=0.04271 ΔB, where $\Delta\alpha$ is in Å and ΔB is in Bohr magnetons. To find the corresponding effect of Co, The value of ΔB at XNi=0.40 was evaluated from the curves for Fe-Ni and Fe-Ni-5Co of Fig.6.3. This gave ΔB=0.1. Assuming the relation between $\Delta\alpha$ and ΔB above to hold for Co as well, we obtain $\Delta\alpha$=0.04271x(0.1/0.05) X_{Co} or $\Delta\alpha$=0.08542 X_{Co}. This equation represents the effect of the magnetic moment on the lattice parameter due to addition of Co.

Taking all the above into consideration, the lattice parameter α_{FCC} for the Fe-Ni-Cr-Co system is given by Vegard's law (and using eq(6.6)) as:

$$\alpha_{FCC} = 3.514\, X_{Ni} + 3.544\, X_{Co} + X_{Fe}\left[f_{\gamma_1}\, \alpha_{\gamma_1} + f_{\gamma_2}\, \alpha_{\gamma_2} \right] + X_{Cr}\left[C_1 - C_2 (X_{Ni} - C_3)^2 + C_4 (X_{Ni} - C_3)^4 \right] + 0.08542\, X_{Co} \qquad (6.8)$$

Then using eq(6.2) to express $f_{\gamma 1}$ and $f_{\gamma 2}$, we obtain:

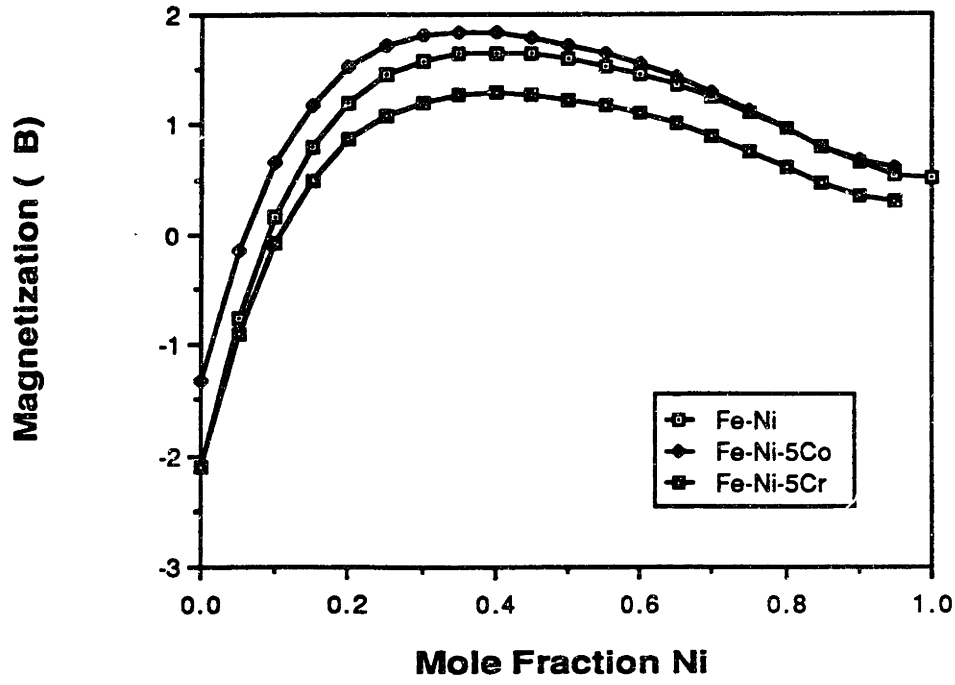

Fig.6.3 Effect of Ni on the magnetic moment of Fe-Ni, Fe-Ni-5Co, and Fe-Ni-5Cr systems evaluated using the THERMOCALC database.

$$\alpha_{FCC} = 3.514X_{Ni} + 3.544X_{Co} + 3.64\left[(1-X_{Ni}-X_{Co}-X_{Cr})\frac{0.02747(1-X_{Ni}-X_{Cr}-X_{Co})}{1+\frac{g_0}{g_1}\exp(\Delta E/RT)}\right]$$

$$+ X_{Cr}\left[C_1 - C_2(X_{Ni} - C_3)^2 + C_4(X_{Ni} - C_3)^4\right] + 0.08542\,X_{Co} \qquad (6.9)$$

ΔE in eq(6.9) is given by summing the contributions of Ni,Cr, and Co:

$$\Delta E = A+BX_{Ni}+CX_{Ni}^2+DX_{Ni}^3+B'X_{Cr}+C'X_{Cr}^2+B''X_{Co}+C''X_{Co}^2+D''X_{Co}^3$$

where the coefficients have been defined above. Eq(6.9) is the final equation to be used for the evaluation of the lattice parameter α_{FCC} in the Fe-Ni-Cr-Co system.

The value of the lattice parameter for the product phase BCC, α_{BCC}, is calculated using Vegard's law:

$$\alpha_{BCC} = \alpha_{Fe}X_{Fe} + \alpha_{Ni}X_{Ni} + \alpha_{Cr}X_{Cr} \qquad (6.10)$$

where α_{Cr}=2.8846Å for BCC Cr from Barrett and Massalski [76]. Experimental data from Ruhl[73] on the Fe-Ni BCC lattice parameters can be used to further develop eq(6.10). These data are presented on Fig.6.4. Ruhl has obtained data for Ni contents up to 30 atomic percent. For higher Ni contents of interest in this work, a straight line between the data points for 22 and 30 atomic percent Ni in Fig.6.4 will be adopted to represent the compositional dependence of the lattice parameter for Ni content higher than 25 atomic percent. The equation for this line is:

$$\alpha_{BCC}\,(Fe\text{-}Ni) = 2.8664 - 0.11\,(X_{Ni} - 0.25)\,,\ \text{for } X_{Ni} > 0.25$$

Eq.(6.10) then becomes:

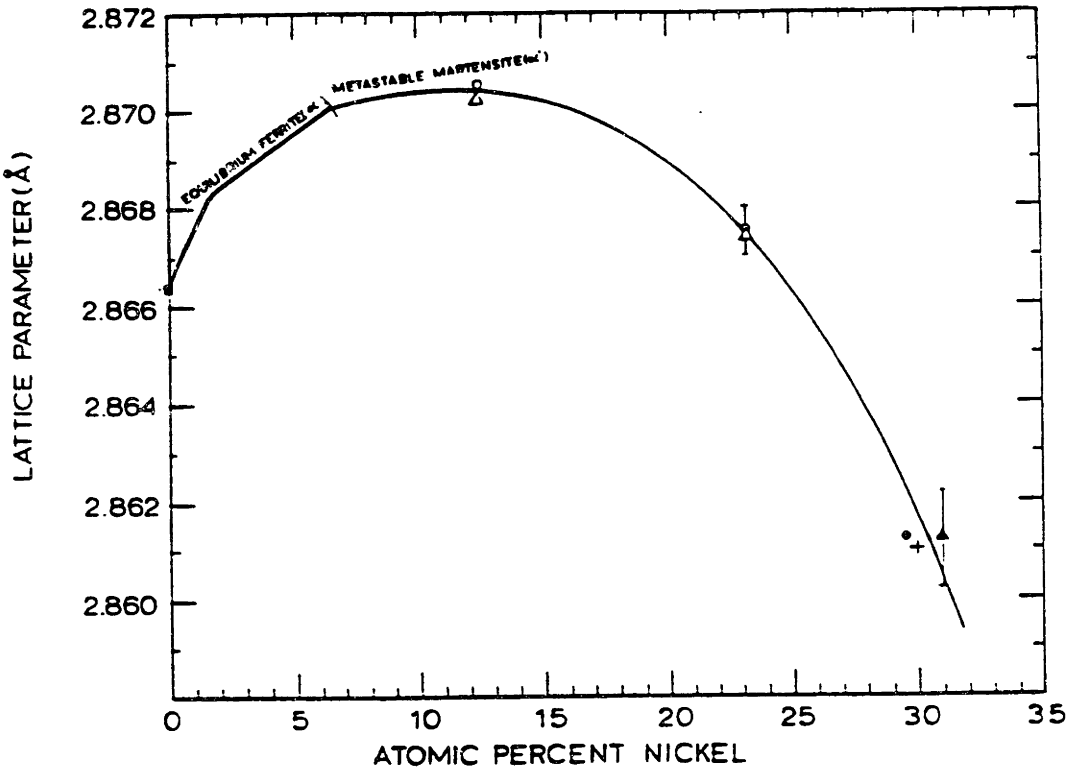

Fig.6.4 Fe-Ni BCC lattice parameters (from reference 71).

$$\alpha_{BCC} = [\ 2.8664 - 0.11\ (X_{Ni} - 0.25)\ ]\ (1 - X_{Cr}) + 2.8846\ X_{Cr} \qquad (6.11)$$

Eq.(6.11) gives the lattice parameter of Fe-Ni-Cr BCC system for $X_{Ni} > 0.25$. The effect of Co was not taken into account because of the lack of information on the lattice parameter of Fe-Co BCC solid solutions.

Eq(6.1),(6.9), and(6.11) are then used to evaluate the volume change $\Delta V/V$ as a function of composition.

6.5 Austenite Stabilization at Higher-Strength Levels.

The toughening effects discussed in Chapter 5 were associated with AF1410 steel with strength in the range 45 to 50 Rc. An attempt will be made now to design alloy compositions for transformation toughening in the 50-55 Rc range corresponding to 1700-2100 MPa in tensile strength . The additional mechanical driving force at these higher strengths must be compensated by a corresponding chemical stabilization of the precipitated austenite to ensure similar toughening effects as for AF1410 steel.

The increment in the mechanical driving force $\Delta(\Delta G^{\sigma})$ due to an increment in stress $\Delta\sigma$, can be calculated using the Patel-Cohen criterion as:

$$\Delta\ (\ \Delta G^{\sigma}\ ) = (\ \Delta\sigma\ )\ (\ \frac{\partial \Delta G^{\sigma}}{\partial \sigma}\ )$$

For the crack-tip stress-state, $\partial\Delta G/\partial\sigma$=1.42 J/mol.MPa. So for $\Delta\sigma$=400 MPa, $\Delta(\Delta G^{\sigma})$=568 J/mol. The free energy change for the martensitic transformation evaluated at room temperature for equilibrium austenite precipitated at a tempering temperature of 510°C will be adopted as a measure of stability. This quantity was calculated using the THERMOCALC software with a procedure described in section 5.2.2.2. For AF1410 steel (14Co-10Ni matrix) the free energy change is ΔG_{ch}=813J/mol. Therefore, in order to compensate for the increment in the mechanical driving force calculated above, the free energy

change must increase to 1380J/mol. The quantity ΔGch was calculated for several alloy compositions, and the results are listed in Table 6.3. The compositions of equilibrium austenite are also shown in Table 6.3. As was mentioned earlier, the selection of alloy compositions is subject to the constraint of a large volume change. Therefore, the transformational volume change was calculated for each of the alloys listed in Table 6.3. with the aid of eq(6.1),(6.9), and (6.11) of the previous section. Several of the alloys in Table 6.3 contain Cr. It is important to note that this is the Cr remaining in solution after complete precipitation of M_2C carbides at 510°C. The alloy compositions in Table 6.3 are therefore matrix compositions. The alloy composition in Table 6.3 that satisfies the stability requirement of 1380J/mol is Fe-14Co-15Ni-2Cr (in wt%) which possesses a ΔGch=1427J/mol and ΔV/V=3.3%. Both, the stability and the volume change are much higher than the corresponding values for the reference Fe-14Co-10Ni matrix. It, therefore, represents the alloy matrix composition with the best combination of austenite stability and transformation volume change for enhanced transformation toughening at higher strength levels.

Table 6.3 Dependence of austenite stability and transformation volume change on alloy matrix compositions (wt%).

Alloy	**Austenite Composition (783K)**			**ΔGch(300K)**	**ΔV/V(%)**
(Co-Ni-Cr)	Ni	Co	Cr		
14-10	0.41	0.032	0	813 J/mol	2.20
16-15	0.43	0.045	0	1300	2.24
14-15-2	0.39	0.044	0.043	1427	3.30
14-13-3	0.37	0.044	0.067	1115	4.1
13-13-3	0.37	0.04	0.066	1045	3.88

7. SUMMARIZING DISCUSSION

7.1 General

The remarkable mechanical behavior associated with transformation plasticity in the metastable fully-austenitic steels has been exploited in this thesis for ultrahigh-strength martensitic steels containing dispersed metastable austenite. The dispersed austenite is found either as retained austenite or precipitated austenite.

Transformation toughening is a toughening mechanism that arises from the interaction between the transformation plasticity of dispersed austenite with fracture-controlling processes. In the ultrahigh-strength steels of improved cleanliness, fracture is controlled by shear instability, which leads to a zig-zag fracture path ahead of a mode I crack tip. The pressure dependence of the shear instability strain in pure shear experiments suggests a void-softening mechanism of shear instability [77]. Models for void nucleation [78-80] indicate that the critical nucleation stress or strain depend on both the characteristics of the void-nucleating particle dispersion (size, volume fraction, particle spacing, interfacial strength) as well as the strain-hardening behavior of the matrix. Toughness improvements can be anticipated by controlling the strain-softening mechanisms which trigger the instability, e.g. by dissolving the void-nucleating particles with high-temperature austenitizing[81,82]. On the other hand, shear instabilities can be delayed by superimposing a controlled strain-hardening contribution at the critical point of instability. For this to happen, a *redistribution* of strain hardening along the stress-strain curve of the material must occur. So far, the most promising mechanism for altering the constitutive behavior of the matrix is transformation plasticity. It was discussed in chapter 2

that when the transformation is strain-induced, transformation and slip act as parallel deformation mechanisms, which result in a distortion of the stress-strain curve towards the ideal exponential hardening behavior that imparts maximum flow stability. These *curve-shaping* effects of transformation plasticity delay shear instabilities and therefore improve toughness. Furthermore, the volume change due to the transformation relieves the general stress triaxiality ahead of the crack tip, and may locally interact at particle interfaces to delay the microvoid nucleation processes driving instability, and this in turn lowers the critical strain-hardening rate for void-induced instability.

The interaction between transformation plasticity and shear instability as described above provides a framework under which transformation toughening operates assuming that the dispersed austenite has optimum stability. The austenite should transform only ahead of a crack-tip and at the latest stages of deformation in order to inhibit the localization of plastic flow. Therefore, the required stability for transformation toughening is quite high. Preferably, the austenite should not transform in a tensile test or even in a plane-strain tension test.

The stability of dispersed austenite is of central importance for transformation toughening and as such it was emphasized in this research. The parameters which control the stability of dispersed austenite have been identified. The most important are the size and the chemical composition of the austenitic particles as well as the stress state. Accordingly, heat treatments have been developed aiming at size refinement and compositional enrichment of the dispersed austenite in order to stabilize it for the crack-tip stress state. One of these treatments, called the "direct-nucleation" treatment, results in the precipitation of very fine intralath austenite, highly enriched in Ni. This treatment significantly enhances the fracture toughness relative to the standard treatment

and with no loss of hardness. The technological importance of dispersed-phase transformation toughening is thus demonstrated.

7.2 On Retained Austenite.

The transformation plasticity effects associated with retained austenite have been studied in 4340 steel. The stability of retained austenite was characterized quantitatively as a function of stress state. For this purpose the M_S^{σ} temperature is used as a measure of stability. Table 3.2 shows how the stability of retained austenite varies with stress state. While the retained austenite is relatively stable for the pure shear stress state, it is quite unstable for the crack-tip stress state. This is because M_S^{σ}(p.s) is just below room temperature while M_S^{σ}(c) is much higher than room temperature. The thin-wall torsion experiments demonstrate that the strain-induced transformation of retained austenite delays shear instability. This flow-stabilizing effect of retained austenite is consisted with its stability for the pure shear stress-state. Room temperature K_{IC} fracture toughness tests do not indicate similar interactions that could enhance toughness, since the retained austenite is unstable for the crack-tip stress state.

For stress-assisted transformation, yielding is controlled by the transformation, and therefore, the flow stress decreases with decreasing temperature as indicated in Fig.2.1. While this phenomenon is clearly evident in TRIP steels, it is not observed for retained austenite dispersed in the martensitic matrix. This is shown in Fig.3.1 which indicates that the 0.2% flow stress does not undergo a reversal at the M_S^{σ} temperature. Only a plateau region is observed around the M_S^{σ} temperature, suggesting that there could be a reversal if larger amounts of retained austenite were present. This idea is supported by the fact that even the plateau region disappears when the volume

fraction of retained austenite drops from 9% to 4%. Another contribution to the observed behavior is that, at lower temperatures, the chemical driving force becomes increasingly important relative to the mechanical driving force in their contributions to the critical driving force for the martensitic transformation. The transformation nucleates at lower stresses as the temperature decreases. The microyielding experiments indicate that the elastic limit is completely controlled by the transformation and decreases with decreasing temperature. Therefore, most of the retained austenite transforms in the microyielding region, before reaching the 0.2% flow stress, as the temperature decreases.

Modelling of the stress-strain behavior in the microyielding region at $T<M_S^{\sigma}$, shows that the elastic limit depends on the degree of carbon enrichment of the retained austenite resulting from the segregation of carbon to the austenite during tempering. The carbon enrichment decreases the chemical driving force for the transformation, and also increases the frictional work of interfacial motion due to solid solution hardening of the austenite. The combination of these two effects requires that additional driving force has to be supplied for the transformation to continue. In the microyielding experiments, this additional driving force is supplied by the applied stress and, therefore, the elastic limit is determined by the degree of carbon enrichment.

7.3 On Precipitated Austenite

It has been demonstrated that retained austenite may be too unstable for transformation toughening. Furthermore, the stability of retained austenite is not easily controlled. However, when the dispersed austenite is in the form of precipitated austenite, then its stability can be controlled through processing. These effects have been studied in the high Ni-Co martensitic steels. A functional form was developed relating the M_S^{σ} temperature with stability

parameters such as size and composition of the austenite particles, the yield strength of the matrix, and the stress state:

$$M_s^{\sigma} = M_s^{\sigma} (\sigma_y , \sigma_h / \bar{\sigma} , V_P , \text{wt\% Ni})$$

Then the size and compositional-enrichment requirements for optimum crack-tip stability of the dispersed austenite were estimated. Following this, a number of treatments were investigated to achieve the desired austenitic dispersions. It was found that in addition to stability, the amount and distribution of the austenite are also important factors controlling the transformation toughening.

Single tempering treatments in the high Ni-Co martensitic steels produce mainly interlath austenitic films. In terms of distribution, this austenitic dispersion is not uniform since no austenite precipitates in the interior of the martensitic laths. With short tempering times these austenitic films are relatively stable, but at longer times they lose stability because they link with other austenite films on the same lath boundary and, therefore, increase in size. Stabilization in this case can occur only after very long tempering times, so that the Ni enrichment in the austenite can reach the equilibrium composition, which is high enough to stabilize the austenite. However, the strength then decreases rapidly with tempering time due to coarsening of the carbide dispersions. Single tempering treatments for austenite stabilization are therefore not successful in achieving good strength/toughness combinations.

Another approach to austenite stabilization considered in this work is heterogeneous nucleation of austenite on alloy-enriched cementite so that the austenite can inherit the stabilizing solutes. In a first tempering step (420°C/5h), a cementite dispersion is formed so that in a second step (510°C/8h), austenite nucleates not only on the lath boundaries but also on the cementite particles in the interior of the martensitic laths. Therefore, both interlath and intralath

austenite are thus formed. The intralath austenite is relatively fine and enriched in Ni (18 wt%), the Ni enrichment being due to solute transfer from the cementite to the austenite particles. However, the cementite particles, being stabilized by Cr, do not dissolve during the second step of the treatment and, as a result, the toughness of the steel is degraded relative to that of the single tempering treatments.

Finally, the best toughening effects are obtained with the direct-nucleation treatment, which results in an ultrafine, chemically-enriched and, therefore, very stable intralath austenitic dispersion. The treatment consists of two steps: a short-time high-temperature tempering (600°C/15min) followed by the standard temper (510°C/8h). Equilibrium high-Ni austenite nucleates during the first step of the treatment. Calculations on nucleation energetics indicate that the most feasible mode of nucleation is semicoherent nucleation on dislocations. Interactions of austenite embryos with carbides may also contribute to the nucleation process. The toughening effects associated with the precipitation of the ultrastable austenitic dispersion are noteworthy. Not only is the J_{IC} increased by 25% with no loss of strength but the tearing modulus (crack-growth resistance) is increased as well. The tensile uniform ductility is also improved compared to the single tempering treatments. However, the improvement in uniform ductility is not as dramatic as the improvement in fracture toughness, demonstrating that although the stability of precipitated austenite is optimum for the crack-tip stress state, it is too high for the tensile stress state. In terms of strength/toughness combinations, the direct-nucleation treatment represents a marked technological advance (Fig.5.24) with a K-value (Charpy energy/hardness combinations) of 170 compared to 140 for the standard treatment of the AF1410 steel used today.

The toughness improvements discussed above take place at the 48-50 Rc strength of AF1410 steel. To achieve the higher property objectives, outlined in the introduction of this thesis, the austenitic dispersion must be made still more stable due to the increased mechanical driving-force contribution at the higher strength levels. Consequently, alloy design for enhanced austenite stabilization and toughening involves two requirements: selection of alloy composition for greater chemical stabilization to compensate for the increased mechanical driving forces and large transformational volume change. The volume change can be controlled through the compositional dependence of the lattice parameters of the product BCC and parent FCC phases. The two-gamma states model has been employed to describe the magnetic effects on the lattice parameter of the FCC phase. Taking into account the effect of alloying elements on the relative stabilities of the γ_1(low-volume) and γ_2(high-volume) states as well as on the overall magnetic moment, the lattice parameter of austenite can be formulated as a function of composition. This, together with thermodynamic calculations on chemical stabilization, allow the design of an alloy with a superior combination of austenite stability and transformation volume change for enhanced transformation toughening.

8. CONCLUSIONS

The results presented in this thesis lead to the following conclusions with regard to dispersed-phase transformation toughening in ultrahigh-strength steels:

(1) The transformation plasticity of dispersed austenite and the associated toughening effects are controlled by the stability of the austenitic dispersion. While the stability of retained austenite cannot be adequately controlled, the stability of precipitated austenite can be optimized through alloy design and heat treatment.

(2) The most important microstructural parameters which control the stability of dispersed austenite are the size and the chemical composition of the austenitic particles. The particle size affects the probability of finding a nucleation site in the particle, while the composition governs the chemical driving force for the martensitic transformation. The stability depends also on the stress state through the interaction of the transformational volume change with stress triaxiality. For significant transformation toughening, the required stability of the austenitic dispersion is quite high, and can be achieved only by size refinement and compositional enrichment of the austenitic particles.

(3) The M_S^{σ} temperature provides a single-parameter characterization of the stability of dispersed austenite. It was measured as a function of stress state for retained austenite in 4340 steel. The results indicate that while this retained austenite is stable for the pure-shear stress state, it is quite unstable for the crack-tip stress state and, therefore, retained austenite had little effect on transformation toughening in this steel.

(4) Controlled experiments, designed to isolate the role of retained austenite in 4340 steel, demonstrate a flow-stabilizing effect in pure shear deformation. The delay in shear instability is attributed to the strain-induced transformation of retained austenite.

(5) While the 0.2% macroscopic flow stress in 4340 steel is found not to be controlled by retained-austenite transformation in the stress-assisted regime, unlike the metastable fully-austenitic steels, microyielding experiments demonstrate that the elastic limit is completely *transformation-controlled* for $T<M_S^{\sigma}$ and *slip-controlled* for $T>M_S^{\sigma}$.

(6) The constitutive behavior in the stress-assisted microyielding regime of 4340 steel has been modelled successfully by considering the effect of stress on the autocatalytic nucleation-site potency distribution. For retained austenite, the distribution is truncated due to the activation of sites during quenching. This procedure allows an estimation of the carbon stabilization of the retained austenite during tempering. The carbon enrichment decreases the chemical driving force and increases the frictional work of interfacial motion. Therefore, for transformation to

continue, the above effects have to be compensated by supplying a mechanical driving force, which then determines the elastic limit (transformation stress) of the steel.

(7) Three types of tempering treatments aiming at austenite stabilization have been studied in AF1410 steel:

(a) Single tempering treatments (510C for 5 or 8h) result in precipitation of interlath austenite with non-uniform distribution. This austenite is not significantly stable for transformation toughening effects.

(b) Austenite nucleation on alloy-enriched cementite results in the formation of an intralath austenite dispersion with significant Ni enrichment. The cementite is precipitated and alloy-enriched during the first step (420°C/5h) of the treatment, while the dispersed austenite forms during the second step (510°C/8h). Despite the resulting austenite stabilization, the presence of undissolved cementite proves deleterious to the fracture toughness.

(c) A direct-nucleation treatment consisting of short-time high-temperature (600°C/15min) tempering, followed by the standard tempering treatment (510°C/8h), results in the nucleation of dispersed equilibrium austenite. This dispersion is uniformly distributed, ultrafine (~200Å), and highly-enriched in Ni (~30wt%). These characteristics re[illegible] the austenitic dispersion stable enough for the crack-tip stress state and, hence, for transformation toughening.

(8) The direct-nucleation treatment results in a 25% increase in fracture toughness at no loss of hardness compared to the standard single treatments. This finding represents a pronounced technological advance and underlines the potential importance of transformation toughening for this class of ultrahigh-strength martensitic steels.

(9) Even greater dispersed-phase transformation toughening at ultrahigh strength levels is potentially attainable by enhanced austenite stabilization and a large transformation volume change. Thermodynamic calculation of austenite stability and a formulation of the compositional dependence of lattice parameters, taking into account magnetic effects in the austenite, permit the design of alloy compositions with superior combinations of austenite stability and transformation volume change for enhanced transformation toughening.

9. SUGGESTIONS FOR FUTURE RESEARCH

(1) The temperature dependence of the strength-differential effect, based on the 0.2% flow stresses in tension and compression, exhibit two local minima at the tensile and compressive M_S^{σ} temperatures respectively. This behavior should be compared with the temperature dependence of the strength-differential effect, based on the tensile and compressive elastic limits.

(2) Although the high fracture toughness of the direct-nucleation treatment in AF1410 steel is attributable to the transformation toughening of the ultrafine and chemically-enriched austenitic dispersion, a rigorous proof requires measurement of the temperature dependence of J_{IC} in order to vary the stability of the precipitated austenite. A peak toughness should be observed near $M_S^{\sigma}(c)$ where the stability of the austenite is optimum for crack-tip interaction that leads to transformation toughening.

(3) The role of carbides on the nucleation of austenite during the first step (600°C/15min) of the direct-nucleation treatment should be studied experimentally by applying the treatment to a carbon-free Fe-14Co-10Ni ternary alloy. This experiment will give insight to the mode of austenite nucleation and whether carbide interactions are important.

(4) The cementite-nucleated austenite treatment should be explored further in Cr-free steels where the cementite should be easier to dissolve on tempering and , therefore, not interfere with transformation toughening as void-nucleating particles. At the same time, the observation in this work of multiple austenite nucleation on a single cementite particle implies a possible role of the transformation of austenite on void nucleation. More detailed TEM observations in fractured specimens are needed to assess the role of dispersed austenite and its transformation as an inhibitor of void nucleation.

(5) Enhanced transformation toughening at extremely high strength levels requires higher stability of the precipitated austenite and a large transformation volume change. The next upgrading of AF1410 suggested in this work is an Fe-14Co-15Ni-2Cr matrix composition that appears to have the optimum combination of austenite stability and volume change at the 55 Rc hardness level. Further modifications could involve substitution of Co by Al for dislocation-recovery resistance and substitution of Ni by Mn as an austenite stabilizer. The reason for the proposed replacement of Ni is the tendency toward intermetallic-compound formation between Ni and Al. In addition, Mn stabilizes the low-volume antiferromagnetic state in the austenite and therefore reduces the austenitic lattice parameter. This results in a larger volume change and should enhance toughening. Higher carbon contents should also be investigated as means of enhancing austenite stability.

(6) The highest K-value of 240 (Charpy-energy/hardness combinations) was achieved by a variation of the direct-nucleation treatment (570°C/15min instead of 600°C/15min). It is interesting to note that relative to the standard treatment in AF1410 steel (510°C/5h), the 600°C/15min treatment increased the toughness at constant hardness while the 570°C/15min treatment increased the hardness at constant toughness. These strengthening interactions, associated probably with the effect of the 570°C temper on subsequent M_2C carbide precipitation, should be explored further.

APPENDIX A

DECONVOLUTION OF PEAKS FOR STEM MICROANALYSIS

High-resolution STEM microanalysis was used in this work to determine the chemical composition of the precipitated austenite. The main problem in the analysis of the energy-dispersive X-ray spectra was the peak overlap for Fe, Co, and Ni. Specifically, the following overlaps were observed:

peak	KeV	overlap
Fe	6.14-6.62	FeK_{α}
Co	6.66-7.22	FeK_{β} and CoK_{α}
Ni	7.26-7.74	CoK_{β} and NiK_{α}

To carry out the deconvolution of these peaks, two standard samples were prepared. A cobalt oxide sample, consisting of cobalt oxide powder supported on a grid, and a pure Fe sample. Energy-dispersive X-ray spectra were then taken in the STEM under the same operating conditions as for the regular STEM microanalysis of the precipitated austenite (100 KV operating voltage and windowless detector). From these spectra, the ratios of the K_{α} and K_{β} peaks were determined:

$$FeK_{\beta} / FeK_{\alpha} = 0.12$$

$$CoK_{\beta} / CoK_{\alpha} = 0.12$$

These ratios remain constant under the same operating conditions. Then, the net number of counts, which is the number of counts after background subtraction, served to calculate the effective number of counts after the peak deconvolution as follows:

$$D_{Co} = C_{Co} - R_{Fe} C_{Fe}$$

$$D_{Ni} = C_{Ni} - R_{Co} C_{Co}$$

where C_{Co}, C_{Ni}, C_{Fe} are the net counts, and D_{Co}, D_{Ni} are the effective number of counts that were used in the Cliff-Lorimer analysis. For Fe, $D_{Fe}=C_{Fe}$ for the K_α peak. The K-factors used in the analysis were:

$K_{Cr}=0.93$

$K_{Fe}=1.00$

$K_{Co}=1.06$

$K_{Ni}=1.07$

$K_{Mo}=3.63$

APPENDIX B

NUCLEATION OF AUSTENITE

B.1 Driving Forces.

The driving force for austenite precipitation entering the calculations of nucleation energetics was derived from the Thermocalc software. The calculations were performed for the composition of the AF1410 steel at 510 and 600°C. The results are shown in Table B1. The following cases were examined:

- precipitation of austenite from a paraequilibrium mixture of ferrite and cementite
- precipitation of austenite from an equilibrium mixture of ferrite and M_2C
- precipitation of austenite from a paraequilibrium mixture of ferrite and M_2C.

The driving forces for the precipitation of M_2C carbides were also calculated and are given in Table B.1 for comparison. The following cases were examined:

- precipitation of incoherent M_2C from ferrite
- precipitation of incoherent M_2C from a paraequilibrium mixture of ferrite and cementite
- precipitation of coherent M_2C from ferrite
- precipitation of coherent M_2C from a paraequilibrium mixture of ferrite and cementite.

The results in Table B.1 indicate that the driving forces for the precipitation of M_2C carbides are much higher than the corresponding driving forces for the precipitation of austenite. However, in the temperature range 500-600°C, the driving forces for the precipitation of austenite remain nearly constant while the driving forces for the precipitation of M_2C carbides decrease rapidly from 510 to

600°C, suggesting a trend for austenite precipitation to compete with carbide precipitation at higher temperatures.

In the following, the driving force for austenite precipitation from ferrite was used in the calculations of nucleation energetics.

Table B.1 Driving forces for precipitation of Austenite and M_2C at 510 and 600°C in AF1410 steel

Precipitation Reaction	Chemical Driving Forces (J/Mol)	
	510°C	600°C
Ferrite ⇒ Austenite	1868	1863
(Ferrite+Pcem)⇒Austenite	1621	1615
Ferrite⇒ incoh.M_2C	21765	17966
(Ferrite+Pcem)⇒ incoh. M_2C	13119	12317
Ferrite⇒ coh. M_2C	13106	11533
(Ferrite+Pcem)⇒coh. M_2C	9120	-1255
(Ferrite+M_2C)⇒ Austenite	2017	1694
(Ferrite+M_2C)paraeq.⇒ Austenite	1962	1613

Note: Pcem=Cementite in paraequilibrium with Ferrite

B.2 Homogeneous nucleation.

B.2.1 Coherent austenite.

The total free-energy change for homogeneous nucleation of austenite is:

$$\Delta G = \Delta G_{Ch} + \Delta G_E + \Delta G_S$$

where ΔG_{Ch} is the chemical driving force for the precipitation of austenite, ΔG_E is the elastic strain energy, and ΔG_S is the surface energy associated with the formation of the embryo. For a spherical particle in an elastic isotropic medium, the strain energy per unit volume is [83]:

$$\Delta G_E = \frac{2\mu}{15(1-\nu)}\left[4\,(\varepsilon_{11}^2 + \varepsilon_{22}^2 + \varepsilon_{33}^2) + 5\,(\nu+1)\,(\varepsilon_{11}\varepsilon_{22} + \varepsilon_{22}\varepsilon_{33} + \varepsilon_{33}\varepsilon_{11}) \right] \qquad \text{(B.1)}$$

where μ is the shear modulus, ν is the Poisson's ratio, and $\varepsilon_{11}, \varepsilon_{22}, \varepsilon_{33}$ are the principal strains of the Bain tensor describing the transformation from BCC to FCC. The Bain distortion is tetragonal with strain components as follows:

$$\varepsilon_{11} = \frac{\alpha_{FCC}}{\alpha_{BCC}} - 1 \quad \text{and} \quad \varepsilon_{22} = \varepsilon_{33} = \frac{\alpha_{FCC}}{\sqrt{2}\ \alpha_{BCC}} - 1 \qquad \text{(B.2)}$$

where α_{FCC} and α_{BCC} are the lattice parameters of the austenite and ferrite respectively. Taking α_{FCC}=3.57Å and α_{BCC}=2.86Å we get:

$$\varepsilon = \begin{bmatrix} 0.248 & 0 & 0 \\ 0 & -0.0885 & 0 \\ 0 & 0 & -0.0885 \end{bmatrix} \qquad \text{(B.3)}$$

Inserting these values in eq(B1) for the strain energy, gives ΔG_E=1.07GJ/m^3. Using V_m=6.85x10^{-6}m^3/mol for the molar volume of the austenite, the above value corresponds to ΔG_E=7.32 KJ/mol. This value is prohibitively large for homogeneous nucleation of coherent austenite to occur under the available driving forces listed in Table B.1.

B.2.2 Semicoherent austenite.

The total free-energy change for the nucleation of a spherical particle is

$$\Delta G = \frac{4}{3}\pi r^3 \left(\Delta G_v + \Delta G_{str} \right) + 4\pi r^2 \gamma_{sem} \qquad (B.4)$$

where γ_{sem} is the interfacial energy associated with a semicoherent interface, ΔG_{str} is the strain energy associated with the size misfit of the austenitic nucleus in the ferritic matrix, and r is the radius of the forming nucleus.

The interfacial energy of a semicoherent nucleus is:

$$\gamma_{sem} = \gamma_{coh} + \gamma_{str}$$

where γ_{coh} is the interfacial energy of a coherent interface (the chemical term) and γ_{str} is a structural term due to the dislocation array that makes up the interfacial boundary. An estimate for γ_{str} is

$$\gamma_{str} = \frac{\delta}{\alpha_{FCC}} \frac{\mu b^2}{2} \qquad (B.5)$$

with δ being:

$$\delta = \frac{\alpha_{FCC} - \alpha_{BCC}}{\alpha_{FCC}} \qquad (B.6)$$

Taking α_{FCC} and α_{BCC} from above gives δ=0.198 With these values and taking γ_{coh} to lie in the range of 10-20 ergs/cm^2 (mJ/m^2), the interfacial energy for a semicoherent nucleus becomes γ_{sem}=184 to 194 ergs/cm^2.

The strain energy ΔG_{str} associated with the size misfit can be evaluated using the treatment by Nabarro[84] and Christian[85] for a spherical inclusion. The strain energy per unit volume is:

$$\Delta G_{str} = \frac{2}{3} \mu^{\alpha} C_6 \left(\frac{\Delta V}{V} \right)^2 \tag{B.7}$$

where $\Delta V = V_{\gamma} - V_{\alpha}$, V_{γ} and V_{α} are the molar volumes of austenite and ferrite respectively The parameter C_6 is given by:

$$C_6 = \frac{3K^{\gamma}}{3K^{\gamma} + 4\mu^{\alpha}} \tag{B.8}$$

where K is the bulk modulus and μ is the shear modulus. C_6 is a measure of the extent to which the matrix is able to accomodate the volume change, and therefore it is termed the as the accomodation factor. The molar volumes are:

$$V_{\gamma} = \frac{N_{AV}}{4} \alpha_{FCC}^3 = 6.85 \times 10^{-6} \text{ m}^3 / \text{mol}$$

$$V_{\alpha} = \frac{N_{AV}}{2} \alpha_{BCC}^3 = 7.28 \times 10^{-6} \text{ m}^3 / \text{mol} \tag{B.9}$$

For these values, eq(B7) gives $\Delta G_{str} = 107$ MJ/m^3.

Taking $\Delta G_V = -272$ MJ/m^3, we obtain the activation barrier and the critical radius as:

$$\Delta G^{*} = \frac{16 \pi \gamma_{sem}^3}{3 \left(\Delta G_v + \Delta G_{str} \right)^2} = 3.5 \times 10^{-18} \text{ J}$$

$$r^{*} = - \frac{2 \gamma_{sem}}{\left(\Delta G_v + \Delta G_{str} \right)} = 21 \text{ Å} \tag{B.10}$$

The activation barrier above corresponds to $\Delta G^{*} = 22$ eV which is a very large barrier to be surmounted by thermal activation.

B.3 Heterogeneous Nucleation on Dislocations

B.3.1 Coherent Nucleation on Edge Dislocations

The problem of formation of coherent embryos near an edge dislocation has been studied by Lyubov[86] and Dollins[87]. Recently Larche[88] used the method of Eshelby[89,90] to calculate the interaction energy between the precipitate and the stress-field of the dislocation. Matrix and embryo are assumed to have the same elastic coefficients.

The total free-energy change is given by the sum of the chemical driving force ΔG_{ch},the elastic strain energy ΔG_E, the surface energy ΔG_S, and the interaction energy ΔG_I as:

$$\Delta G = \Delta G_{ch} + \Delta G_E + \Delta G_S + \Delta G_I$$

The interaction energy is given by:

$$\Delta G_I = - \int_V \sigma_{ij}^D \varepsilon_{ij}^T \, dV \tag{B.11}$$

where σ_{ij}^D describes the stress field of a dislocation in an infinite homogeneous isotropic medium and ε_{ij}^T is the stress-free transformation strain. Larche[84] considered a pure dilatational transformation and the interaction with an edge dislocation, and defined two parameters β and A as follows:

$$-\beta = \Delta G_v + \Delta G_E \tag{B.12}$$

$$-A = \frac{\mu b}{3\pi} \frac{1+\nu}{1-\nu} e^T \tag{B.13}$$

In the case of austenite nucleation, ΔG_E also posseses a large deviatoric component. Therefore, the value of ΔG_E from eq(B2) is used. Substituting the values of the parameters in the equations above we get:

$\beta<0$, $A<0$, and $|A|-2\gamma>0$, and the free-energy change vs r curve has a minimum at $r^* = (-2\gamma-A) / \beta$. Therefore, a stable cylinder, of radius r^*, can form but cannot grow with further reduction of the free energy of the system. The size of the stable cylinder is $r^*=10$Å for $\gamma=10 mJ/m^2$ and $r^*=8$Å for $\gamma=20 mJ/m^2$.

B.3.2 Semicoherent Nucleation on Edge Dislocations

A semicoherent nucleus will possess the strain energy of a misfiting particle which was calculated above to be $\Delta G_E=107$ MJ/m^3. Under these conditions, the parameters A and β for the intaraction with an edge dislocation according to the treatment by Larche outlined above are: $-\beta=\Delta G_v+\Delta G_E=-165$ MJ/m^3 ($\beta>0$), $A=355$ mJ/m^2. The surface energy of the semicoherent nucleus is found to be 174 mJ/m^2 and so $|A|-2\gamma=7 mJ/m^2$. Since $\beta>0$ and $|A|-2\gamma>0$, the nucleation is barrierless.

BIBLIOGRAPHY

1. G.B.Olson, "Mechanically-Induced Phase Transformations in Alloys", Encyclopedia of Mat.Sci.and Eng., Ed. M.B.Bever (1986) Pergamon Press, NY, pp 2929-32.

2. G.B.Olson and M.Cohen, Metall.Trans. **7A** (1976) 1897.

3 M.Cohen and G.B.Olson, "Martensitic Nucleation and the Role of the Nucleating Defect", in *New Aspects of Martensitic Transformations* , First JIM International Symposium (JIMIS-1) Kobe, Japan. Suppl. Trans. JIM **17** (1976) 93.

4. R.E.Cech and D.Turnbull, Trans. AIME , **206** (1956) 124.

5. J.R.Patel and Morris Cohen, Acta Metall. **1** (1953) 531.

6. G.B.Olson, K.Tsuzaki, and M.Cohen, "Statistical Aspects of Martensitic Nucleation", in Turnbull Symposium : *Phase Transformations in Condensed Systems* ed. G.S.Cargill, F.Spaepen, and K.N.Tu, MRS, in press.

7. I-W Chen and P. Reyes, J. Am. Ceram. Soc., **69**, No.3, (1986), 181

8. Y.Kuroda, "Kinetics of Deformation-Induced Transformation of Dispersed Austenite In Two Alloy Systems", S.M.Thesis, MIT, June 1987.

9. M.Kato. R.Monzen, and T.Mori, Acta Metall. **26** (1978) 605

10. A.K.Sachdev, Acta Metall. **31** (1983) 2037

11. T.Narutani, G.B.Olson, and M.Cohen, Proc. Int. Conf. Mart. Transf. ICOMAT-82, Leuven, Belgium, J. de Physique **43** (1982) C4-429.

12. G.B.Olson, "Transformation Plasticity and the Stability of Plastic flow ", in *Deformation Processing and Structure* , pp. 391-424; ASM, Metals Park, OH, 1983.

13. T.Narutani, G.B.Olson, and M.Cohen, unpublished research, MIT, Cambridge, MA, 1982.

14. W.W.Gerberich, P.L.Hemmings, and V.F.Zackay, Metall.Trans. **2** (1971) 2243.

15. R.H.Leal, "*Transformation Toughening of Metastable Austenitic Steels*", Doctoral Thesis, MIT, Cambridge, MA (1984).

16. C.C.Young, "*Sharp-Crack Transformation Toughening in Phospho-Carbide Strengthened Austenitic Steels*", Doctoral Thesis, MIT, Cambridge, MA (1987).

17. A.G.Evans and R,M.Cannon, Acta Metall. **34** (1986) 761.

18. A.G.Evans and A.H.Heuer, J.Am.Cer.Soc. **63** (1980) 241.

19. B.Budianski, J.W.Hutchinson, and J.C.Lambropoulos, Int. J. Solids and Structures **19** (1983) 337.

20. S.Jin, S.K.Hwang, and J.W.Morris,Jr, Metall.Trans. **6A** (1975) 1569

21. K.Segawa, S.Nagashima, S.Sekino, and H.Shimada, Tetsu to Hagane, **49** (1963) 40

22. J.I.Kim and J.W.Morris, Jr, Metall.Trans. **12A** (1981) 1957

23. J.I.Kim, C.K.Syn, and J.W.Morris, Jr, Metall.Trans. **14A** (1983) 93

24. G.R.Speich, V.A.Demarest, and R.L.Miller, Metall.Trans.**12A** (1981) 1419

25. C.I.Garcia and A.J.DeArdo, Metall.Trans. **12A** (1981) 521.

26. G.R.Speich and A. Szrimae, Trans. TMS-AIME **245** (1969) 1063

27. M.Hillert, K.Nilson, and L.B.Torndahl, JISI **209** (1971) 49

28. G.Molinder, Acta Metall. **4** (1956) 565

29. R.W.Judd and H.W.Paxton, Trans. TMS-AIME **242** (1968) 206

30. G.R.Speich, D.S.Dabkowski, and L.F.Porter, Metall. Trans. **4A** (1973) 303.

31. C.W.Marschall, R.F.Hehemann, and A.R.Troiano, Trans. ASM **55** (1962) 135.

32. H.S.Kim, H.R.Harrison, and P.G.Winchell, Metall.Trans. **12A** (1981) 1461.

33. R.F.Hehemann, in "Mechanical Behavior of Metals and Alloys Associated with Displacive Phase Transformations", Proc. Joint US / Japan Seminar, RPI, 1979.

34. B.V.N.Rao, U.S. Patent 4, 544, 422 (1985).

35. E.R.Parker and V.F.Zackay, Engineering Fracture Mechanics, **7** (1975) 371.

36. W.E.Wood, Engineering Fracture Mechanics, **7** (1975) 219.

37. G.Y.Lai, W.E.Wood, R.A.Clark, V.F.Zackay, and E.R.Parker, Metall. Trans. **5A** (1974) 1663.

38. D.Webster, Metall. Trans. **2** (1971) 1857.

39. B.Lou and B.L.Averbach, Metall. Trans. **14A** (1983) 1899.

40. M.Sarikaya, A.K.Jhingan, and G.Thomas, Metall. Trans., **14A** (1983) 1121.

41. S.Nagashima et al., Trans. ISIJ **11** (1971) 402.

42. S.Yano, Trans. ISIJ **13** (1973) 133.

43. T.Ooka and K.Sugino, J.Jpn.Inst.Metals **30** (1966) 435.

44. M.Nikura and J.W.Morris Jr., Metall. Trans. **11A** (1980) 1401.

45. D.Hardwick, JISI **34** (1961) 414.

46. J.I.Kim and J.W.Morris Jr., Metall. Trans. **11A** (1980) 1401.

47. C.D.Little et al, General Dynamics Report AFML-TR-75-148 (1975).

48. C.D.Little and P.M.Machmeier, U.S Patent 4,076,525 (1978).

49. B.Sundman, B. Jansson, and J.O-Anderson, CALPHAD, **9** (1985) 153

50. B.D.Cullity, "*Elements of X-ray Diffraction* ", Addison-Wesley Publishing Co, Reading, Mass., (1956).

51. G.F.Bolling and R.A.Richman, Acta Metall. **18** (1970) 673.

52. H.Muir, B.L.Averbach, and Morris Cohen, Trans. ASM **47** (1954) 23.

53. Annual Book of ASTM Standards, E23, (1982).

54. Annual Book of ASTM Standards, E399: Test for Plane-Strain Fracture Toughness of Metallic Materials, (1984).

55. Annual Book of ASTM Standards, E813: J_{IC}, a Measure of Fracture Toughness, (1982).

56. P.Albrecht et al, "Tentative Test Procedures for Determining the Plane-Strain J-R Curve", Journal of Testing and Evaluation, **10** (1982)245.

57. T.Hollstein, J.B.Blauel, and B.Voss, " On the Determination of Elastic-Plastic Fracture Materials Parameters: A Comparison of Different Test Methods", in *Elastic-Plastic Test Methods: The User's Experience,* ASTM STP 856 (1984) 104.

58. D.A.Jablonski, "Computerized Single-Specimen J-R curve for Compact Tension and Three-Point Bend Specimens", in *Automated Test Methods For Fracture and Fatigue Crack Growth* , ASTM STP 877 (1985) 269.

59. F.Stavehaug, "Transformation Toughening In γ'-strengthened Metastable Austenitic Steels", Doctoral Thesis Research in progress, MIT, Cambridge, MA, (1987).

60. G.B.Olson and M.Cohen, Metall. Trans. **13A** (1982) 1907.

61. G.N.Haidemenopoulos, M.Gruijic, G.B.Olson, and Morris Cohen, " *Transformation Microyielding of Retained Austenite* ", submitted to Acta Metall. (1988)

62. S.R. Pati and Morris Cohen, Trans. AIME, **17**, (1969),189

63. M. Lin, "*Autocatalytic Kinetics of Martensitic Transformations* ", Doctoral Thesis Research in progress, MIT, Cambridge, MA, (1987).

64. S.J.Barnard, G.D.W.Smith, M.Sarikaya, and G.Thomas, Scripta Metall.,**15** (1981) 387.

65. B.V.Narasimha Rao and G.Thomas, in Proc. Intern. Conf. Martensitic Transformations, ICOMAT-79, Cambridge, MA, (1979).

66. L.Kaufmann and M.Cohen, Journal of Metals, October 1956, p.1393.

67. K.Tsuzaki and G.B.Olson, unpublished research, MIT, Cambridge, MA, (1984).

68. K.J. Tauer and R.J. Weiss, Bull. Am. Phys. Soc. II **6** (1961) 125

69. R.J. Weiss and K.J. Tauer, Phys. Rev. **102** (ii). (1956) 1490.

70. R.J. Weiss and K.J. Tauer, J. Phys. Chem. Solids, **4** (1958) 135.

71. L. Kaufman, E.W. Clougherty, and R.J. Weiss, Acta Metall. **11** (1963) 323.

72. R.J. Weiss, Proc. Phys. Soc., **82** (1963) 281

73. R. Ruhl, " *Splat Quenching of Fe-Based Alloys* ", Doctoral Thesis, MIT, Cambridge, MA, (1967).

74. A.P. Miodownik, Acta Metall., **18** (1970) 541

75. W.B. Pearson, "*Handbook of Lattice Spacings* ", Pergammon Press, London, (1958).

76. C.S. Barrett and T.B. Massalski, "*Structure of Metals* ", McGraw-Hill Book Company, New York, (1966).

77. J.Cowie and M. Azrin, "Shear Testing and Microvoid Formation in Ultrahigh-Strength Steels", Proc. 34th Sagamore Army Materials Research Conference, Lake George, New York, August, 1987.

78. A.S.Argon, J.Im, and R.Safoglou, Metall. Trans. **6A** (1975) 825.

79. A.Needleman, "A Model of void nucleation by Inclusion Debonding", Proc. 34th Sagamore Army Materials Research Conference, Lake George, New York, August, (1987).

80. J.W.Hutchinson and Viggo Tvergaard, "Softening due to Void Nucleation in Metals", June 1987, to be published.

81. W.M. Garrison and K.J. Handerhan, " Fracture Toughness: Particle-Dispersion Correlations", Proc. 34th Sagamore Army Materials Research Conference, Lake George, New York, August, (1987)

82. M.J. Gore, "Grain-Refining Dispersions and Mechanical Properties in Ultrahigh-Strength Steels", Doctoral Thesis, MIT, Cambridge, MA, (1988)

83. T. Mura, " *Micromechanisms od Defects in Solids* ", Martinus Nijhoff, The Hague, (1982).

84. F.R.N. Nabarro, Proc. Phys. Soc., **52** (1940) 90

85. J.W. Christian, " *The Theory of Transformations in Metals and Alloys* ", Pergamon Press, Oxford, England, 1975.

86. B. Lyubov, Fiz. Metal. Metalloved., **19**, (1965), 333.

87. C.C. Dollins, Acta Metall. **18** (1970) 1209

88. F.C. Larche, " *Nucleation and Precipitation on Dislocations* ", in "Dislocations in Solids" , F.R.N. Nabarro (ed.) Vol.IV, Nort Holand, (1979).

89. J.D. Eshelby, Proc. Royal Soc. **A241** (1957) 376.

90. J.D. Eshelby, Prog. Solid Mech. **2** (1961) 89.

BIOGRAPHICAL NOTE

The author was born and raised in Athens, Greece. He graduated from high school in 1977 and the same year he passed the general qualifying exam for the Greek universities. He graduated 5 years later with a diploma in Mechanical Engineering from Aristotle University. In 1983 he was admitted at M.I.T. where he earned an S.M degree in Naval Architecture and Marine Engineering and an S.M degree in Metallurgy in 1985. The same year he enrolled to the doctoral program in the Department of Materials Science and Engineering. The author pursued his graduate life at M.I.T. with his wife Yiota and his daughter Stella. Following graduation, he will assume a research position in industry or academia.